BRIGHT AND DARK PULSED FIBER LASERS BASED ON MULTIMODE INTERFERENCE

CHEN YU

FACULTY OF ENGINEERING
UNIVERSITI MALAYA
KUALA LUMPUR

2025

BRIGHT AND DARK PULSED FIBER LASERS BASED ON MULTIMODE INTERFERENCE

CHEN YU

THESIS SUBMITTED IN FULFILMENT OF THE REQUIREMENTS FOR THE DEGREE OF DOCTOR OF PHILOSOPHY

FACULTY OF ENGINEERING
UNIVERSITI MALAYA
KUALA LUMPUR

2025

UNIVERSITI MALAYA

ORIGINAL LITERARY WORK DECLARATION

Name of Candidate: CHEN YU

Matric No: S2156672

Name of Degree: DOCTOR OF PHILOSOPHY

Title of Project Paper/Research Report/Dissertation/Thesis ("this Work"):

Bright and dark pulsed fiber lasers based on multimode interference

Field of Study: Photonics

I do solemnly and sincerely declare that:

(1) I am the sole author/writer of this Work;
(2) This Work is original;
(3) Any use of any work in which copyright exists was done by way of fair dealing and for permitted purposes and any excerpt or extract from, or reference to or reproduction of any copyright work has been disclosed expressly and sufficiently and the title of the Work and its authorship have been acknowledged in this Work;
(4) I do not have any actual knowledge nor do I ought reasonably to know that the making of this work constitutes an infringement of any copyright work;
(5) I hereby assign all and every rights in the copyright to this Work to the Universiti Malaya ("UM"), who henceforth shall be owner of the copyright in this Work and that any reproduction or use in any form or by any means whatsoever is prohibited without the written consent of UM having been first had and obtained;
(6) I am fully aware that if in the course of making this Work I have infringed any copyright whether intentionally or otherwise, I may be subject to legal action or any other action as may be determined by UM.

Candidate's Signature Date: Jan, 15th, 2025

Subscribed and solemnly declared before,

Witness's Signature Date: 15/1/2025

Name:

Designation:

BRIGHT AND DARK PULSED FIBER LASERS BASED ON MULTIMODE INTERFERENCE

ABSTRACT

Pulsed lasers, particularly ultrashort pulsed lasers, find widespread application across various fields including telecommunications, bio-imaging, spectroscopy, atmospheric measurements, surgery, and material processing. This study focuses on harnessing the potential of the single mode-multimode-single mode (SMS) structure as a robust avenue for developing simple, compact, and cost-effective bright and dark pulsed erbium-doped fiber lasers (EDFLs). The SMS configuration serves as an ingenious artificial saturable absorber (SA), facilitating the generation of ultrashort pulsed lasers through the Kerr Effect with nonlinear multimode interference. By precisely fusion-splicing single mode fibers to both ends of a designated length of multimode fiber, the SMS architecture is established. Subsequently, integrating this SMS structure into a ring EDFL and finetuning parameters via a polarization controller enables the successful demonstration of ultrashort pulsed lasers.

Various experiments were conducted in both anomalous and normal dispersion regimes to explore the potential of different SMS structures for both bright and dark pulse generation. Within the net anomalous dispersion regime, utilizing step-index multimode fibers (SIMMF) with lengths of 96 mm, 156 mm, and 196 mm in the SMS structures, Q-switched fiber lasers were successfully observed. Remarkably, a notable milestone has been achieved with the observation of the shortest pulse width at 2.4 μs, coupled with a repetition rate of 155.8 kHz, attained at an input power of 343 mW and a center wavelength of 1530 nm. The artificial SA exhibited a significantly elevated damage threshold compared to conventional thin film types.

The mode-locked EDFLs were also realized using the grade-index multimode fiber (GIMMF) based SMS structures, with lengths approximately at 45 mm, 100 mm, and 150 mm. These lasers produced both conventional soliton and bound soliton phenomena with

pulse widths as low as 290 fs, accompanied by a repetition rate around 22 MHz and a center wavelength of around 1574 nm. Notably, the pulse width exhibited minimal variation across different lengths of GIMMF. Additionally, dark pulses were also realized with a minimum pulse width of 1.6 ns and a repetition rate of 21.5 MHz. Noteworthy spectral analysis revealed the dark pulse to be dual wavelength, with peak wavelengths centered at 1567.2 nm and 1569.4 nm, indicating the presence of a domainwall dark pulse phenomenon

By integrating 230 meters of dispersion compensation fiber (DCF) into the cavity, the laser is ensured to operate within a significantly large net normal dispersion region. In this study, a 103 mm length GIMMF-based SMS structure is focused on within this domain. As the pump power increased, multiple pulsing emerged, with the pulse cluster ranging from 3 to 16 pulses. These multiple pulsing instances exhibited remarkably broad dissipative solitons, highlighting the potential of the SMS structure for direct supercontinuum generation. Additionally, harmonic pulses were also observed extending up to the 35^{th} harmonic alongside the dissipative soliton.

Keywords: Q-switching, Mode-locking, dark pulse, soliton, SMS structure.

LASER SERAT BERDENYI TERANG DAN GELAP BERDASARKAN GANGGUAN MULTIMOD

ABSTRAK

Laser berdenyut, terutamanya laser berdenyut ultrashort, menemui aplikasi meluas dalam pelbagai bidang termasuk telekomunikasi, pengimejan bio, spektroskopi, pengukuran atmosfera, pembedahan dan pemprosesan bahan. Kajian ini menumpukan pada memanfaatkan potensi struktur mod tunggal-multimode-tunggal (SMS) sebagai jalan yang teguh untuk membangunkan laser gentian doped erbium (EDFL) yang mudah, padat dan kos efektif. Konfigurasi SMS berfungsi sebagai penyerap tepu buatan

(SA) yang cerdik, memudahkan penjanaan laser berdenyut ultrashort melalui Kesan Kerr dalam gangguan multimod tak linear. Dengan mencantumkan gentian mod tunggal dengan tepat kepada kedua-dua hujung gentian berbilang mod panjang yang ditetapkan, seni bina SMS diwujudkan. Selepas itu, menyepadukan struktur SMS ini ke dalam cincin EDFL dan parameter penalaan halus melalui pengawal polarisasi membolehkan demonstrasi laser berdenyut ultrashort yang berjaya.

Pelbagai eksperimen telah dijalankan dalam kedua-dua rejim penyebaran anomali dan normal untuk meneroka potensi struktur SMS yang berbeza untuk penjanaan nadi cerah dan gelap. Dalam rejim penyebaran anomali bersih, menggunakan gentian multimod indeks langkah (SIMMF) dengan panjang 96 mm, 156 mm, dan 196 mm dalam struktur SMS, laser gentian suis Q telah berjaya diperhatikan. Hebatnya, pencapaian yang ketara telah dicapai dengan pemerhatian lebar nadi terpendek pada 2.4 μs, ditambah dengan kadar pengulangan 155.8 kHz, dicapai pada kuasa input 343 mW dan panjang gelombang tengah 1530 nm. SA buatan mempamerkan ambang kerosakan yang ketara tinggi berbanding jenis filem nipis konvensional.

EDFL yang dikunci mod juga direalisasikan menggunakan struktur SMS berasaskan gentian mod indeks gred (GIMMF), dengan panjang kira-kira 45 mm, 100 mm dan 150 mm. Laser ini menghasilkan kedua-dua soliton konvensional dan fenomena soliton terikat dengan lebar nadi serendah 290 fs, disertai dengan kadar ulangan sekitar 22 MHz dan panjang gelombang tengah sekitar 1574 nm. Terutama, lebar nadi menunjukkan variasi minimum merentasi panjang GIMMF yang berbeza. Selain itu, denyutan gelap juga direalisasikan dengan lebar nadi minimum 1.6 ns dan kadar pengulangan 21.5 MHz. Analisis spektrum yang perlu diberi perhatian mendedahkan nadi gelap menjadi dua panjang gelombang, dengan panjang gelombang puncak berpusat pada 1567.2 nm dan 1569.4 nm, menunjukkan kehadiran fenomena nadi gelap dinding domain

Dengan menyepadukan 230 meter gentian pampasan penyebaran (DCF) ke dalam rongga, laser dipastikan beroperasi dalam kawasan penyebaran normal bersih yang besar

dengan ketara. Dalam kajian ini, kami menumpukan pada struktur SMS berasaskan GIMMF sepanjang 103 mm dalam domain ini. Apabila kuasa pam meningkat, pelbagai denyutan muncul, dengan kelompok nadi antara 3 hingga 16 denyutan. Berbilang kejadian berdenyut ini mempamerkan soliton pelesapan yang sangat luas, menonjolkan potensi struktur SMS untuk penjanaan supercontinuum langsung. Selain itu, denyutan harmonik juga diperhatikan memanjang sehingga harmonik ke-35 bersama soliton lesap.

Keywords: Penukaran Q, Penguncian mod, nadi gelap, soliton, struktur SMS.

ACKNOWLEDGEMENTS

Firstly, I would like to express my sincerest gratitude to my supervisors, Professor Ir. Dr. Sulaiman Wadi Harun, Prof. Ir. Ts. Dr. Tiu Zian Cheak, Professor Ir. Dr. Kaharudin Bin Dimyati, and Dr. Tan Sin Jin. You are like a lighthouse, guiding me on the path of acquiring knowledge. Professor Ir. Dr. Sulaiman Wadi Harun is a great supervisor with much patience and profound knowledge. Without the platform you have built, I cannot find the joy of scientific research. Without your professional and patient guidance, I cannot deepen my knowledge. I am fortunate to have chosen to pursue a PhD, and I am even more fortunate to have met my mentors on the path of pursuing a PhD.

My sincere gratitude also goes to Dr. Abdulkadir Mukhtar Diblawe, Dr. Ahmad Haziq Aiman Rosol, and all the lab mates for their help and knowledge sharing. You taught me how to conduct optical experiments from Optics 101. More importantly, you have given me encouragement and support like family in a foreign land. The experiments that lasted until late at night became more interesting because of your company.

To my family members, thank you all for your encouragement and support. It is never possible for me to pursue my PhD without your understanding and strong support.

Again, thank you to everyone who helped me directly or indirectly.

TABLE OF CONTENTS

Abstract iii

Abstrak v

Acknowledgements..... vii

Table of Contents viii

List of Figures xii

List of Symbols and Abbreviations..... xvii

CHAPTER 1: INTRODUCTION 1

1.1 Background 1

1.2 Thesis Aim and Objectives 3

1.3 Scope of Research..... 4

CHAPTER 2: LITERATURE REVIEW 7

2.1 Introduction..... 7

2.2 Fiber Characteristics 8

2.2.1 Dispersion 8

2.2.2 Nonlinearity 11

2.3 Nonlinear Pulse Propagation 12

2.3.1 Pulse Propagation in Optical Fibers 12

2.3.2 Nonlinear Effects 13

2.3.3 Solitons 14

2.4 Multi-mode Interference 18

2.4.1 Self-imaging 18

2.4.2 Spectral filtering 20

2.5 Resonators..... 21
2.6 Saturable Absorber 22

2.6.1 Real SAs 23

2.6.2 Artificial SAs 24

2.6.3 SA Characterization 27

2.7 Generation of Short Pulse in Fiber Laser 29

2.7.1 Q-switching Operation 29

2.7.2 Mode-locking Operation 31

2.8 Summary of research gaps 32

CHAPTER 3: Q-SWITCHED AND MODE-LOCKED PULSES GENERATIONS WITH SMS STRUCTURE AS ARTIFICIAL SA 33

3.1 Introduction..... 33

3.2 Q-switching Operation Using SIMMF Based Artificial SA 34

3.2.1 Mechanism of Q-switching Operation Based on SMS structure..... 35

3.2.2 Experimental Arrangement 35

3.2.3 Q-switching Performance by Using SIMMF Based Artificial SA 39

3.2.4 Q-switching Performance Comparison with MoS_2 based real SA 44

3.3 Mode-locking Operation with Conventional Soliton Using GIMMF Based Artificial SA..... 48

3.3.1 Mechanism of Mode-locking Operation Based on SMS structure. 49

3.3.2 SA Preparation and Experimental Setup 49

3.3.3 Mode-locking Performance with Conventional Soliton Using GIMMF

based SMS Structure as Artificial SA 53

3.4 Harmonic Mode-locking Using GIMMF based Artificial SA 59

3.4.1 Mechanism of HML Operation Based on SMS structure. 59

3.4.2 Experimental Arrangements 60

3.4.3 HML Performance Using SMF-GIMMF-SMF as Artificial SA 62

3.5 Discussion 67

3.6 Summary 68

CHAPTER 4: UNCONVENTIONAL SOLITONS IN EDFL USING SMS STRUCTURE AS ARTIFICIAL SA 69

4.1 Introduction..... 69

4.2 Bound Soliton in Anomalous Dispersion Regime 70

4.2.1 Mechanism of Bound Soliton Operation 71

4.2.2 Experimental Approach 72

4.2.3 Bound Soliton in Anomalous Dispersion Regime Performance 75

4.3 Ultra-broadband Dissipative Soliton with Multi-Pulses 82

4.3.1 Cavity Design 82

4.3.2 Ultra-broadband Dissipative Soliton Performance 83

4.4 Harmonics of Dissipative Soliton 88

4.4.1 Experimental Setup 89

4.4.2 Harmonics of Dissipative Soliton Performance 90

4.5 Discussion 96

4.6 Summary 97

CHAPTER 5: DARK PULSE OPERATION IN EDFL 98

5.1 Introduction..... 98

5.2 Domain Wall Dark Pulse in Anomalous Dispersion Regime 99

5.2.1 Mechanism of DW Dark Pulse Formation. 100

5.2.2 Experimental Setup 101

5.2.3 Laser Performances 102

5.2.4 Performance Comparison of Dark Pulse in Anomalous Dispersion Regime Using Polyacrylonitrile as SA 106

5.3 Harmonics of Domain Wall Dark Pulse in Normal Dispersion Regime 113

5.3.1 Experimental Setup 114

5.3.2 Domain Wall Dark Pulse in Normal Dispersion Regime Performance . 114

5.4 Discussion 119

5.5 Summary 120

CHAPTER 6: CONCLUSION AND FUTURE WORK 121

6.1 Conclusion 121

6.2 Novelty and Contributions 125

6.3 Future Work 127

References .....

129

List of Publications and Papers Presented 146

LIST OF FIGURES

Figure 1.1: Research flow chart 6

Figure 2.1: Dispersion characteristic against wavelength for Corning® SMF-28e® 9

Figure 2.2: Schematic drawing of light coupling from an SMF to an MMF 19

Figure 2.3: A fiber laser configuration with a ring cavity (Agrawal, 2008). 21

Figure 2.4: Example of doped fiber laser configuration with a figure-of-eight cavity (Agrawal, 2008). 22

Figure 2.5: Schematic drawing of a balanced twin detector measurement method. 28

Figure 2.6: Measurement of linear absorption for a SA..... 28

Figure 3.1: Schematic drawing of SIMMF based SMS structure. 36

Figure 3.2: Spectral transmission of the SIMMF based SA. 36

Figure 3.3: Absorption curve of the SIMMF based SA. 37

Figure 3.4: Schematic diagram of experimental setup of the ring cavity for Qswitched pulse generation using SIMMF as artificial SA. (Inset: microscope image of the SMS structure and its splicing point.) 38

Figure 3.5: Spectrum of Q-switched operation using SIMMF based artificial SA with variation of input pump power. 39

Figure 3.6: (a)Typical pulse train of Q-switched operation with SIMMF based artificial SA; (b) Dual-pulse envelope of the enlarged pulse train. 40

Figure 3.7: RF spectrum of Q-switching operation using SIMMF based artificial SA. . 41

Figure 3.8: Long-term stability of the Q-switched operation. 41

Figure 3.9: Average output power and pulse energy of the Q-switched laser with respect to the pump power. 42

Figure 3.10: Average output power and pulse energy of the Q-switched laser with respect to the pump power. 43

Figure 3.11: Schematic drawing of the cavity setting for Q-switching using MoS_2 as SA. 44

Figure 3.12: Spectrum of Q-switched operation using MoS_2 as SA with variation of input pump power. 45

Figure 3.13: (a) Pulse train of Q-switched operation with MoS_2 as SA; (b) Dual-pulse envelope of the enlarged pulse train..... 45

Figure 3.14: RF spectrum of Q-switching operation with MoS_2 as SA. 46

Figure 3.15: Average output power and pulse width of the Q-switched laser with respect to the pump power using MoS_2 as SA. 47

Figure 3.16: Average output power and pulse energy of the Q-switched laser with respect to the pump power using MoS_2 as SA. 47

Figure 3.17: Schematic drawing of GIMMF based SMS structure. 50

Figure 3.18: Spectral transmission of the 4.5 cm GIMMF based SA. 51

Figure 3.19: Absorption curve of the 4.5 cm GIMMF based SA. 51

Figure 3.20: Schematic diagram of experimental setup of the ring cavity for Mode-locked pulse generation using GIMMF as artificial SA. 53

Figure 3.21: Spectrum of mode-locked laser pulse with GIMMF based structure as SA. 54

Figure 3.22: OSC trace of the mode-locked laser pulse using GIMMF based structure as SA. 55

Figure 3.23: RF spectrum of the mode-locked laser pulse over 1 GHz span using GIMMF based structure as SA (inset: enlarged RF spectrum at 22 MHz). 56

Figure 3.24: Autocorrelator trace of the mode-locked laser pulse using GIMMF based structure as SA. 56

Figure 3.25: Pulse energy and output power vs LDP the mode-locked laser pulse using GIMMF based structure as SA. 57

Figure 3.26: Long-term stability of the Mode-locked operation with GIMMF based structure as SA. 58

Figure 3.27: Spectral transmission of the 10.3 cm GIMMF based SA. 61

Figure 3.28: Absorption curve of the 10.3 cm GIMMF based SA. 61

Figure 3.29: Spectrum of HML with GIMMF based structure as SA. 63

Figure 3.30: Pulse Train of the 2nd HML using GIMMF based structure as SA. 63

Figure 3.31: Pulse Train of the 3rd HML using GIMMF based structure as SA. 64

Figure 3.32: RF spectrum of (a) 2nd HML and (b) 3rd HML over 500 MHz span using GIMMF based structure as SA. 65

Figure 3.33: Autocorrelator trace of 2nd HML using GIMMF based structure as artificial SA. 65

Figure 3.34: Pulse energy and output power vs input pump power of the HML using GIMMF based structure as SA. 66

Figure 4.1: Schematic diagram of the SMS structure with the image of splicing point at both ends of GIMMF. 72

Figure 4.2: Spectral transmission characteristic of the SMS structure. 73

Figure 4.3: Nonlinear transmission curve of the SMS structure-based SA. 74

Figure 4.4: Schematic diagram of the mode-locked fiber laser 75

Figure 4.5: Conventional soliton performances (a) Optical spectrum; (b) pulse train; (c) RF spectrum (inset: the RF spectrum within a larger range of 1 GHz); (d) autocorrelation trace. 77

Figure 4.6: Long term stability test of the conventional soliton (Every 1 hour for 6 hours) 78

Figure 4.7: Bound soliton performances (a) Optical spectrum; (b) pulse train; (c) RF spectrum (inset: the RF spectrum within a range of 500 MHz); (d) autocorrelation trace. 79

Figure 4.8: Bound soliton characteristics at different pump power levels (a)-(c) Autocorrelator trace. (d)-(f) Optical spectrums. 81

Figure 4.9: Schematic diagram of mode-locked EDFL cavity with dispersion management using SMF-GIMMF-SMF as SA. ..... 83 Figure 4.10: Evolution of optical spectrum with the increment of pump powers..... 84

Figure 4.11: Evolution of bunch envelope with pump power. 84

Figure 4.12: Projection of number of pulses in an envelope with pump power. 86

Figure 4.13: (a) Oscillation trace of pulses at pump power of 23.2 mW pump power. (b)

Oscillation trace of pulses at pump power of 220 mW pump power. 86

Figure 4.14: RF spectrum of bunch pulses at different frequencies span. (a) RF spectrum at 5 MHz span. (b) RF spectrum at 200 MHz span. 87

Figure 4.15: Pulse width measurement with autocorrelator..... 88

Figure 4.16: Pulse trains of the laser: (a) FML at 858 KHz, pump power 23.2 mW (b) 2nd HML at 1.72 MHz, pump power 36.0 mW (c) 3rd HML at 2.56 MHz, pump power 53.9 mW (d) 4th HML at 3.40 MHz, 73.4 mW (e) 5th HML at 4.29 MHz, pump power 97.0 mW 91

Figure 4.17: 2D contour view of pulse train at various pump power 92

Figure 4.18: Spectrum of different orders of HML at different pump powers. 92

Figure 4.19: Autocorrelation trace of the pulse at 5th harmonic. 93

Figure 4.20: RF spectrum: (a) 2nd HML at 1.72 MHz (b) 3rd HML at 2.56 MHz (c) 4th HML at 3.40 MHz (d) 5th HML at 4.29 MHz 94

Figure 4.21: Output power vs. input power at different harmonic orders..... 95

Figure 5.1: Experimental setup of the domain-walled dark pulse EDFL with SMF-GIMMF-SMF as artificial saturable absorber. 102

Figure 5.2：Wavelength domain of DW dark pulse throughout the operating pump power range. Inset is the optical spectrum at pump power of 195.4 mW. ..... 103 Figure 5.3：Temporal domain of DW dark pulse at pump power of 195.4 mW. 104

Figure 5.4：Output power and average pulse energy against pump power. 105

Figure 5.5：RF spectrum of DW dark pulse EDFL at pump power of 195.4 mW. 106

Figure 5.6: Schematic diagram of mode-locked EDFL cavity with as Polyacrylonitrile SA. 107

Figure 5.7: Spectral transmission of the polyacrylonitrile thin film SA. 108

Figure 5.8: Absorption curve of the polyacrylonitrile thin film SA. 108

Figure 5.9：Wavelength domain of DW dark pulse throughout the operating pump power range. 109

Figure 5.10：Temporal domain of DW dark pulse at pump power of 72.4 mW. 110
Figure 5.11：Output power and average pulse energy against pump power. 111

Figure 5.12：RF spectrum of DW dark pulse EDFL at pump power of 72.4 mW. Inset is the enlarged view of RF ranging from 15-35 MHz. 112

Figure 5.13: Wavelength domain of harmonic DW dark pulse throughout the operating pump power range in normal dispersion regime. 115

Figure 5.14: Pulse train of the harmonic DW dark pulse at pump power of 53.9 mW. 116

Figure 5.15: RF spectrum of the harmonic DW dark pulse EDFL at pump power of 53.9 mW. 117

Figure 5.16: Output power and average pulse energy against pump power of harmonic DW dark pulse in normal dispersion regime..... 118

LIST OF SYMBOLS AND ABBREVIATIONS

A	:	Pulse amplitude
α_{ns}	:	Non-saturable loss
λ	:	Wavelength
$\Delta\lambda$	:	3dB bandwidth
λ_0	:	Operation wavelength of a specific intensity laser light
λ_{high}	:	Operation wavelength of high intensity laser light
n	:	Refractive index
n_g	:	Group index
n_{eff}	:	Effective refractive index
$\Delta n_{eff,n}$	:	Difference of effective refractive index
$\tilde{n}$	:	Complex refractive index
β	:	Propagation constant
β_n	:	Intensity dependent propagation constant
c	:	Speed of light in vacuum
C_n	:	Mode expansion coefficient
D	:	Dispersion parameter
$\|E\|^2$	:	Optical intensity inside fiber
I	:	Intensity
I_{sat}	:	Saturation intensity
L	:	Fiber length
$\chi^{(3)}$	:	Third-order susceptibility
$Re(\chi^{(3)}_{xxxx})$	:	Real part of third-order susceptibility fourth tensor
v_g	:	Group velocity
ω	:	Pulse frequency

ω_0	:	Pulse frequency at center spectrum
ϕ	:	Phase change
ϕ_{nl}	:	Nonlinear phase shift
z	:	Propagation distance
γ	:	nonlinear parameter
e_n	:	The n-th guided mode
$\Delta\tau$	:	Pulse width
$\Delta\upsilon$	:	Spectral width in Hz
T(I)	:	Intensity dependent transmission
ΔT	:	Modulation depth
t	:	Time
ξ_0	:	Eigenvalue in the spectral transform
AC	:	Auto-correlator
ASE	:	Amplified Spontaneous Emission
CW	:	Continuous Wave
DCF	:	Dispersion Compensation Fiber
EDF	:	Erbium Doped Fiber
EDFL	:	Erbium Doped Fiber Laser
EDFA	:	Erbium Doped Fiber Amplifier
FWHM	:	Full Width Half Maximum
FWM	:	Four-Wave Mixing
GIMMF	:	Grade-index Multimode Fiber
GLE	:	Ginzburg-Landau Equation
GVD	:	Group Velocity Dispersion
NPR	:	Nonlinear Polarization Rotation
NALM	:	Nonlinear Amplifying Loop Mirror

NLMMI	:	Nonlinear Multimode Interference
NOLM	:	Nonlinear Optical Loop Mirror
NLSE	:	Nonlinear Schrödinger Equation
OSA	:	Optical Spectrum Analyzer
OSC	:	Oscilloscope
PC	:	Polarization Controller
RFSA	:	Radio Frequency Spectrum Analyzer
SA	:	Saturable Absorber
SMF	:	Single Mode Fiber
SNR	:	Signal to Noise Ratio
SOA	:	Semiconductor Optical Amplifier
SPM	:	Self-Phase Modulation
SIMMF	:	Step-index Multimode Fiber
SMS	:	Single mode- Multimode- Single Mode
TBP	:	Time-Bandwidth Product
TOD	:	Third order dispersion
WDM	:	Wavelength Division Multiplexing
XPM	:	Cross Phase Modulation

CHAPTER 1: INTRODUCTION

1.1 Background

Ultrashort laser pulse generation is a cutting-edge technology that has revolutionized numerous fields, from science and medicine to industry and telecommunications. It encompasses the generation of extremely short-duration laser pulses, typically femtoseconds laser pulses or picoseconds laser pulses. Recently, the generation and application of attosecond laser pulses have pushed the development of ultrashort lasers to a climax. Pierre Agostini, Ferenc Krausz, and Anne L'Huillier, who have observed the attosecond laser pulses, were awarded the Nobel Prize in Physics for this achievement. The ultrashort laser pulses have opened new frontiers in research and applications by enabling the precise control of light in time, making it possible to investigate and manipulate ultrashort processes on a molecular and atomic scale.

Ultrashort laser pulses can be generated through two primary methods: active and passive mode-locking. Active mode-locking involves the use of an external component, such as an acousto-optic modulator or an electro-optic modulator, to actively manipulate the laser cavity. By periodically introducing phase modulation to the laser pulse, it synchronizes and shortens the pulses (Haus, 2000). This method allows for precise control over the pulse repetition rate and pulse duration, making it well-suited for specific applications requiring customized pulse characteristics. Passive mode-locking, on the other hand, relies on the inherent properties of the laser cavity to generate ultrashort pulses without the need for external components. It typically employs saturable absorbers (SA) to passively modulate the intra-cavity light, causing the laser to self-start mode-locking (Keller, 2022). This method is favorable because of its simplicity, reliability, and cost-effectiveness (Mohd Rusdi et al., 2017).

SAs are the key devices that determine the mode-locking performance in passively mode-locking fiber laser (MLFL) generation. Real SAs are typically based on the nonlinear absorption properties of a material, achieved through the absorption of photons within the material. Typical real SAs are semiconductor saturable absorber mirrors (SESAMs), transition metal chalcogenides (TMDs), carbon nanotube (CNT), graphene and black phosphorous (BP) (Hisyam et al., 2017). These SAs have their pros and cons, but most of them suffer from high cost, complex fabrication processes, narrow operation regime and low damage threshold, which have spurred researchers to develop artificial SAs.

The advent of artificial SA has revolutionized the landscape of MLFLs, addressing the limitations of real SAs. Artificial SAs, owing to their all-fiber composition, can be seamlessly integrated into optical systems while boasting a high damage threshold. In contrast to their conventional counterparts with narrow operation bandwidths, artificial SAs exhibit versatility across a broad spectrum of wavelengths. Moreover, artificial SAs demonstrate favorable nonlinear optical characteristics, including high modulation depth, minimal non-saturable loss, and low saturation intensities. These attributes enhance laser stability, efficiency, and pulse quality.

Artificial SAs harness nonlinear optical effects rather than direct photon absorption. Key artificial SA types encompass nonlinear polarization rotation (NPR), nonlinear polarization evolution (NPE), nonlinear optical loop mirror (NOLM), nonlinear amplifying loop mirror (NALM), and single-mode fiber (SMF)-multimode fiber (MMF)-SMF (denoted as SMS structures. NPR and NPE leverage nonlinear polarization phenomena and polarization instabilities within the laser cavity for modelocking, while NOLM and NALM utilize fiber loops to achieve this effect. SMS structures exploit the Kerr Effect of nonlinear multimode interference (NL-MMI).

Among artificial SAs, the SMS structure stands as the most recent and least explored. Furthermore, systematic investigations into the SMS structure's potential as an artificial SA for generating various ultrashort pulses remain scarce, prompting the research objectives outlined in this study. Here, the main focus is to experimentally probe the capabilities of different ultrashort pulse generation using SMS structures based on stepindex multimode fiber (SIMMF) and graded-index multimode fiber (GIMMF) as artificial SAs.

1.2 Thesis Aim and Objectives

The study of SAs is crucial in passive Q-switching and mode-locking technology for generating ultrashort pulsed lasers. Among SAs, the SMS structure stands out as a unique type, employing NL-MMI. This research focuses on exploring the effectiveness of SMS structure as an artificial SA in passive Q-switching and mode-locking operations. The primary aim is to systematically demonstrate the generation of various types of pulsed lasers utilizing the SMS structures as artificial SAs and evaluate the performances of the proposed SMS structures in pulse formation. To realize this aim, the following objectives have been outlined:

1. Propose an SMS structures to generate Q-switched pulse, conventional bright soliton and harmonic mode-locked bright pulse, evaluate the performance of this SMS structures as artificial SAs in Erbium-doped fibre lasers (EDFLs) and analyse the characteristics of the Q-switched pulses, conventional bright soliton and harmonic mode-locked bright pulse.
2. Propose and utilize an SMS structure as artificial SAs in dispersion managed cavity to generate dissipative solitons in EDFLs and evaluate the performance of the SMS structure and the generated dissipative solitons.

3. Propose and utilize an SMS structures as artificial SAs in EDFL to generate dark pulse and evaluate the performance of the SMS structure and the generated dark pulse.

After experimental demonstrations of different kinds of ultrashort pulses with SMS structures, the performance of the pulses shall be evaluated in time domain, frequency domain and spectrum domain with data processing tools.

1.3 Scope of Research

This thesis comprises six chapters that comprehensively demonstrate and discuss the generation of various types of pulsed lasers utilizing SMS structure as artificial SA. This chapter provides a brief overview of practical uses of pulsed lasers and the ways of passively generating Q-switched and mode-locked lasers, which leads to the motivation of current study, along with outlining the motivations and objectives of the present study. It also offers an outline of the contributions made by this thesis to the existing body of knowledge.

Chapter 2 explores the theoretical background and fundamental principles concerning the nonlinear effects within optical fibers, which play a pivotal role in the generation of pulsed lasers. It delves into topics such as nonlinear pulse propagation in dispersive media and the dispersion phenomena occurring within fibers. Additionally, the chapter reviews various SAs utilized for passive pulsed laser generation, as well as examining resonators and pulsing techniques.

Chapter 3 to Chapter 5 evaluate SMS structures in different pulses and these chapters together picture the whole performance characteristics of SMS structures as artificial SA. Figure 1.1 shows a flow chart of the research, indicating the relationship of the chapters.

Chapter 3 demonstrates the generations of Q-switched and conventional soliton mode-locked fiber lasers based on SMS structure as artificial SA. The cavity was set in net anomalous dispersion regime, where the solution of nonlinear Schrödinger equation

(NLSE) in this regime supports bright solitons. The mechanism of Q-switched operation, conventional mode-locked operation and harmonics based on the SMS structure as SA was studied at the beginning of each section. Subsequently, experimental setup and results in the time domain, spectrum domain, frequency domain were analyzed for Qswitched operation, conventional mode-locked operation, and harmonics respectively in each section. Due to the expected versality of the SMS structure for ultrashort pulse generation, research with different experimental settings is continued in later chapters.

Chapter 4 focuses on special kinds of solitons generation with SMS structure in EDFLs. Firstly, the GIMMF was shortened from around 10.3 cm to 4.5 cm to observe the bound state soliton. The mechanisms and performance of bound soliton generation using SMS structure were presented. In section 4.3 and 4.4, the ring cavity was set in a net normal dispersion regime to observe the possibility of dissipative soliton generation using SMS structure. A long length of dispersion compensation fiber (DCF) was used to compensate for the dispersion introduced by the SMS. This new cavity setting gave an ultra-broadband dissipative soliton with multi-pulses. By further increase of pump power and adjustment of the polarization controller, harmonics of the dissipative soliton were observed, and the results were presented in section 4.4.

Chapter 5 focuses on generating dark pulses based on SMS structure. By managing the net dispersion of the cavity, domain wall (DW) dark pulse and harmonic modelocked DW dark pulse were demonstrated in anomalous and normal dispersion regime respectively.

Finally, chapter 6 summarizes the findings of this PhD work and suggests future works accordingly.

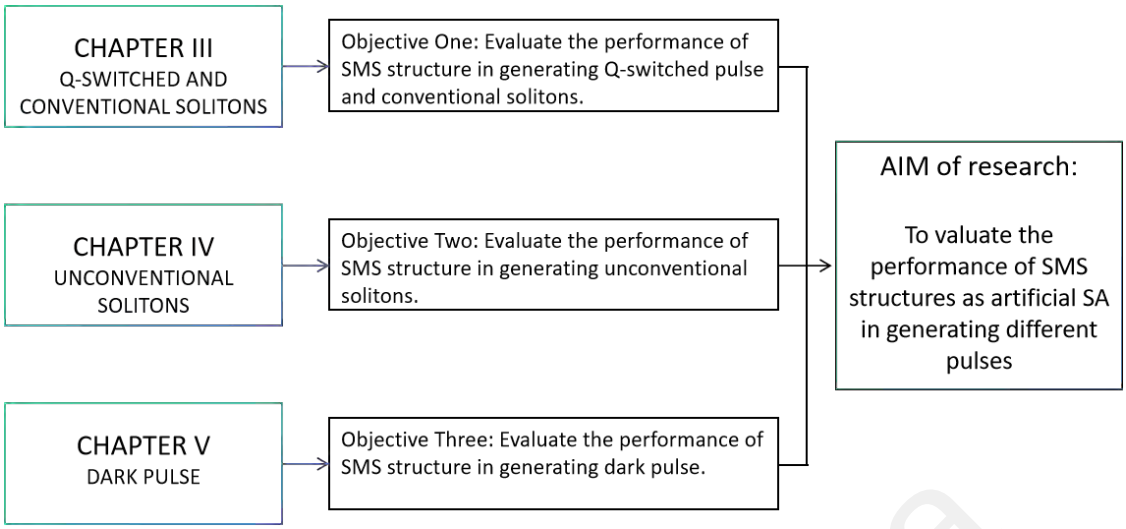

Figure 1.1: Research flow chart

In summary, this work will help the readers to understand the mechanisms underlying the formation of various soliton types with SMS structures as artificial SAs. This comprehensive study provides insights into the formation processes of different soliton types, offering valuable directions for further analysis and development of SMS structures.

CHAPTER 2: LITERATURE REVIEW

2.1 Introduction

This chapter intends to investigate the theoretical underpinnings and previous experimental findings pertinent to the thesis objective of demonstrating pulse generation possibilities using single-mode fiber (SMF) - multimode fiber (MMF) - SMF or SMS structures as artificial saturable absorbers (SAs). The propagation of light within an optical fiber is influenced not only by the light itself but also by fiber characteristics such as loss, gain, dispersion, and nonlinearity. Section 2.2 describes the impact of fiber characteristics on laser light transmission, with a particular focus on dispersion and nonlinearity.

The interplay between nonlinearity and dispersion, particularly in the anomalous dispersion regime, gives rise to intriguing phenomena, among which soliton formation stands out. Solitons, versatile entities finding applications in optical communication systems, manifest in various forms under both anomalous and normal dispersion regimes. Section 2.3 explains the nonlinear phenomena occurring during the propagation of laser light within optical fibers.

SMS structures function as artificial SAs by leveraging the mechanism of nonlinear multimode interference (NL-MMI). Within a multimode fiber, NL-MMI engenders periodic replication of the input field, a phenomenon known as self-imaging. Additionally, SMS structures serve as spectral filters, facilitating the selective transmission of pulses. Section 2.4 delves into the NL-MMI mechanism and its implications. On the other hand, resonators serve as the foundational framework for pulse formation. Section 2.5 provides a brief overview of two types of resonators compatible with artificial SAs for pulse generation.

Both active and passive techniques can be employed for ultrashort pulse generation, with passive Q-switching and mode-locking relying on SAs as crucial components. SAs, categorized into real and artificial types, play pivotal roles in these techniques. Artificial SAs, serving as counterparts to real SAs, operate based on nonlinear effects rather than saturable absorption. Section 2.6 offers a concise introduction to SAs utilized for pulse generation and methods for evaluating their characteristics. Section 2.7 delves into the theoretical foundations of Q-switching and mode-locking, while reviewing previous studies employing artificial SAs, particularly SMS structures, for pulse generation using these techniques.

2.2 Fiber Characteristics

The behavior of optical fibers undergoes significant changes when subjected to highintensity laser light, consequently influencing light propagation within the fiber. This alteration is intricately linked to the dispersion and nonlinearity characteristics of optical fibers, which profoundly impact the generation of Q-switched and mode-locked pulses within a fiber laser cavity. This section delves into the mechanisms underlying both phenomena.

2.2.1 Dispersion

Dispersion significantly influences the propagation of ultrashort optical pulses by inducing varying velocities among pulses of different frequencies. Two common types of dispersion are chromatic dispersion and polarization-mode dispersion. Chromatic dispersion, the predominant form, leads to pulse broadening during short-distance light transmission. This dispersion arises from the frequency-dependent nature of the refractive index. In optical fiber propagation, the mode-propagation constant β is expressed by the following equation: (Agrawal, 2013a)

$$\beta(\omega) = \frac{n(\omega)}{c} = \beta_0 + \beta_1(\omega - \omega_0) + \beta_2(\omega - \omega_0)^2 + \cdots, \quad (2.1)$$

where ω_0 is the pulse frequency at center spectrum. β_1 and β_2 are related to refractive index n(ω) and the frequency as in (2.2) and (2.3).

$$\beta_1 = \frac{1}{v_g} = \frac{n_g}{c} = \frac{1}{c}\left(n + \omega \frac{dn}{d\omega}\right), \quad (2.2)$$

$$\beta_2 = \frac{1}{c}\left(2\frac{dn}{d\omega} + \frac{d^2n}{d\omega^2}\right), \quad (2.3)$$

where n_g is the group index and v_g is the group velocity. The envelop of an optical pulse should move at the group velocity, but the dispersion represented by β_2 can cause the pulse broadening. This dispersion is known as group velocity dispersion (GVD) and β_2 is the GVD parameter. Usually, fiber specifications give dispersion parameter D, which is defined as:

$$D = \frac{d\beta_1}{d\lambda} = -\frac{2\pi c}{\lambda^2}\beta_2, \quad (2.4)$$

where λ is the center wavelength and c is the speed of light in vacuum. For Corning® SMF-28e®, the dispersion characteristic against wavelength is given by Figure 2.1. It has a zero dispersion at 1313 nm.

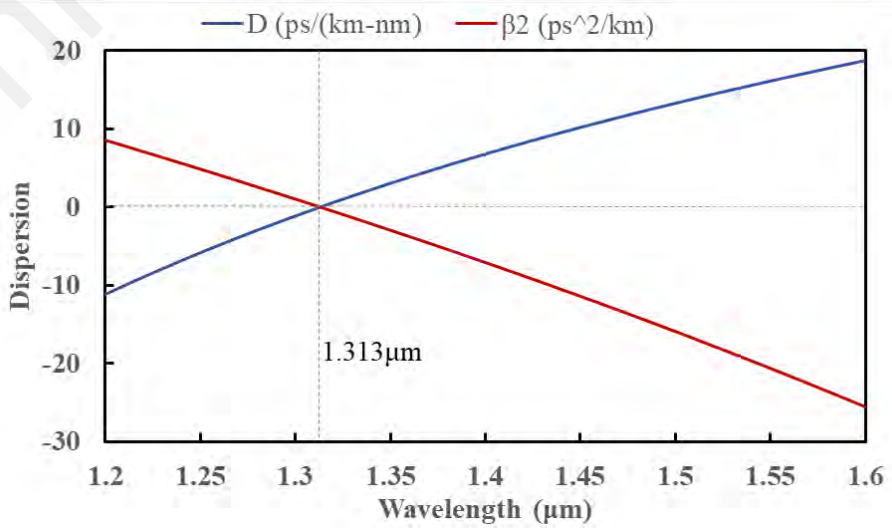

Figure 2.1: Dispersion characteristic against wavelength for Corning® SMF-28e®

The wavelength corresponding to zero dispersion is denoted as λ_D. If the operating wavelength λ is smaller than λ_D, β_2 is positive, the operation is in normal-dispersion regime. If the operating wavelength λ is larger than λ_D, β_2 is negative, the operation is in anomalous-dispersion regime. Pulses with longer wavelengths travel faster in the normal-dispersion regime and slower in the anomalous-dispersion regime. The operation regime affects the nonlinear effects, which will be discussed in the next section. It is important to note that at zero dispersion does not mean the dispersion is zero, because the third-order dispersion (TOD) should be included near λ_D. In the meantime, TOD should be taken into consideration for ultrashort pulses analysis, because TOD can cause ultrashort pulse distortion.

Chromatic dispersion poses a significant challenge in optical communication systems due to its tendency to cause pulse broadening, which can degrade system performance. To mitigate this effect, dispersion compensation fibers (DCFs) or dispersion-shifted fibers are commonly employed to reduce dispersion levels close to zero around the operational center wavelength. Additionally, polarization-mode dispersion (PMD) contributes to pulse broadening, particularly in long-haul optical communication systems, where it becomes a focal point of interest. PMD arises from the discrepancy in the mode-propagation constants (β) between the x and y directions, known as modal birefringence. Methods to manipulate birefringence include shaping the fiber core elliptically and introducing stress, with the latter being the more effective approach. Notably, PMD in MMF tends to be more pronounced compared to SMF. However, the impact of PMD is minimal in this work, as very short lengths of MMF were utilized where their magnitude is negligible.

2.2.2 Nonlinearity

Optical fibers as a dielectric medium, response nonlinearly to intense electromagnetic fields. This nonlinearity can cause nonlinear effects when light propagates inside the fibers. Nonlinear effects are useful because it can compensate for pulse dispersion and supports bright soliton formation. On the other hand, it limits the maximum power in optical fibers.

The origin of nonlinear effects in silica fiber, such as self-phase modulation (SPM) and cross-phase modulation (XPM), is due to the intensity dependence of the refractive index of optical fiber. If the nonlinear medium response instantaneously to intensity change, this nonlinearity is also known as Kerr nonlinearity (Okamoto, 2022). The refractive index of an optical fiber can be written as

$$\tilde{n}(\omega, |E|^2) = n(\omega) + n_2|E|^2, \tag{2.5}$$

where $n(\omega)$ is the linear refractive index, $|E|^2$ is the optical intensity inside the fiber and n_2 is the nonlinear-index coefficient related the third-order susceptibility $\chi^{(3)}$ given by the following equation,

$$n_2 = \frac{3}{8n} \chi^{(3)} Re(\chi_{xxxx}), \tag{2.6}$$

where Re denotes the real part of $\chi^{(3)}$. $\chi^{(3)}$ is also responsible for other lowest-order nonlinear effects, such as third-order harmonic generation and four-wave mixing.

It is important to note that for ultrashort pulses whose pulse widths are close to or smaller than 1 ps, which is the case in the mode-locked pulses in this thesis, the nonlinear effects governed by Equation (2.6) is not enough because higher-order nonlinearity, specifically the Raman effect, will shift the pulse spectrum to the lowfrequency side, which is called Raman-induced frequency shift (Agrawal, 2013b).

2.3 Nonlinear Pulse Propagation

When laser light of ample intensity travels through an optical fiber, the fiber's response to the light becomes nonlinear, leading to various intriguing nonlinear phenomena. This section delves into these nonlinear effects and their manifestation in the form of solitons within fiber lasers.

2.3.1 Pulse Propagation in Optical Fibers

Laser light, an electromagnetic field governed by Maxwell's Equations, undergoes nonlinear behavior when propagating within a silica fiber, especially at high intensities. This nonlinear response leads to various effects such as self-phase modulation (SPM), cross-phase modulation (XPM), four-wave mixing (FWM), stimulated Raman Scattering (SRS), and stimulated Brillouin scattering (SBS). Simultaneously, the interaction of laser light with the silica fiber induces a frequency-dependent response known as dispersion. Considering both nonlinearity and dispersion, the propagation of laser light within a fiber can be accurately described by the nonlinear Schrödinger equation (NLSE). The NLSE solution predicts the existence of bright solitons, which arise from the delicate balance between nonlinearity and dispersion, particularly in the anomalous dispersion regime.

However, the behaviour of laser light in an optical fiber is not solely governed by nonlinearity and dispersion; factors such as loss and gain also contribute. By incorporating these factors, the dynamics of light propagation within an optical fiber are described by the Gingzburg-Landau Equation (GLE), the solution of which gives rise to dissipative solitons.

2.3.2 Nonlinear Effects

Nonlinear effects occurring within a fiber laser cavity are categorized into elastic and inelastic effects, depending on whether there is energy exchange between the laser light

and the optical fiber. For the sake of simplicity in this analysis, two prominent effects are considered: SPM and XPM. These effects, governed by the third-order susceptibility $\chi^{(3)}$, play a pivotal role in the operation of most passively mode-locked fiber lasers.

Since the refractive index depends on the local intensity of light as described in Equation (2.5), an optical pulse modulates its own phase when propagating inside an optical fiber. This phenomenon is called SPM, which was found in 1967 (Shimizu, 1967). The phase change ϕ can be expressed as follows:

$$\emptyset(t) = \tilde{n}(t)k_0L = (n + n_2|E(t)|^2)k_0L, \tag{2.7}$$

where $k_0 = 2\pi/\lambda$ and L is the fiber length. The second term is the nonlinear phase shift $\phi_{NL}(t)$, which is caused by the SPM. The time dependence of $\phi_{NL}(t)$ indicates that the pulse is chirped inside a nonlinear fiber, which results in spectral broadening of a pulse. When a light propagates inside a fiber, the envelop of the pulse along the fiber is governed by the NLSE, written as in the following equation:

$$\partial z - 2\,\partial t_2 + \underline{i\,\partial A} \quad \underline{\beta^2\,\partial^2 A} \qquad {}^2A = 0, \tag{2.8}$$
$$\gamma|A|$$

where A is pulse amplitude which varies with propagation distance z and γ is the nonlinear parameter which depends on nonlinear refractive index n_2, wavelength and effective mode area. β_2 is the GVD parameter. When $\beta_2 < 0$, the solution of Equation (2.8) shows SPM leads to the formation of optical soliton. To sum up, the key mechanism of SPM is the Kerr Effect. It introduces symmetrical spectrum broadening and supports soliton (Agrawal, 2013b).

When two or more optical pulses of different wavelengths and polarizations are launched simultaneously in an optical fiber, the refractive index of one optical beam does not depend only on the intensity of that beam but also depend on the intensity of the co-propagating beams. If only two beams are considered, the nonlinear phase shift can be

written as Equation (2.9), the first term is caused by SPM and the second term of which is caused by XPM (Agrawal, 2013c).

$$\phi_{NL}(t) = n_2(|E_1(t)|^2 + 2|E_2(t)|^2)k_0L, \quad (2.9)$$

From the above equation, it's obvious that XPM always happens together with SPM and it's twice as effective as SPM for the same intensity.

Since there are more than one pulses propagating simultaneously in the fiber, coupled NLSE can be used to analyze the effects of XPM. The analysis shows that XPM can introduce modulation instability no matter the sign of the GVD coefficient. Also, XPM is responsible for asymmetrical spectral broadening of optical pulses. Besides, the solution of coupled NLSE indicates that XPM supports solitons pairs (also called bound state soliton). A vector theory of XPM can analyze optical fields launched and propagating with different states of polarization (SOP) in an optical fiber. It shows that XPM-introduced nonlinear birefringence can change SOP when the input field is nonlinearly polarized. Besides, XPM can introduce polarization-dependent spectral broadening, pulse trapping and optical wave breaking.

2.3.3 Solitons

"Soliton" was first introduced by Zabusky and Kruskal (1965), referring to localized solutions to integrable nonlinear systems. These solutions are remarkable because they stand for special kinds of wave packets that can propagate undistorted over long distances even after colliding with each other. In fiber optics, the integrable conventional solitons result from the balance between nonlinearity and dispersion and have a secant-hyperbolic time dependence. The mode-locked pulses in anomalous dispersion regime are referred to as soliton because they result from the balanced interplay of dispersion and nonlinearity, more specifically, the balance between GVD and SPM (Akhmediev et al., 2001). The presence of another pulse or higher-order nonlinear effects can be considered as a perturbation to this soliton.

Hasegawa and Tappert (1973a) theoretically predicted the existence of solitons using NLSE and Korteweg–deVries equation (KdV equation). These kinds of conventional solitons governed by NLSE are considered as bright solitons, which are characterized as intensity peaks in the time domain. Due to the bending and strains introduced birefringence in the fiber, two orthogonal polarization modes can propagate inside a single mode fiber. Menyuk (1987) first theoretically studied this phenomenon with coupled NLSE. The XPM between the orthogonally polarized modes could drastically alter the scenarios of soliton interactions and give rise to the formation of bound solitons (Oreshnikov et al., 2017). The experimental demonstration of bright solitons is plentiful. Recent demonstrations of bright soliton with different kinds of SMS structures in different operation regimes are also emerging (Chen et al., 2020; H. Li et al., 2019; H. Li et al., 2017; Wu et al., 2019; H. Zhang et al., 2019).

Dark solitons, to the contrary of bright soliton, always have intensity dips embedded in a continuous wave background. Dark solitons can be categorized as NLSE dark pulse, Cubic-Quintic nonlinear Schrödinger equation (CQNLSE) dark pulse, and Domainwalled (DW) dark pulse (Tiu et al., 2022). As NLSE dark pulse relies on the change of linear refractive index coefficient in the cavity, it is only function in normal dispersion cavity. Hasegawa and Tappert (1973b) theoretically predicted the NLSE dark soliton in normal dispersion regime. With sufficient light intensity to interact with higher-order nonlinearity, the CQNLSE dark pulse can be formed in both normal dispersion and anomalous dispersion regime. The DW dark soliton is due to the interaction of two or more lasing in different wavelength that causes the topological defects in temporal domain. DW dark soliton can also be formed in both normal dispersion and anomalous dispersion regime. Vladimir E Zakharov and Aleksei B Shabat (1973) first theoretically predicted the DW dark soliton. Recently, many experimental demonstrations of dark solitons with SMS structure were reported (G. Chen et al., 2021; Wang et al., 2024; Zou et al., 2019).

Until the 1990s, physicists realized that "solitons" also exist in non-integrable and non-conservative optical systems. This kind of solitons are called dissipative solitons. Unlike conventional soliton, which is the result of balanced interplay of nonlinearity and anomalous dispersion, dissipative soliton depends on the balance of gain and loss of the optical system (Grelu & Akhmediev, 2012). Dissipative solitons are governed by the Ginzburg–Landau Equation (GLE). One of the merits of dissipative soliton is that with a given set of predetermined equation parameters, the energy, profile, and chirp of a dissipative soliton are fixed no matter the initial conditions. This feature is highly desirable for applications, such as the generation of stable pulses trains by mode-locked cavities, or the in-line regeneration of optical data streams (Grelu & Akhmediev, 2012). Another merit of dissipative soliton is from the dissipative soliton molecules. Unlike the soliton molecules governed by higher-order NLSE, which are easily destroyed by external perturbations or additional effects such as third-order dispersion or Raman scattering, dissipative soliton molecules are robust multi-soliton structures that can be perfectly stationary, and its energy remains proportional to the number of single-soliton constituents.

Multiple solitons interaction is another subject that has been researched extensively. Multiple solitons could be formed in fiber laser due to wave-breaking effect, peak power clamping effect and soliton shaping of dispersive waves. Typical multiple solitons observed in fiber laser include soliton bunches, bound state of solitons and soliton rain. Bound state soliton, also known as soliton molecules, refers to two or more solitons bind together through direct soliton interactions. The study of bound solitons has progressed both theoretically and experimentally over the years. In theoretical research, (Malomed, 1991, 1992) theoretically studied the formation of bound state soliton with NLSE. Akhmediev et al. (1997) studied the formation of bound state soliton in complex GLE systems. Tang et al. (2009) found that the formation of multiple solitons was due to the peak power limiting effect by analyzing the light propagation in the weakly birefringent

fibers with coupled NLSE. Sakaguchi et al. (2018) reported the transformation of different kinds of bound solitons by simulating near zero-dispersion laser cavity using complex GLE with cubic-quintic nonlinearity and third order dispersion term. Recently, Kulagin and Shapovalov (2024) used NLSE with a nonHermitian term to simulate nonlinear optics system taking the environmental impact on the system into consideration. Though these theoretical studies and simulations showed the possibilities of different kinds of solitons, they used only limited sets of data, which cannot fully describe the phenomenon in experiments. Experiments reporting bound state solitons were also abundant (Gong et al., 2001; Guo et al., 2022; Lü et al., 2019; Muhamad Apandi et al., 2023; Stratmann et al., 2005; Yang et al., 2022). Tang et al. (2005) observed bound soliton pulses in fiber lasers employing NPE technology. Seong and Kim (2002) achieved fourth order bound solitons in a passively mode-locked fiber laser with a figure-of-eight cavity. Other researchers also demonstrated all-optical bit storage in fiber lasers through optically mechanically bound solitons (He et al., 2021; Pang et al., 2016). Specifically, bound state solitons with different kinds of SMS structures at different operation regime were reported (Fan et al., 2023; Gan et al., 2020; Gan et al., 2021; Lv et al., 2019; Ren et al., 2022; Zhang et al., 2022; Zhu et al., 2019). Zhu et al. (2019) obtained controllable tightly and loosely bound solitons using a hybrid no-core fiber (NCF)-graded index multimode fiber (GIMMF) structure. Wang et al. (2019) utilizing a similar NCF-GIMMF structure SA, reported the generation of pulsewidth controllable dissipative solitons and bound solitons with tunable spectral bandwidths at net-normal dispersion. Ren et al. (2022) experimentally observed conventional and bound solitons with GIMMF based artificial SA in 2.0 μm Tm-doped fiber laser. Experimental investigations into artificial SA have clearly indicated its diverse applications in generating various types of bound solitons. This pioneering research unveils the vast potential of artificial SA across a spectrum of soliton generation techniques, offering promising avenues for further exploration and innovation.

2.4 Multi-mode Interference

When light is introduced into an MMF, it stimulates a distinct array of MMF modes, each characterized by its unique propagation constants. As these modes traverse the MMF, they interact with one another to produce a phenomenon known as multimode interference (MMI). Consequently, the field distribution within the MMF at any given point results from the superposition of these individual mode fields, reflecting the complex interplay and interference among the excited modes along their propagation paths.

2.4.1 Self-imaging

Self-imaging in MMF was first observed by Allison and Gillies (1994). It is characterized by the periodic replication of an optical field. Although the superposition of the excited modes in MMF generally yields a complicated field distribution due to the MMI, self-imaging of the input field can be obtained at certain positions where the excited modes are in phase. Such positions satisfy the condition that the accumulated phase difference between any two excited modes is an integer multiple of 2π as analyzed by Zhu (2008). Similar results were reported by Nazemosadat and Mafi (2013a) in GIMMF.

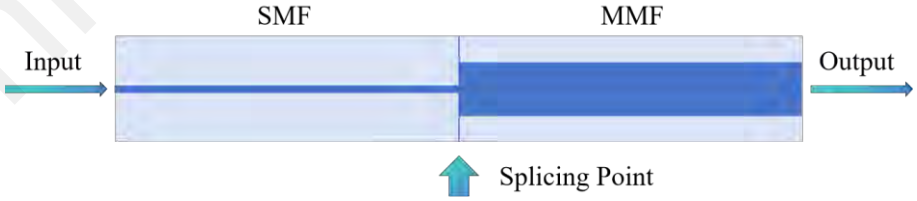

Figure 2.2: Schematic drawing of light coupling from an SMF to an MMF

At the splice point depicted in Figure 2.2, N modes are excited. These excited modes can be mathematically described by the following equation:

$$N$$

$$E_{sm}(r, \emptyset, z = 0) = \sum_{1} C_n e_n(r, \emptyset, z = 0), \quad (2.10)$$

where $E_{sm}(r, \emptyset, z = 0)$ is the fundamental mode of the SM fiber and $e_n(r, \emptyset, z = 0)$ is the n-th guided mode of the MMF. N is the excited modes inside the MMF. C_n is the mode expansion coefficient. Neglecting mode conversion, the excited modes propagate inside the MMF, and the field $E_{MM}(r, \emptyset, z)$ along the MMF can be expressed as

$$E_{MM}(r, \emptyset, z) = \sum_{1}^{N} C_n e_n(r, \emptyset, 0) e^{-i\beta_n z} = e^{-i\beta_1 z} \sum_{1}^{N} C_n e_n(r, \emptyset, 0) e^{-i(\beta_n - \beta_1) z}, \quad (2.11)$$

where β_1 and β_n are the propagation constants of the fundamental mode and the n-th excited mode of the MMF respectively. From Equation (2.11), it becomes evident that the replication of the input field will occur when the succeeding equation is satisfied for all N modes.

$$(\beta_n - \beta_1) z_{self-imaging} = \Delta\beta_n z_{self-imaging} = m_n 2\pi, \quad (2.12)$$

where m_n is an integer. Equation (2.12) implies that if the phase difference between any two excited modes is an integer multiple of 2π, the excited modes are in phase and a precise self-imaging of the input field occurs. However, because the excited modes have propagation constants that do not have multiple relationship, it is almost impossible to find a self-imaging position that exactly satisfy Equation (2.12) within a reasonable length of MMF (within several meters) in practice. For this reason, one usually pursues quasi-reproduction positions of input field, where the phase difference between the excited modes is slightly different from 2π but still have a high self-imaging quality, for example, more than 99% reproduction of the input field.

It should be noted that, due to the mode orthogonality and the on-axis excitation, only $LP_{0,n}$ modes in linear polarization approximation, are strongly excited in the MMF. Usually, the larger the core of the MMF is, the more modes can be excited and the longer

the self-imaging period. Thus, to obtain high quality self-imaging, when largecore MMF is used, the length of the MMF should be chosen with more consideration.

2.4.2 Spectral filtering

Consider a MMF with a specific length L, Equation (2.12) can be rewritten as

$$\Delta n_{eff,n} L = m_n \lambda_0, \tag{2.13}$$

where $\Delta n_{eff,n} = (\beta_n - 2\beta\pi 1)\lambda_0 = n_{eff,n} - n_{eff,1}$ and λ_0 is the operation wavelength of a specific intensity laser light. It is obvious from Equation (2.13) that the self-imaging from the output side only happens for a specific wavelength. This phenomenon is regarded as spectral filtering effect of NI-MMI.

As stated in section 2.2, due to the Kerr effect, β_n and β_1 are intensity dependent propagation parameters, Equation (2.13) can be further rewritten as

$$\Delta n_{eff,n}(I) L = m_n \lambda_0. \tag{2.14}$$

Hence, with increased intensity, the operational wavelength can be determined using the following equation:

$$\lambda_{high} = \frac{\Delta n_{eff,n}(I_{high})}{\Delta n(I_0)} \lambda_0. \tag{2.15}$$

The above equation highlights the spectral filtering effect inherent in an SMS structure. For GIMMF, Nazemosadat and Mafi (2013a) proposed employing the SMF-GIMMFSMF structure as a SA. Their numerical analysis revealed that, owing to NL-MMI, the SMF-GIMMF-SMF structure exhibits spectral filtering capabilities. This mechanism selectively attenuates low-power signals while permitting higher-power signals to propagate effectively.

2.5 Resonators

In the context of fiber lasers, a resonator is commonly referred to as a cavity. Fiber lasers can be constructed with various types of laser cavities, but two frequently utilized designs are the ring and figure-of-eight cavities. Ring cavities are particularly adept at achieving unidirectional laser operation. They dispense with traditional mirrors, resulting in an all-fiber cavity. The utilization of ring cavities in fiber lasers dates back to 1985. In its simplest form, a ring cavity comprises a loop formed by connecting two ports of a wavelength division multiplexing (WDM) coupler, encompassing the doped fiber, as depicted in Figure 2.3. To ensure unidirectional operation, an isolator is typically inserted within the loop. Additionally, for conventional doped fibers that do not maintain polarization, a polarization controller is necessary.

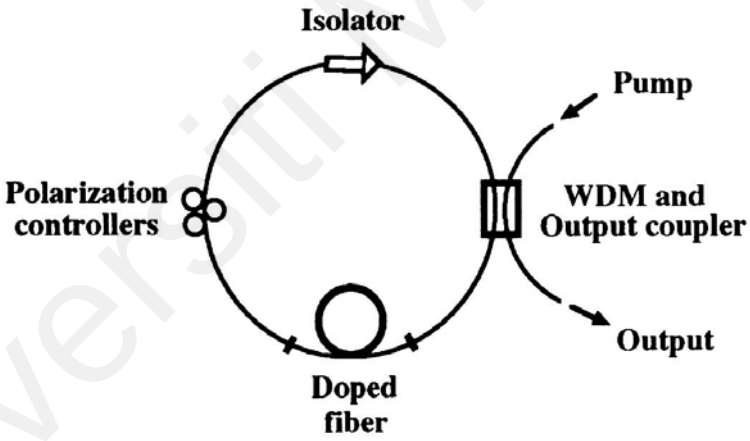

Figure 2.3: A fiber laser configuration with a ring cavity (Agrawal, 2008).

Figure-of-Eight resonator is another type of ring cavity. It is referred to as figure-of-8 cavity due to its appearance. A schematic drawing of figure-of-eight cavity is shown in Figure 2.4. The center coupler splits the laser light into two equal counter-propagating parts. The doped fiber is placed close to the center coupler to form a nonlinear amplifying-loop mirror (NALM). As a result, one part is amplified at the entrance to the loop, while the other undergoes amplification just before exiting the loop. The two parts of waves acquire different nonlinear phase shifts during each round trip inside the

NALM. If the phase difference is close to π, this center part of the pulse is transmitted, while wings of the pulse are reflected due to their lower power levels and smaller phase shifts. This results in a saturable absorber-like property. Thus, figure-of-eight resonator is often used for mode-locking.

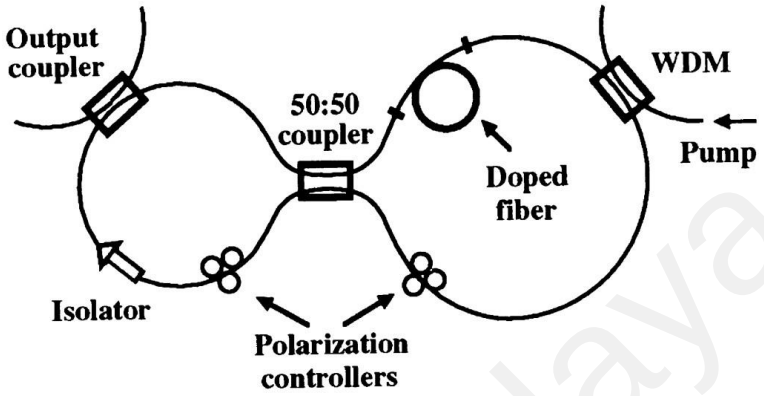

Figure 2.4: Example of doped fiber laser configuration with a figure-of-eight cavity (Agrawal, 2008).

2.6 Saturable Absorber

Saturable absorption is a nonlinear optical phenomenon that plays a pivotal role in the generation of ultrashort light pulses, such as passive Q-switching and Mode-locking lasers. An SA is an optical component that shows saturable absorption property. Real (or natural) SAs work on the absorption mechanism. When light interacts with a material, it can excite electrons to higher energy states (Marini et al., 2017). As the intensity of the incident light increases, more electrons are excited from ground state to higher energy states. Due to the finite number of energy states available for electron excitation within the material, the material eventually reaches the saturation point where it cannot absorb any more photons. When the intensity of the incident light decreases, electrons in the excited states can relax back to lower energy states and allows the material to return to its normal absorption behavior.

Artificial SAs on the other hand, do not really absorb electrons. They rely on the intensity dependent or polarization dependent nonlinear effects in the resonator. Due to these nonlinear effects, artificial SAs exhibit behaviors like real SAs, which decrease optical losses for higher intensities, thus allowing the higher intensity wave to pass through and blocking the lower intensity wave.

2.6.1 Real SAs

Commonly used SAs include semiconductor saturable absorber mirrors (SESAMs), carbon nanotubes (CNTs), graphene, transition metal dichalcogenides (TMDs), and black phosphorus (BP). SESAM is currently the most widely used SA in industry due to mature semiconductor technology for electronics. Keller et al. (1996) first invented SESAM and demonstrated the femtosecond mode-locking solid-state laser using SESAM as SA. Later, SESAM was used for Q-switching and mode-locking in microchip laser (Spühler et al., 1999) and fiber laser (Okhotnikov et al., 2004). Even though SESAM allows good control of the SA parameters, resulting in high stability and low noise pulses, it suffers from complex fabrication process, high cost and narrow operation wavelength range.

SAs based on single-walled CNTs were first demonstrated in 2003 (Set et al., 2003) and developed quickly since then because they are cheaper and low cost compared to SESAM. CNT-SAs are easy to be integrated in fiber laser systems and covers a broad operation wavelength (Martinez & Sun, 2013). The main challenge associated with CNT-SAs is their relatively large non-saturable losses. This drawback is obvious in solid-state lasers but was not a problem in fiber lasers.

Graphene SA is first demonstrated in 2009 (Bao et al., 2011). Graphene SAs are low cost and easy to fabricate. Besides, graphene SAs have a better ratio of modulation depth to non-saturable losses than CNT-SAs. The main advantage of graphene SAs over SESAM is still its ultra-broad operation wavelength range (Martinez & Sun, 2013). The

disadvantages of graphene SAs include relatively low saturation fluence at longer wavelengths and low modulation depth of single-layer graphene.

TMDs are one of the most studied two-dimensional (2D) saturable absorbers. They are composed of transition metal atoms, sandwiched between layers of chalcogen atom. TMD saturable absorbers offer several advantages, including their ultrashort response time, broadband operation, and robustness (Mohanraj et al., 2016). But its good performance is confined within the visible range due to a relatively large band gap (Wang et al., 2012).

BP is another kind of 2D material SA. Unlike graphene and TMDs, its band-gap can be tuned from ~0.3 eV (bulk) to ~2 eV (monolayer) flexibly by changing the layer number, thus it can bridge the gap between the zero band-gap of graphene and large band-gaps of TMDs (Li et al., 2016).

To sum up, each of these SAs has its own pros and cons, which gives researchers the motivation to study artificial SAs.

2.6.2 Artificial SAs

Artificial SAs are attracting more and more attention because they have many merits, such as low cost, easy to fabricate, wavelength independence, longevity, high damage threshold, and easy to integrate in optical systems. Most researched artificial SAs include nonlinear polarization rotation (NPR), nonlinear polarization evolution (NPE), nonlinear optical loop mirror (NOLM), nonlinear amplifying loop mirror (NALM), and
SMS structures.

NPR is one of the common artificial SAs employed for mode-locking. It relies on the fact that the refractive index of an optical fiber depends on the intensity and polarization of the light, thus the change of phase shift and state of polarization depends on the strength of light intensity. Since the polarization rotation of light changes accordingly to the light intensity, the NPR effect is regarded as an intensity dependent process. NPR technique was adopted to initiate mode-locking, literature on NPR works from 1 um to 3 um

wavelength regions are extensive (Dong et al., 2020; Gu et al., 2020; F. Wang et al., 2020; X.-f. Wang et al., 2021; X. Wang et al., 2018; B. Zhang et al., 2023). In fact, this technique can be used regardless of wavelengths, but it is sensitive to the condition of the fiber such as temperature, bending and vibration. NPR is a versatile pulsing technique where pulse profiles, from one form to another form can be switched easily by adjusting the light polarization. Many switchable pulse profiles as well as switchable wavelengths, Q-switched to mode-locked, fundamental to harmonic mode-locking, soliton filtering with of soliton Kelly sidebands and interchangeable soliton, dissipative soliton resonance (DSR) and noise like pulse (NLP) as well as switchable bright-dark pulse were demonstrated using NPR technique.

NPE is very similar to NPR. However, unlike NPR, NPE involves not only rotation but also changes in ellipticity and other polarization parameters. By placing a polarizer after the fiber, one can selectively transmit or reflect the pulses depending on their polarization state. By adjusting the polarizer angle, one can create a feedback mechanism that favors the formation of short and stable pulses. It is self-starting and self-adaptive, so it does not require any external triggering or seeding to initiate mode locking and can adjust to changes in the laser parameters. Additionally, it is compatible with a wide range of fiber types and can operate at different wavelengths. Furthermore, NPE is simple, robust, and low-cost, requiring only a fiber, a polarizer, and a coupler to implement. NPE has some challenges and limitations when used for mode locking that need to be considered. For example, NPE is sensitive to environmental fluctuations, such as temperature or humidity, that can cause instability or loss of mode locking. Additionally, it is nonlinear, meaning that it depends on the intensity and shape of the pulses, which can lead to complex dynamics that can degrade the quality or coherence of the pulses. Lastly, NPE is not universal and does not work for all types of lasers due to differences in gain media, cavity configurations, or nonlinearities.

Likewise, NOLM/NALM are also based on intensity transmission loss to operate as artificial SA. A NOLM is essentially comprised of a 2x2 optical coupler, whose two outputs are connected together to form a loop. Figure 2.4 shows the typical modelocking fiber laser using NALM. This configuration is often referred to as figure-ofeight (F8). For mode-locking, an asymmetrical loop is desired, and it can be achieved by inserting a gain medium in the ring. Input light will be spilt into clockwise (CW) and counterclockwise (CCW) direction. Light travelling in counterclockwise direction will be amplified first and propagate down the remaining loop. On the other hand, light in the clockwise direction will undergo amplification later. As a result, light in different directions will experience different amounts of nonlinear phase shift due to Kerr effect.

SMS structures acting as artificial SAs are based on the mechanism of NL-MMI. According to Equation (2.14) and (2.15), the nonlinear change of the refractive index originating from the optical Kerr effect leads to a change of the self-imaging wavelength in the MMF. In another word, the transmission spectrum of the SMS fiber device will change due to the Kerr effect of MMI. Consequently, the transmission of the SMS fiber device at a certain wavelength exhibits a performance similar to a saturable absorber. Specifically, the transmission increases at high laser power and attenuates at low laser power. Therefore, pulsed laser operation can be achieved at a wavelength where the SMS fiber device performs like a saturable absorber. SMS structures have many advantages. First, SMS structures are all-fiber structures, so they are easy to be integrated in fiber laser systems and have high damage threshold. This inherent merit is crucial for the stability of optical systems. In the meantime, the SMS structures are easy to fabricate, and usually very low cost compared with their real SA counterparts. Besides, it is easy to realize wavelength tunable laser with SMS structures.

With all the aforementioned merits, artificial SA has critical drawbacks as well. It is challenging to experimentally quantify and reproduce the performance of these artificial SAs, and they are typically sensitive to environmental perturbations.

2.6.3 SA Characterization

Nonlinear characterization and linear characterization are usually performed to evaluate the key parameters of SAs, out of which, modulation depth is the maximum possible change in optical loss specified in percent, non-saturable losses are the unwanted part of the losses which cannot be saturated, saturation intensity is the optical intensity that it takes in a steady state to reduce the absorption to half of its unbleached value.

Nonlinear characterization involves assessing the transmission/absorption, modulation depth, and non-absorption losses of a SA. To conduct this characterization, a balanced twin detector measurement technique is commonly employed. The setup, depicted in Figure 2.5, comprises several key components. Initially, a short pulse laser source generates pulses, which are subsequently amplified by an Erbium-doped fiber amplifier (EDFA). The amplified light is then divided equally by a 50/50 or 3-dB coupler, with one portion directed to the SA device for testing and the other portion routed to a power meter to serve as a reference. An attenuator is introduced to adjust the power launched into the SA device. Through this setup, variations in the SA's response can be precisely evaluated. By plotting a nonlinear transmission/absorption curve based on the collected data, the nonlinear characteristics of the SA can be thoroughly assessed.

This method provides valuable insights into the behavior of the SA under test, aiding in the optimization of its performance for various applications. The transmission curve can be described by

$$T(I) = 1 - \Delta T \times \exp\left(-\frac{I}{I_{sat}}\right) - \alpha_{ns}, \tag{2.16}$$

where T(I) is the transmission, ΔT is the modulation depth, I is the input intensity, I_{sat} is the saturation intensity and α_{ns} is the non-saturable loss.

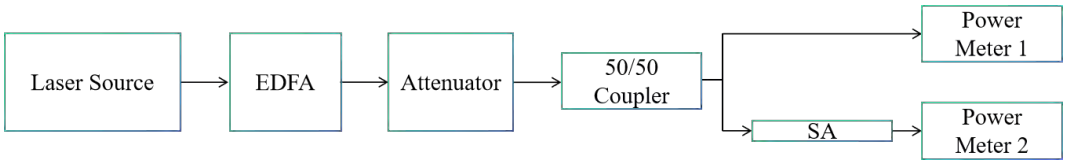

Figure 2.5: Schematic drawing of a balanced twin detector measurement method.

Linear characterization of a SA involves assessing its transmission at various wavelengths. The schematic diagram for linear characterization is illustrated in Figure 2.6. In the setup a white light source or amplified spontaneous emission (ASE) source is used as a light source while an Optical Spectrum Analyzer (OSA) is utilized to examine the difference in transmission with and without the SA. By comparing the results, the transmission spectrum of the SA can be deduced. Notably, when MMF is involved, the transmission spectrum may exhibit a periodic interference pattern due to NL-MMI among the different modes propagating through the MMF. This interference phenomenon adds complexity to the transmission characteristics, reflecting the intricate interactions between the diverse modes within the MMF.

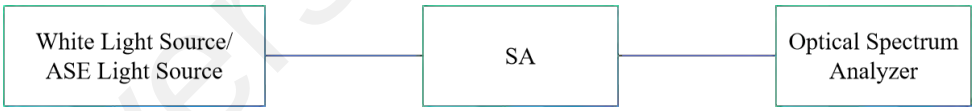

Figure 2.6: Measurement of linear absorption for a SA.

2.7 Generation of Short Pulse in Fiber Laser

Two techniques used to generate short, pulsed fiber laser are known as Q-switching and mode locking. Both can be initiated actively and passively. In this section, literature on passively Q-switched and Mode-locked pulses is paid special attention. Specifically, research on several kinds of special mode-locked pulses is presented here.

2.7.1 Q-switching Operation

The quality factor of a cavity or its Q-factor measures how ideal or lossless the cavity resonator is. When the Q factor of a laser resonator (based on its resonator losses only) is abruptly increased, an intense laser pulse can be generated. This technique of pulse generation is called Q-switching. Since its first demonstration in the 1960's, Q-switched operation has attracted much attention due to its various application possibilities in remote sensing, medical surgery, defense, optical communication, and material processing. Q-switching technique can be used to generate microsecond to nanosecond pulses with high energy and high peak power. The pulse repetition rate of a Q-switched pulse typically ranges from 1-100 kHz and the peak power can reach extremely high at gigawatt level.

Q-switched operation works on the mechanism of modulating the intracavity losses and thus the Q factor of the laser resonator. Q-switch can be considered as some kind of attenuator which can switch on and off to modulate the loss to high (low Q-factor) or low (high Q-factor). At the beginning, the Q-switch functions to prevent light feedback to the gain medium, maintaining a low Q-factor in the optical resonator and causing a population inversion. At this moment, the lasing cannot begin because there is no feedback in the resonator. When the amount of energy stored in the gain medium reaches the maximum or gain saturated, the Q-switch quickly changes the resonator Qfactor from low to high, causing the stimulated emission to begin. Due to the large amount of energy built in the gain medium, the intensity of light in the resonator builds up quickly and depletes also quickly. This process results in a short pulse with high peak intensity, which is known as a Q-switched pulse.

Q-switching can be achieved actively and passively. Active Q-switching uses acousto-optic device, magneto-optic effect device or electro-optic device as a modulator to control the Q-factor in the resonator. The advantage of this method is good control of the pulse characteristics, such as repetition rate, pulse width and wavelength (Wang & Xu, 2007). However, active Q-switching has complicated optical systems and is expensive (N. Li et

al., 2021). Passive approaches are preferable due to their simplicity, compactness, and low cost. Different kinds of SAs used for passive Q-switching together with their working mechanisms are presented in section 2.4.

The use of SMS structures as artificial SA for Q-switched pulses generation was first demonstrated by Fu et al. (2015) with a segment of 4.9 cm SIMMF sandwiched by SMFs. The repetition rate, pulse energy and pulse duration were 35.2 kHz, 0.78 μJ, and 3.86 μs respectively. Later, researchers used doped-fiber to build SMS structure for Qswitching operation (S. Li et al., 2019) and wavelength tunable Q-switching operations (P. Zhang et al., 2023). The doped fibers have smaller core diameter compared with SIMMF and GIMMF, which means that the self-imaging interval length is shorter than SIMMF and GIMMF based SA, but previous results showed that Q-switching occurred without special care on the doped fiber lengths. SIMMF based SMS structure was also used for dual-wavelength (Noor et al., 2022) and wavelength tunable (N Li et al., 2021) Q-switching operations. N. Li et al. (2021) demonstrated a nanosecond pulse width Qswitched pulse with SIMMF based SA, showed that SIMMF based SA is a promising candidate for nanosecond Q-switched operation.

2.7.2 Mode-locking Operation

Mode-locking refers to the technique of locking multiple longitudinal modes in a laser cavity. By synchronizing the phase of different modes, pulsed laser can be produced. Mode-locking generates ultra-short pulses with durations on the order of picoseconds or femtoseconds, and the repetition rate ranges from several megahertz to gigahertz.

As Q-switching, mode-locking can be achieved actively and passively. Active modelocking mainly works by modulating the internal losses in a resonator (Paschotta, 2008). However, due to the limited bandwidth of the modulator, active mode-locking typically only results in pulse width in the range of 10-100ps. Passive mode-locking with SA is more effective in pulse shaping. Most commonly used passive mode-locking

method are additive pulse mode-locking (APM) and Kerr-lens mode-locking (KLM). In fiber laser, APM is due to the interference of co-propagating pulses. KLM is due to the Kerr effect, because of which, the high intensity part of the laser beam is focused while the low intensity part is unfocused. When this beam passes through an aperture, the low intensity part will be attenuated, thus the pulse is shortened (Haus, 2000). Both APM and KLM lead to the effect resembles that of fast SA. Because the Kerr effect is very fast, KLM is suitable for ultrashort pulse generation. According to the master equation by Haus et al. (1991), the pulse shape of a hyperbolic secant shape. This shape is used to fit the pulse in autocorrelation. SMS structures work on the mechanism of Kerr effect and also on the interference of the pulses.

Myriads of experiments were performed with SMS structures to mode-lock lasers. Ding et al. reported the first theoretical model that treats a large core fiber structure as an SA for mode-locking and demonstrated mode-locking with a segment of SIMMF (Ding et al., 2011). Other researchers later experimentally demonstrated mode-locking with a GIMMF based SMS structure as artificial SA (Nazemosadat & Mafi, 2013a, 2013b). Recently, groups of researchers managed to demonstrate mode-locking at different operation wavelength regimes (H. Li et al., 2019; Qi et al., 2022; Ren et al., 2022; Thulasi & Sivabalan, 2021), with different kinds of solitons (Sobon et al., 2016; Wang et al., 2022; Zhao et al., 2018), and in anomalous and normal dispersion regimes (Lv et al., 2019), with different kinds of SMS structures (Qi et al., 2022; Yang et al., 2018).

To evaluate the quality of mode-locked pulses, the time-bandwidth product (TBP) is often used. It indicates how close a pulse is to the transform limit. For $sech^2$-shaped pulses and Gaussian-shaped pulses, the transform limits are about 0.315 and 0.441 respectively. The closer the TBP value is to these numbers, the closer the pulse is to the pulse duration lower limit. Larger values of TBP indicate the pulses are chirped. TBP is calculated as follows:

$$c\,\lambda \qquad = \Delta\upsilon \cdot \Delta\tau = \frac{}{2} \cdot \Delta\lambda \cdot \Delta$$

$$TBP\tau, \tag{2.17}$$

where $\Delta\upsilon$ is the spectral width in Hz, $\Delta\tau$ is the pulse width in second (Full width half maximum, FWHM), c is the speed of light in vacuum, λ is the operation center wavelength, and $\Delta\lambda$ is the 3 dB bandwidth.

2.8 Summary of research gaps

From the previous sections in this chapter, it is obvious that pulse formation dynamics in fiber lasers were extensively studied, and the pulse formation techniques were formed. SA, especially real SA, as the key component in pulse formation, was explored by many researchers. However, SMS structure was not systematically studied previously. SMS structure, as the new emerging artificial SA, has many advantages that are worthwhile to be studies, which leads to the motivation of this thesis: to systematically evaluate SMS structure performances in generating different kinds of ultrashort pulses.

CHAPTER 3: Q-SWITCHED AND MODE-LOCKED PULSES GENERATIONS WITH SMS STRUCTURE AS ARTIFICIAL SA

3.1 Introduction

Fiber lasers hold great promise across various scientific and industrial domains, commanding a significant portion of the commercial laser market. They can be categorized into continuous and pulsed types based on their mode of operation. Pulsed fiber lasers, characterized by high pulse energy and short pulse width, have substantially broadened the laser's applications in fiber-optic communication, medical devices, laser cutting, automotive manufacturing, and beyond. Pulsed laser generation primarily relies on two techniques: Q-switching and mode-locking, both of which can be implemented actively or passively, as discussed previously. Passive methods have garnered increasing attention in recent years due to their simplicity, compactness, flexibility and cost-

effectiveness. This approach involves incorporating a saturable absorber (SA) into the resonant cavity, emphasizing the important role of SAs in passive Q-switched and mode-locked fiber lasers.

The advancement of passive pulsed lasers heavily relies on real SA materials. In this context, investigation on the generation of Q-switched and mode-locked pulses using an artificial SA based on the structure of single-mode fiber (SMF) - multimode fiber (MMF) – SMF or SMS are conducted. These pulse operations are demonstrated in an Erbium-doped fiber laser (EDFL) operating within the net anomalous dispersion regime. To create the SMS structure, a segment of multimode fiber is fusion spliced into the cavity, flanked by SMFs on each side. Leveraging the Kerr effect of nonlinear multimode interference, Q-switching, mode-locking, and harmonic mode-locking operations were observed.

The generation of Q-switched pulsed laser involves intra cavity loss management. In the context of using the SMS structure as artificial SA, the cavity loss could be managed by simply twisting the MMF or by increasing the core diameter of the MMF. In the current work, the loss was managed by both bending the MMF and by using the large core SIMMF. Due to the mechanism of Q-switching, the efficiency slope of the Qswitching operation is usually smaller than the mode-locking operation and the operation wavelength tends to move to shorter lengths. Here, an experimental demonstration of the Q-switching operation using SIMMF based SMS structure as artificial SA is presented.

Passive mode-locking operation in anomalous dispersion regime usually leads to conventional bright soliton with Kelly sidebands. The pulse width of this mode-locked laser can reach femtosecond level, and the repetition rate is usually higher than Qswitched pulses. To further increase the repetition rate of a mode-locked laser, harmonic mode-locking (HML) is an effective way. By controlling the parameters of the fiber laser cavity,

HML operation can be realized, usually at a relatively higher pump power than fundamental mode-locking.

This chapter is arranged as follows: section 3.2 discusses Q-switched operation with SIMMF based SMS structure. Section 3.3 presents the mode-locked operation in EDFL with conventional solution with GIMMF based SMS structure. Section 3.4 presents the HML operation in EDFL with conventional soliton, also with GIMMF based SMS structure. Section 3.5 discusses finding of this chapter and section 3.6 concludes this chapter.

3.2 Q-switching Operation Using SIMMF Based Artificial SA

SIMMF is one kind of MMF whose refractive index is uniformly distributed in the core. The light propagates in SIMMF in a zigzag form and causes large modal dispersion. The large core diameter of SIMMF supports multi-modes co-propagating inside it and interfere with each other, resulting in an intensity dependent transmission analogous to a real SA. Extensive theoretical study shows that SIMMF spliced with
SMF structure can be used as artificial SA for Q-switching operation (Zhu, 2008).
However, experimental demonstration of Q-switching operation with SIMMF is few (Fu et al., 2015).

3.2.1 Mechanism of Q-switching Operation Based on SMS structure.

When laser light propagates from SMF (core diameter 8.3 μm) to SIMMF (core diameter 105 μm), because the core diameter of SIMMF is significantly larger than that of the SMF, the mismatched cross-sections at the splicing points may cause mode excitation and coupling. Because of the Kerr effect, which came into play as the input intensity of light increases, the refractive index of the core of the SIMMF was changed. When the intensity was low, the refractive index remained relatively constant. However, at higher intensities, the nonlinear refractive index change can cause the SIMMF's core

to behave differently. It can shift the conditions at which interference occurs, effectively reducing the coupling of light into specific modes. This shift results in an increased transmission of light at high-intensity levels, making the SMS structure behave like an SA.

3.2.2 Experimental Arrangement

The experimental arrangement includes two parts. First, fabrication and characterization of the SMS structure shall be done. After the SMS structure is fabricated and characterized, the SMS structure shall be put in a ring cavity for Qswitching operation. A 158 mm long SIMMF was used to form the SMS structure. The SMS structure is shown schematically in Figure 3.1. A 158 mm long SIMMF (Thorlabs, FG105LVA) was fusion spliced with two segments of SMFs (Corning, SMF-28) on each side (Splicer model: Fujikura 90S+). The loss on each of the splicing points were 0.01 dB and 0.02 dB respectively. The SIMMF has core and cladding diameters of 105 µm and 125 µm respectively. The SMF has core and cladding diameter of 8.2 µm and 125 µm respectively. The three segments of fibers together formed the SMS structure.

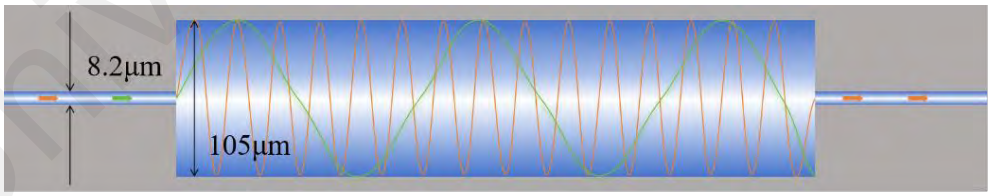

Figure 3.1: Schematic drawing of SIMMF based SMS structure.

To evaluate the characteristics of the SIMMF based artificial SA, the linear and nonlinear characterization were performed. A home-made amplified spontaneous emission (ASE) laser was used for the linear characterization. Figure 3.2 presents the spectral transmission characteristic of the SMS structure. It's obvious that the spectral transmission has a periodic interference pattern. This pattern is due to the multimode

interference induced by the several excited modes as the laser light propagates from SMF into the SIMMF.

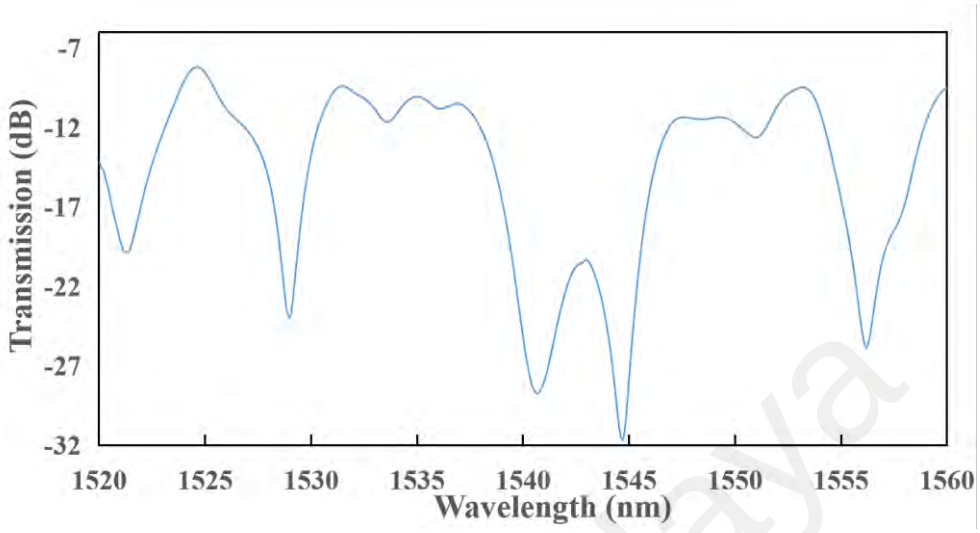

Figure 3.2: Spectral transmission of the SIMMF based SA.

A balanced twin-detector system was then used to measure the modulation depth and saturation intensity of the SMS structure. A homemade laser operating at a center wavelength of 1567 nm, pulse width of 700 fs and repetition rate of 21.73 MHz was used as the laser source. The nonlinear transmission curve was fitted by Equation (2.16). The experiment result is shown in Figure 3.3. It shows that modulation depth is 2.3%, which shows a not significant change before and after the SMS structure. This might be because of the poor coupling quality in between the SIMMF and SMFs. Another possible reason might be because the competing nonlinear effects like SPM or XPM interfere with the saturable absorption process, thus reducing the modulation depth. The saturable intensity is 9 MW/cm^2, showing a low saturation threshold. The non-saturable absorption is 81.2%, which is very high non-saturable absorption. This is likely due to bending and splicing causing large loss.

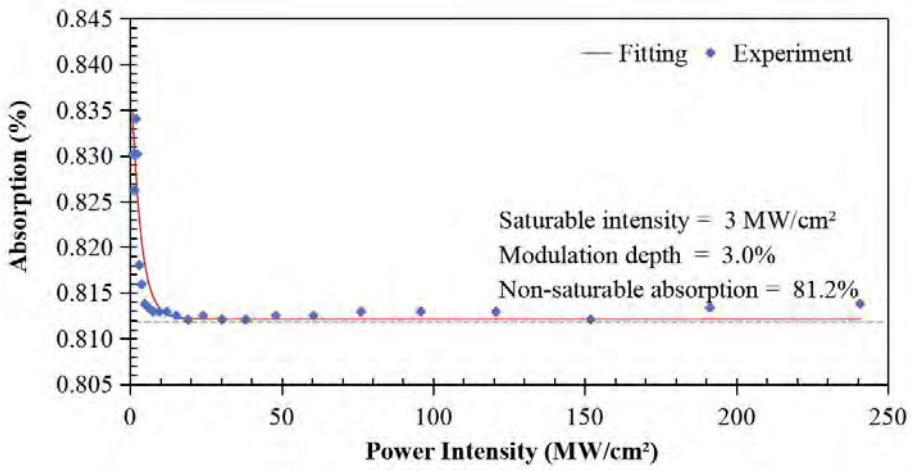

Figure 3.3: Absorption curve of the SIMMF based SA.

After the SMS structure was characterized, it was spliced in a ring cavity. Figure 3.4 shows the schematic diagram of experimental setup for Q-switching. The continuous wave laser diode (LD) provides a maximum output power of 343 mW at 975 nm (II-VI, Model LC96Z400-74). The LD was spliced with a 980/1550 nm wavelength division multiplexer (WDM). A 2 m long Erbium-doped fibre (EDF, Fibercore I25) acting as the gain medium was connected to the cavity after the WDM. The output of gain medium was then connected to a polarization insensitive isolator to ensure a unidirectional operation of the laser light. The SMS structure acting as the artificial SA was fusion spliced into the cavity after the isolator. The SIMMF part of the SA was then placed into an in-line PC to minimize the bending of the SIMMF. The in-line PC can also apply proper stress and strain on the SIMMF and control the polarization of the oscillating laser when necessary. An 80:20 coupler was placed after the SMS as feedback to the cavity and output port. The 20% of oscillating light was tapped out from the ring cavity for further analysis. The optical spectrum was analysed by optical spectrum analyser (OSA) (Anritsu, MS9710C) with a resolution of 0.02 nm. A highspeed photodetector (ET-3500F) attached to digital oscilloscope (GW Instek, GDS-3352) to monitor the real time signal in temporal domain. The stability of the Q-switching operation is checked in frequency domain, using radiofrequency (RF) spectrum analyser (Anritsu, MS2830A).

The total length of the cavity was about 9.6 m which included the gain medium, SIMMF and the single-mode fibers.

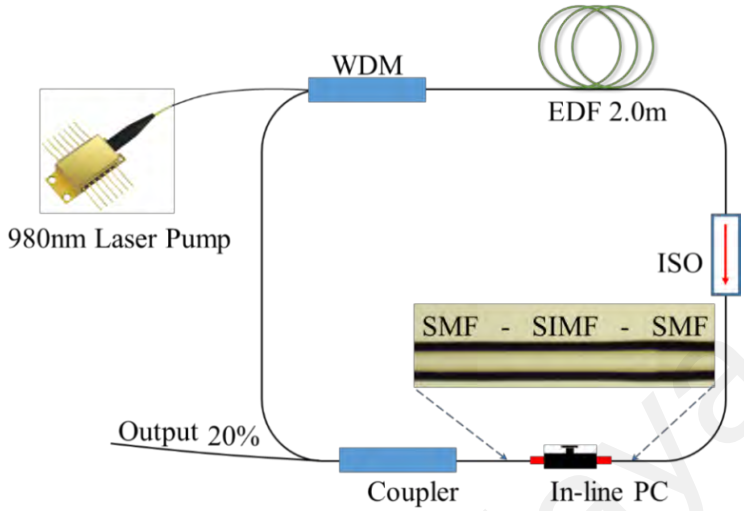

Figure 3.4: Schematic diagram of experimental setup of the ring cavity for Qswitched pulse generation using SIMMF as artificial SA. (Inset: microscope image of the SMS structure and its splicing point.)

3.2.3 Q-switching Performance by Using SIMMF Based Artificial SA

The performance of Q-switching laser operation based on the proposed SMS structure as an artificial SA was investigated. The Q-switched laser pulses were observed at threshold input pump power of 115 mW. The relatively high threshold was due to the high loss of the SMS structure. The Q-switched laser operation was maintained up to the maximum pump power of 343 mW. It is worth noting that no pulses were generated when the SMS structure was removed from the cavity.

The characteristics of the Q-switched pulse laser were thoroughly examined. Operating at 1530 nm, the laser maintained a consistent wavelength across various input pump powers, as illustrated in Figure 3.5. This wavelength was deliberately chosen for its optimal gain to counterbalance losses within the SMS structure. However, the selfimaging phenomenon induced by the SIMMF's large core diameter resulted in suboptimal output quality. Consequently, the spectrum exhibited numerous lower intensity peaks spanning from 1530 nm to 1580 nm.

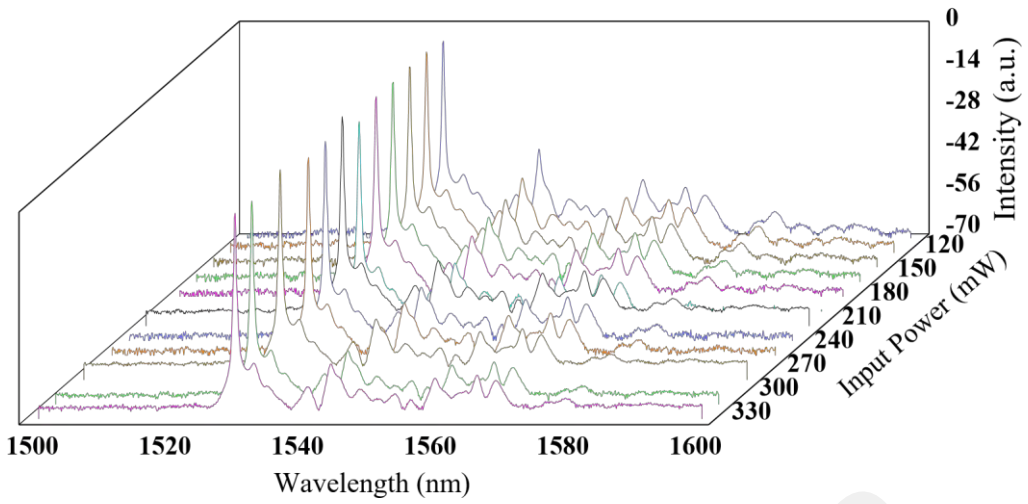

Figure 3.5: Spectrum of Q-switched operation using SIMMF based artificial SA with variation of input pump power.

A typical pulse waveform at 343 mW is shown in Figure 3.6(a). It indicates a stable output pulse train with no noticeable intensity fluctuations. Figure 3.6(b) shows the dual-pulse envelope of the enlarged pulse train, which indicates the pulse period and duration of 6.3 µs and 2.4 µs, respectively. The pulse period corresponds to the repetition rate of 157.7 kHz.

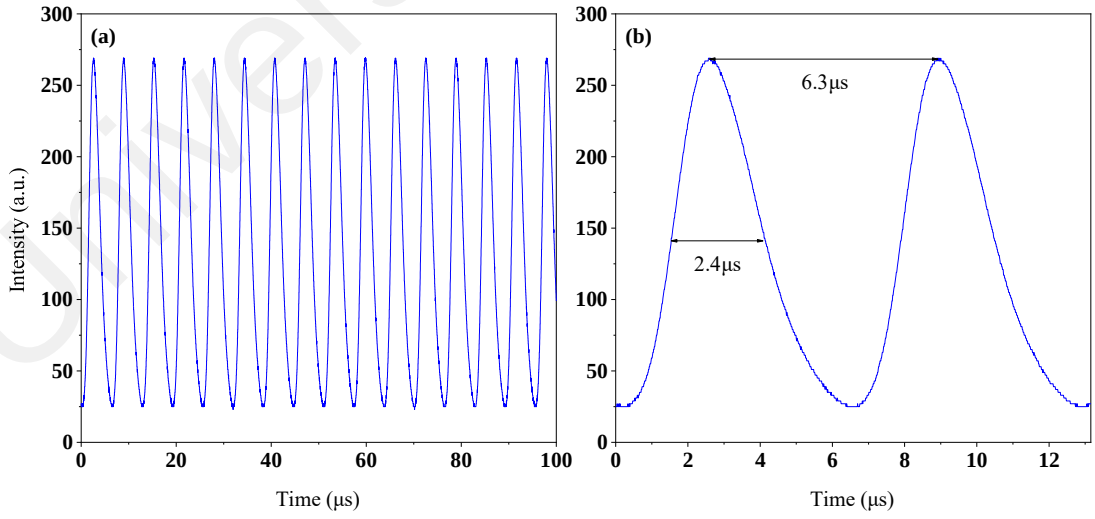

Figure 3.6: (a)Typical pulse train of Q-switched operation with SIMMF based artificial SA; (b) Dual-pulse envelope of the enlarged pulse train.

The RF spectrum of the output laser at 343 mW pump power is shown in Figure 3.7.

It shows a signal to noise ratio (SNR) of 72 dB at the fundamental frequency of 157.7 kHz, indicating the high stability of the laser. At least 13 harmonics were recorded within a frequency span of 1.8 MHz. This further verifies the stability of the Qswitching operation.

To further investigate the long-term stability of the Q-switched pulsed laser, the cavity was run at the maximum power of 343 mW in the laboratory environment for 5 hours and spectrum data was taken every half an hour. The result is shown in Figure 3.8. The spectra barely changed during the measurement process, which demonstrated that the pulse was very stable in a laboratory environment. The laser was also left to operate in the laboratory condition for more than 24 hours, and no noticeable degradation of performance was observed. This further demonstrates the good longterm stability of the Q-switching operation utilizing the proposed SMS structure as artificial SA.

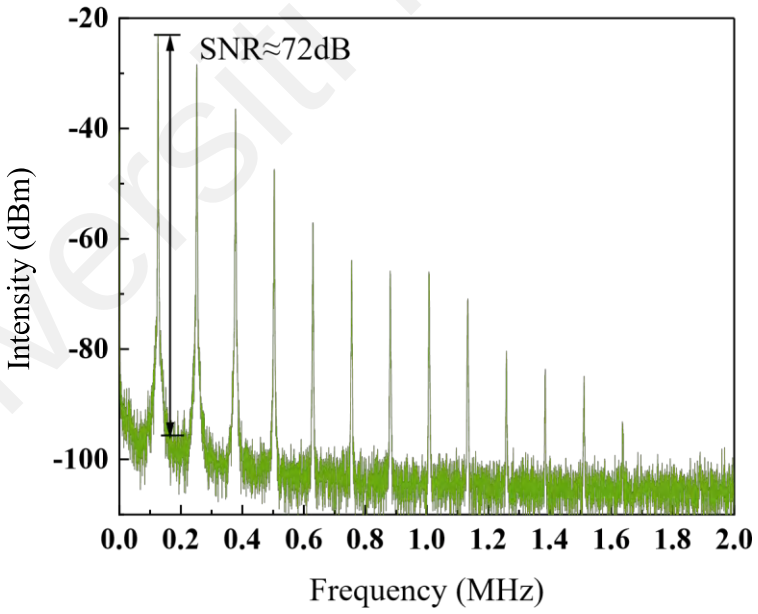

Figure 3.7: RF spectrum of Q-switching operation using SIMMF based artificial SA.

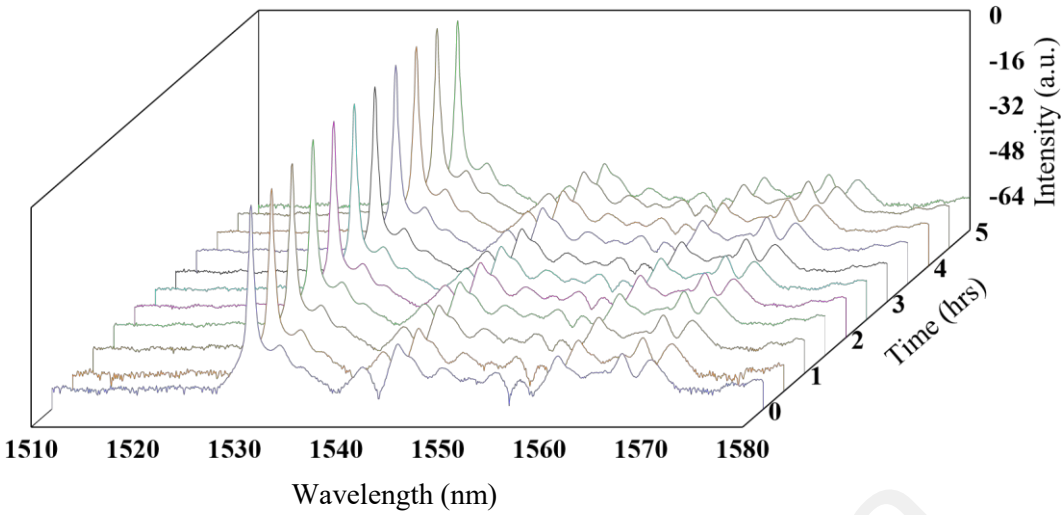

Figure 3.8: Long-term stability of the Q-switched operation.

Figure 3.9 presents the variation of repetition rate and pulse width at different pump power. As shown, the repetition rate increased from 87.4 kHz to 157.7 kHz, while the pulse width was reduced from 4.2 µs to 2.4 µs as the pump power changed from 115 mW to 343 mW. This behavior is typical for a Q-switched fiber laser, where the pulse width reduction is due to the gain compression that occurs in the laser cavity as the pump power is increased.

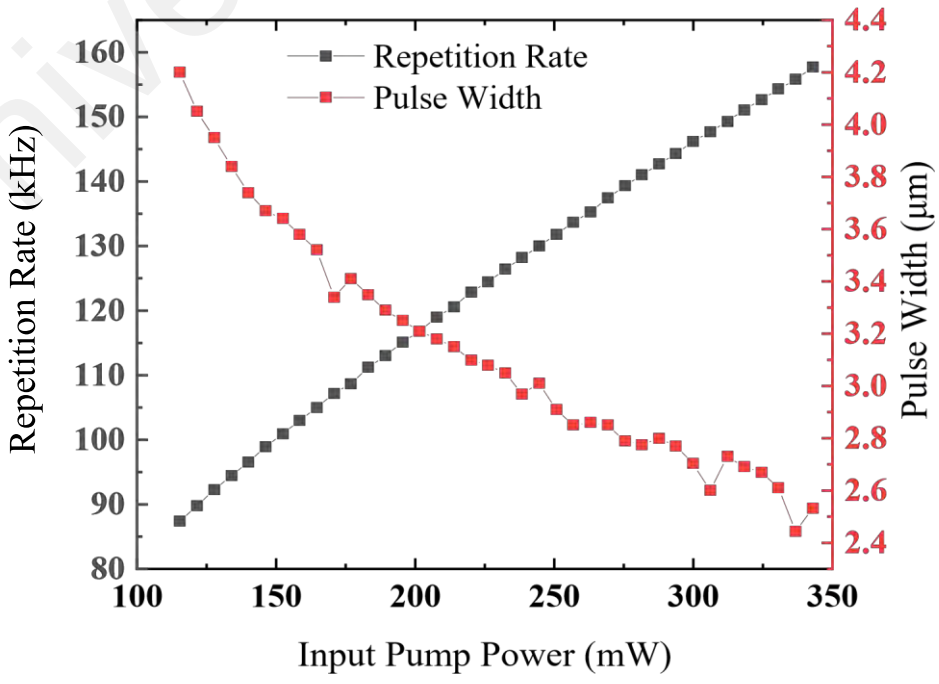

Figure 3.9: Average output power and pulse energy of the Q-switched laser with

respect to the pump power.

Figure 3.10 shows the average output power and pulse energy of the Q-switched laser with respect to the pump power. The output power was linearly increased from 0.61 to 2.35 mW with ascending pump power from 115 mW to 343 mW, while the pulse energy increased from 7.0 nJ to 15.0 nJ within the same range. The slope efficiency is about 0.8%, which is very low due to the high loss in the cavity.

Compare this work with recent works on Q-switched pulse with SMS structures, this work shows a relatively low pulse width.

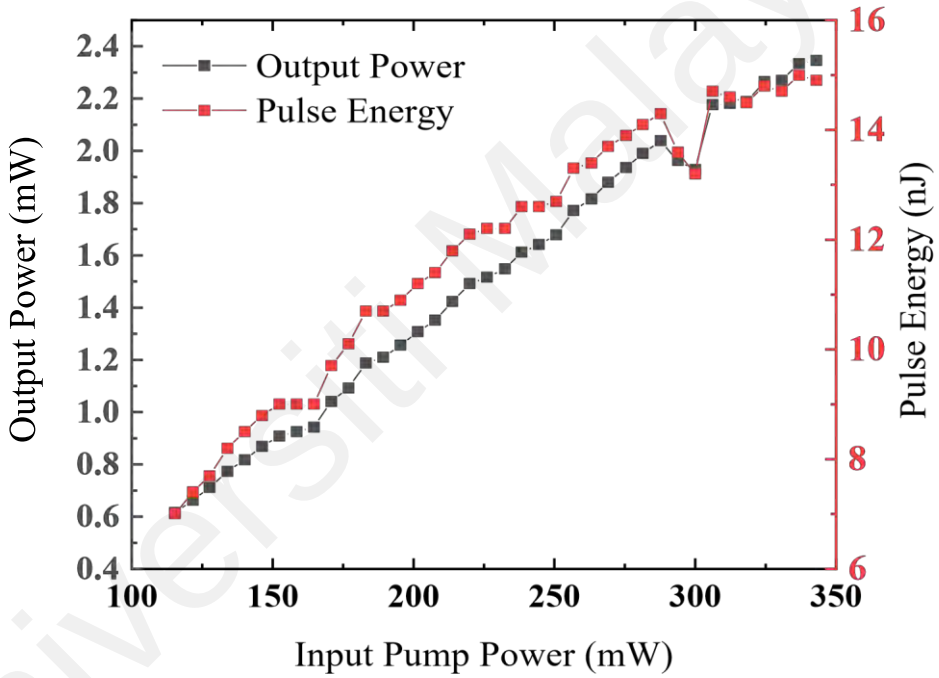

Figure 3.10: Average output power and pulse energy of the Q-switched laser with respect to the pump power.

To sum up, a stable Q-switched laser pulse was successfully achieved by incorporating an SMF-SIMMF-SMF structure as artificial SA in the EDFL cavity. The operation can withstand high pump power and generate single pulse energy up to 15 nJ, which is an order higher than mode-locked fiber lasers, demonstrating the high pulse energy characteristics of Q-switched pulses. Due to the pump power limitation of the current device, it is not possible to detect the power limit of this structure. But since this is an all-

fiber structure, it is expected to have a very high damage threshold, which thus is likely to support nanosecond Q-switched pulses at higher pump power. Also, this operation shows good long-term stability in the absence of disturbance, indicating the possibility of the proposed structure being used in real applications as artificial SA. Besides, this proposed SMF-SIMMF-SMF structure as artificial SA is simple, low cost, and provides good stability of laser, which makes it a good candidate for Q-switched pulse generation. However, it should be noted that even though the Q-switched operation has good long-term stability, the proposed SMS structures were observed to be notably more sensitive to environmental changes than thin film SAs, which may cause long-term stability problems in real practice.

3.2.4 Q-switching Performance Comparison with MoS_2 based real SA

To further assess the effectiveness of the SMS structure as an artificial SA, this subsection presents the results of Q-switching operations utilizing thin film of MoS_2 as the SA for comparison. The thin film MoS_2 SA was fabricated via electro-deposition on a thin film, as detailed by Hong et al. (2023). The linear and nonlinear characteristics of the thin film MoS_2 SA can also refer to the work of Hong et al. (2023). The schematic diagram of the cavity setup for Q-switching employing MoS_2 as SA is depicted in Figure 3.11. A continuous-wave laser diode (LD) with a maximum output power of 343 mW at 975 nm (II-VI, Model LC96Z400-74) served as the input pump. The gain medium utilized was a 2-meter-long EDF (Fibercore I25)

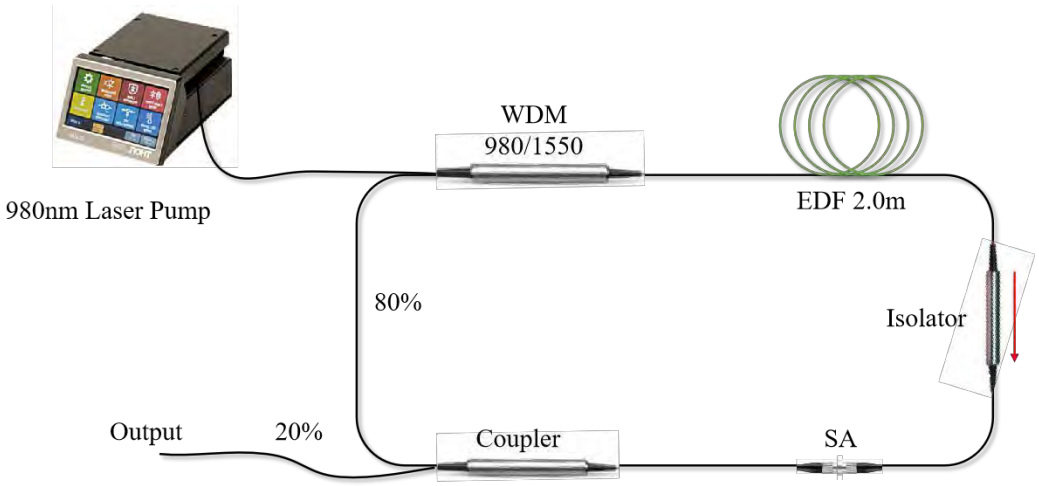

Figure 3.11: Schematic drawing of the cavity setting for Q-switching using MoS_2 as SA.

The Q-switching started at 35.5 mW input power and sustained until 72.4 mW before the pulse width started to increase. The Q-switched pulse operated at ~1564 nm and the operating wavelength had a ± 0.2 nm fluctuation with the variation of input pump powers as shown in Figure 3.12. Compared with the Q-switching operation of the SMS structure as artificial SA at 1530 nm, the operation wavelength moved to longer wavelength due to the lower gain needed to compensate for the loss.

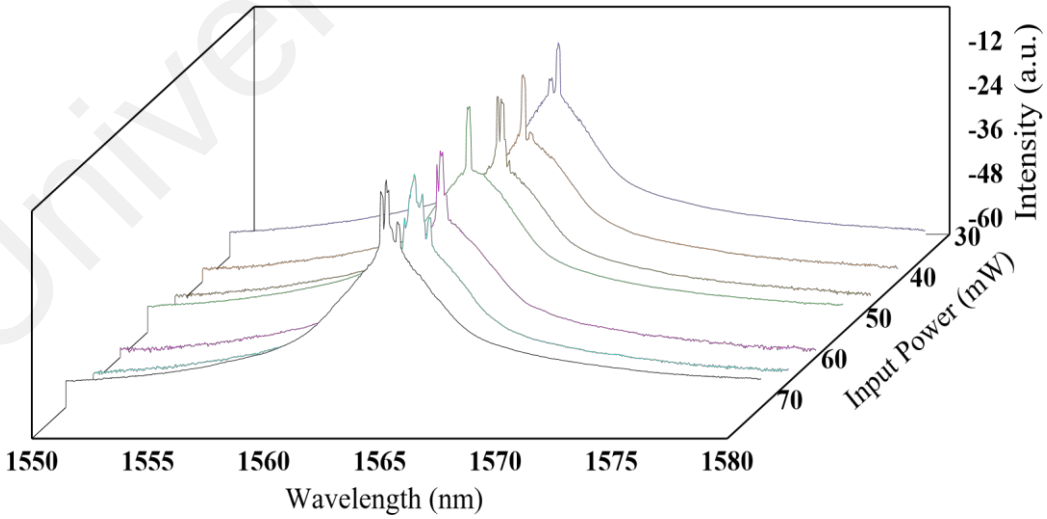

Figure 3.12: Spectrum of Q-switched operation using MoS_2 as SA with variation of input pump power.

The pulse train at the maximum power of 72.4 mW is shown in Figure 3.13(a). It indicates the pulse train is stable with no noticeable intensity fluctuations, same as Qswitching operation with SMS structure. Figure 3.13(b) shows the enlarged pulse train, which indicates the pulse period and duration of 16.1 μs and 3.17 μs, respectively. The corresponding repetition rate is 61.2 kHz.

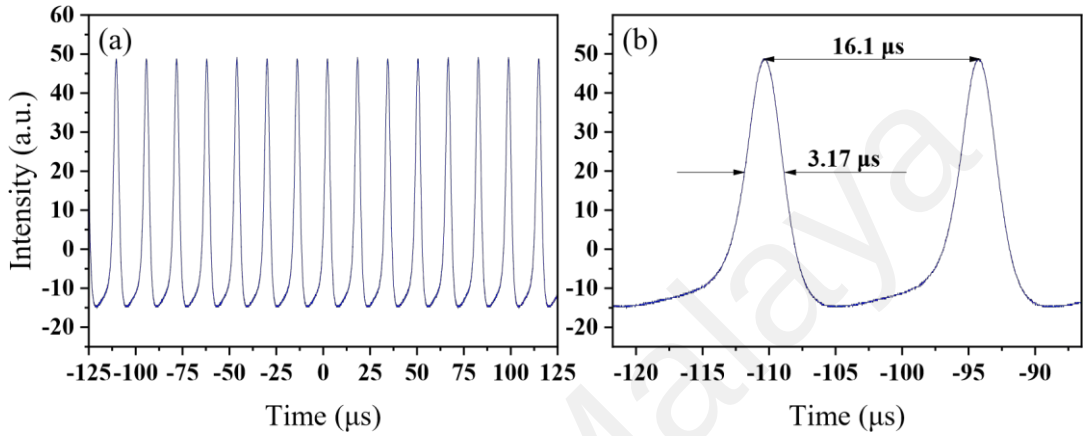

Figure 3.13: (a) Pulse train of Q-switched operation with MoS_2 as SA; (b) Dual-pulse envelope of the enlarged pulse train.

The RF spectrum of the output laser at 72.4 mW pump power is shown in Figure 3.14. It shows an SNR of 56 dB at the fundamental frequency of 61.2 kHz, which is a bit lower than the SNR with of Q-switching operation with SMS structure in section 3.2.3. The Q-switched pulse was left to run in the lab for 24 hours, and no noticeable decrease of the SNR was found, indicating a good long-term stability.

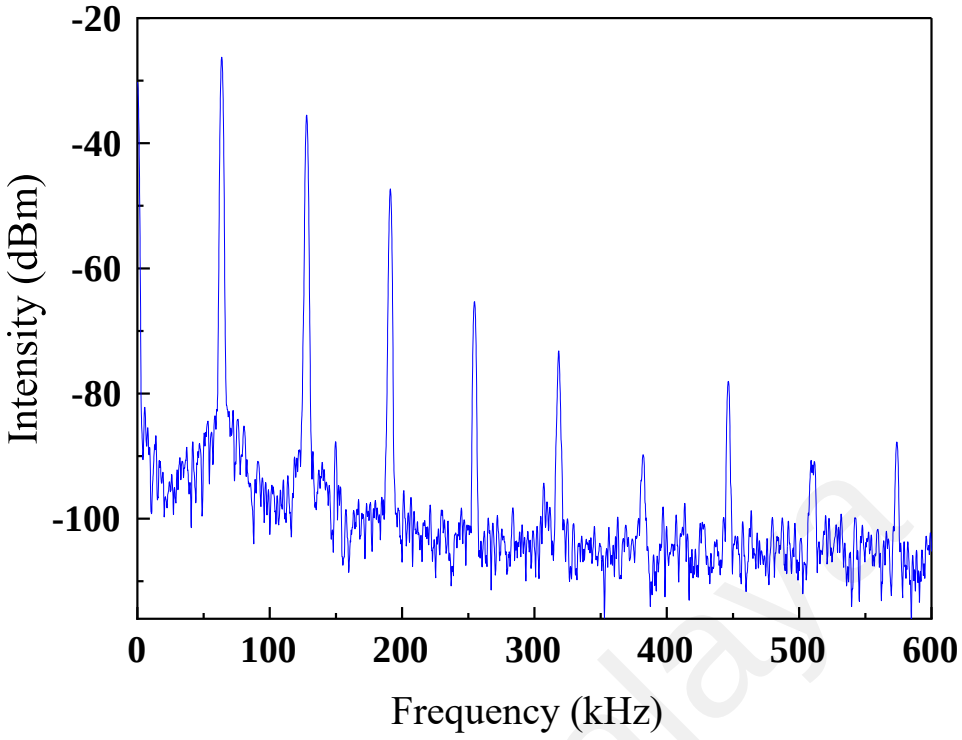

Figure 3.14: RF spectrum of Q-switching operation with MoS_2 as SA.

Figure 3.15 presents the variation of repetition rate and pulse width at different pump power. As shown, the repetition rate increased from 37.1 kHz to 62.1 kHz, while the pulse width was reduced from 6.69 μs to 3.17 μs as the pump power changed from 35.5 mW to 72.4 mW. This Q-switching operation has a lower start threshold, lower repetition rate and higher pulse width than the Q-switching with SMS structure stated in 3.2.3. Figure 3.16 shows the average output power and pulse energy of the Q-switched laser with respect to the pump power using MoS_2 as SA. Due to the lower repetition rate, the pulse energy is a bit higher than Q-switching with SMS structure.

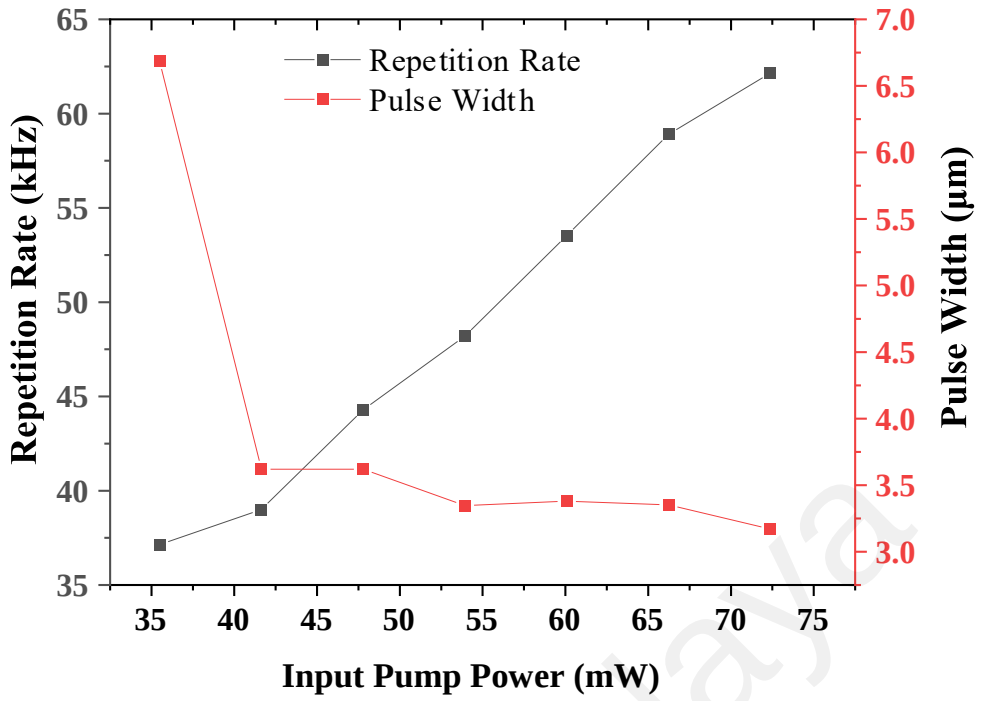

Figure 3.15: Average output power and pulse width of the Q-switched laser with respect to the pump power using MoS_2 as SA.

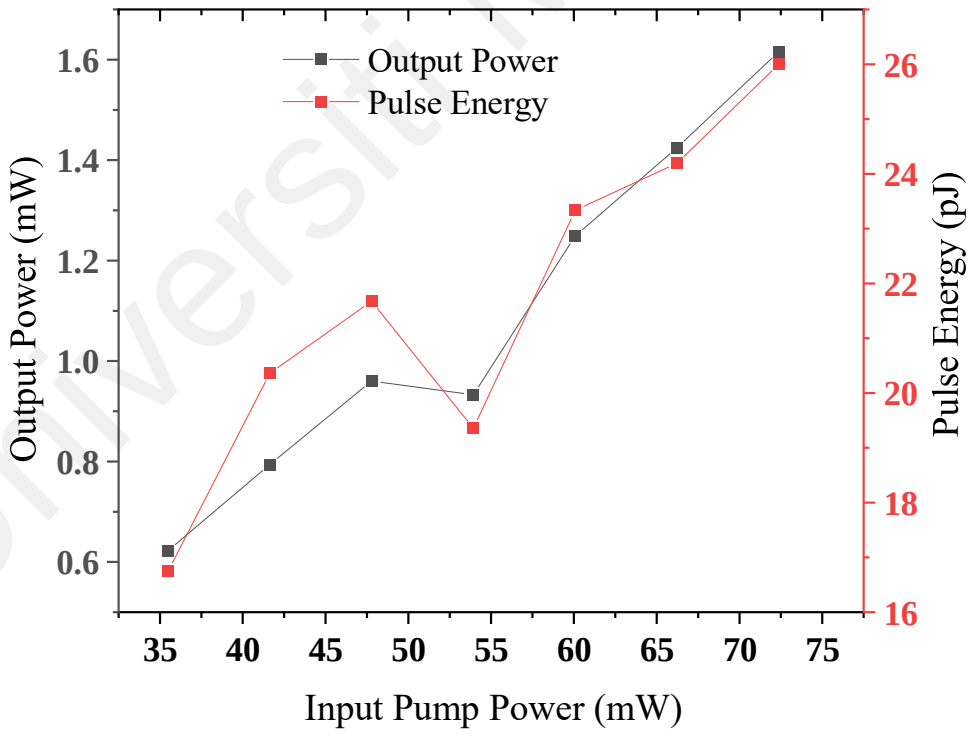

Figure 3.16: Average output power and pulse energy of the Q-switched laser with respect to the pump power using MoS_2 as SA.

In summary, a comparative analysis between the results obtained from a Q-switched laser utilizing MoS_2 as a SA was conducted, and those employing the SMS structure for

Q-switching described in subsection 3.2.3. The findings indicate that the SMS structure exhibits higher losses compared to the thin film MoS_2 SA, resulting in a higher starting threshold for Q-switched pulses and operation at different wavelengths. Furthermore, while the pulse width can reach a shorter limit with the SMS structure than with the thin film MoS_2, the stability of both experiments remains consistently above 30 dB, with the SMS structure demonstrating superior stability. Additionally, the SMS structure demonstrates the capability to withstand much higher power levels compared to the thin film MoS_2. Based on these cross-domain comparisons, it is reasonable to assert that the SMS structure offers numerous advantages over thin film SAs

3.3 Mode-locking Operation with Conventional Soliton Using GIMMF Based Artificial SA

GIMMF is another kind of MMF whose refractive index is higher at the core axis and decreases gradually towards the core-cladding interface. This refractive index profile greatly reduces the modal dispersion compared to SIMMF. Due to the multimode interference, GIMMF based SMS structures support an intensity dependent transmission that resembles real SAs. Theoretical study and experimental demonstration of GIMMF based SMS structures acting as artificial SA for mode-locking operation are extensive (Chen et al., 2020; Gan et al., 2020; Gan et al., 2021; H. Li et al., 2017; Qi et al., 2022; H. Zhang et al., 2019), showing that GIMMF based SMS structures are good candidates for mode-locking lasers. In this section, experimental demonstration of the mode-locking operation with conventional soliton using simple GIMMF based SMS structure as artificial SA shall be presented and performances shall be evaluated.

3.3.1 Mechanism of Mode-locking Operation Based on SMS structure.

In anomalous dispersion regime, when the dispersion balances the nonlinearity in the cavity, mode-locked laser with conventional soliton or bright soliton can be formed. The

Kerr effect induces nonlinear change of the refractive index, leading to the NI-MMI of the excited modes in the GIMMF. The SMS structure supports the self-imaging effect and spectral filtering effect which provide a reliable modulation to achieve nonlinear saturable absorption properties of light. Mode-locking laser operation is realized at a wavelength where the SMF-GIMMF-SMF structure performs like a saturable absorber.

It is worth noting that both Q-switching and Mode-locking using SMS structure as SA work on the mechanism of nonlinear multimode interference. If the light coupling is not ideal and the cavity experience large losses, both mode-locking and Q-switching can be achieved in the same cavity by adjusting the rotation angles of the waveplates or the polarization controller. In other words, mode-locking and Q-switching can be supported simultaneously in the fiber laser cavity with a fixed pump power. Moreover, in certain cases, the transition between Q-switching and mode-locking can be achieved by merely altering the pump power.

3.3.2 SA Preparation and Experimental Setup

The SMS structure was fabricated and characterized at first. A section of GIMMF (YOFC, OM4) was directly spliced with standard SMFs (Corning, SMF-28) on each side to form the SMF-GIMMF-SMF structure. The GIMMF was 45 mm in length with the core and cladding diameters of 50 µm and 125 µm respectively. Figure 3.17 displays the schematic diagram of the SMF-GIMMF-SMF structure.

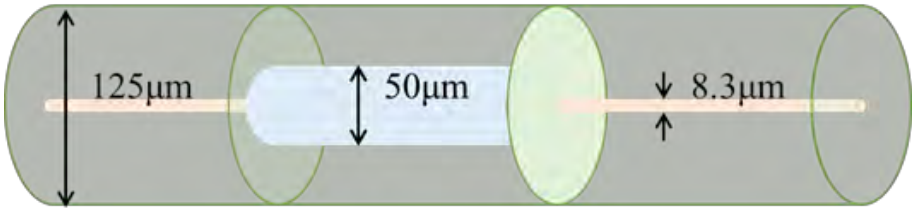

Figure 3.17: Schematic drawing of GIMMF based SMS structure.

Linear and nonlinear characterization were performed for this SMF-GIMMF-SMF structure. Figure 3.18 presents the spectral transmission characteristic of the GIMMF, which was obtained by launching a home-made ASE light source into the structure. It shows a periodic interference pattern, which was obtained due to MMI induced by several excited modes as the laser light propagates in the GIMMF. A nonlinear response function of the GIMMF based SA with peak power growth was also investigated by launching a home-made amplified ultrashort pulse into the SMF-GIMMF-SMF structure. The home-made ultrashort pulsed laser operated at a center wavelength of
1567 nm. The repetition rate and pulse width were 21.5 MHz and 700 fs respectively. Figure 3.19 shows the nonlinear characteristics of the proposed SMF-GIMMF-SMF structure. It shows a modulation depth of 4.6 %, which was higher than that of the 15.8 cm SIMMF, showing a larger change between saturated and unsaturated states. The saturable intensity of this structure was 19.33 MW/cm^2, showing a high saturation threshold. The non-saturable loss was 27.4%, much smaller than the SIMMF structure form section 3.2. This is due to the low loss of this structure.

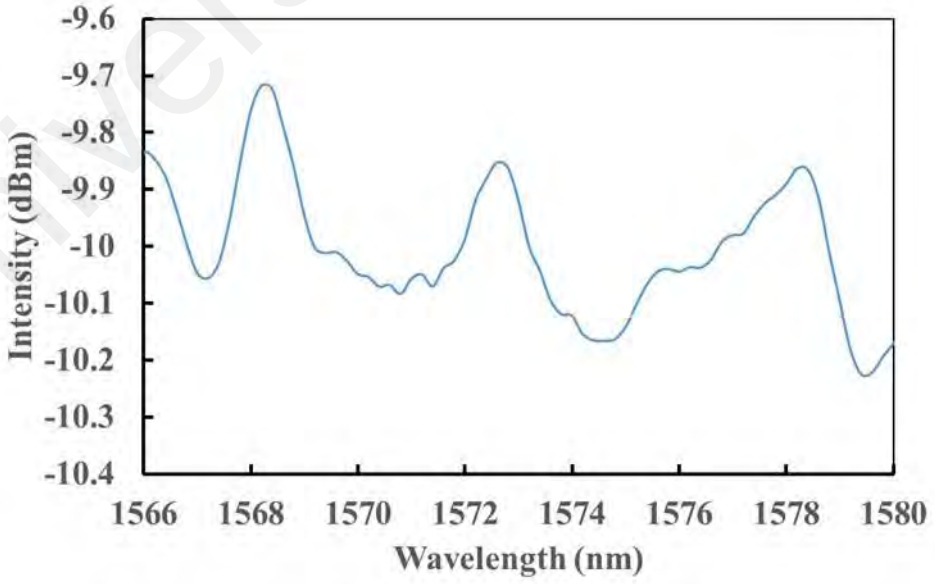

Figure 3.18: Spectral transmission of the 4.5 cm GIMMF based SA.

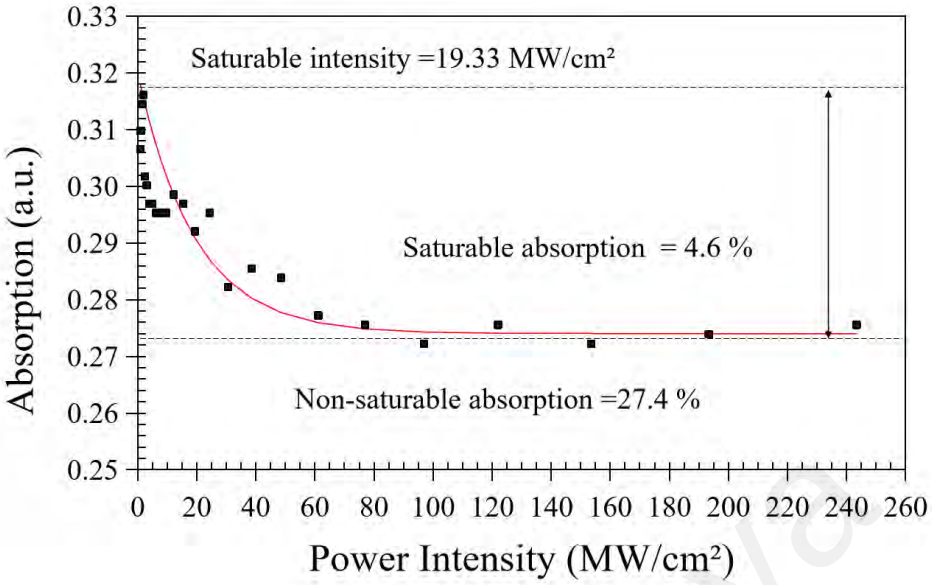

Figure 3.19: Absorption curve of the 4.5 cm GIMMF based SA.

After characterization, the SMS structure was spliced directly into a ring cavity. The schematic diagram of laser cavity is illustrated in Figure 3.20. The continuous wave laser diode (LD) provides a maximum output power of 350 mW at 975 nm (II-VI, Model LC96Z400-74). The LD is spliced with a 980/1550 nm wavelength division multiplexer (WDM). A 2 m long Erbium-doped fibre (EDF, Fibercore I25) acting as the gain medium is connected to the cavity after the WDM. The EDF has a GVD of 27.6 ps2/km and a 23 dB/m absorption rate at 980 nm. The output of gain medium is then linked to an isolator to warrant a unidirectional operation of the laser light. The prepared SMF-GIMMF-SMF structure is fusion spliced into the cavity to act as artificial SA. It consists of two types of fibers with different core diameters: 8.3/125 µm SMF and
50/125 µm GIMMF, which establish mismatched cross-sections at the splicing point. This mismatching not only produces a splicing loss but also causes mode excitation at the input end and mode coupling at the output end of GIMMF. As the light
unidirectionally oscillates in the ring cavity, the mode excitation and coupling lead to wavelength-dependent transmission. The MMI filtering effect is strongly dependent on

the effective refractive index in the fiber's core and thus it can act as an artificial saturable absorber to modulate the cavity loss for mode-locking.

An 80:20 coupler is placed after the SMF-GIMMF-SMF as feedback to the cavity and output port. The total length of the cavity is about 6.8 m which includes the gain medium, GIMMF and the single-mode fibres used in the optical components. The cavity net dispersion is calculated to be -0.05 ps^2. The polarization controller positioned before the GIMMF can slightly adjust the effective length of the multimode waveguide and thus synchronously adjust the transmission or filtering characteristic of the SMFGIMMF-SMF structure. The mode proportion of the pulse which determines the operating regime of the laser is also adjusted by the change of the effective length of GIMMF. 20% of the oscillating laser is tapped out via the optical coupler (OC) for temporal and spectral analysis using an OSA (Yokogawa, AQ6317C), an oscilloscope
(GWINSTEK GDS-3352, 350 MHz bandwidth) with a photodetector (Thorlabs: DET01CFC), a RF spectrum analyzer (Anritsu MS2683A, 7.8 GHz bandwidth) and an autocorrelator (Alnair Lab, HAC-200).

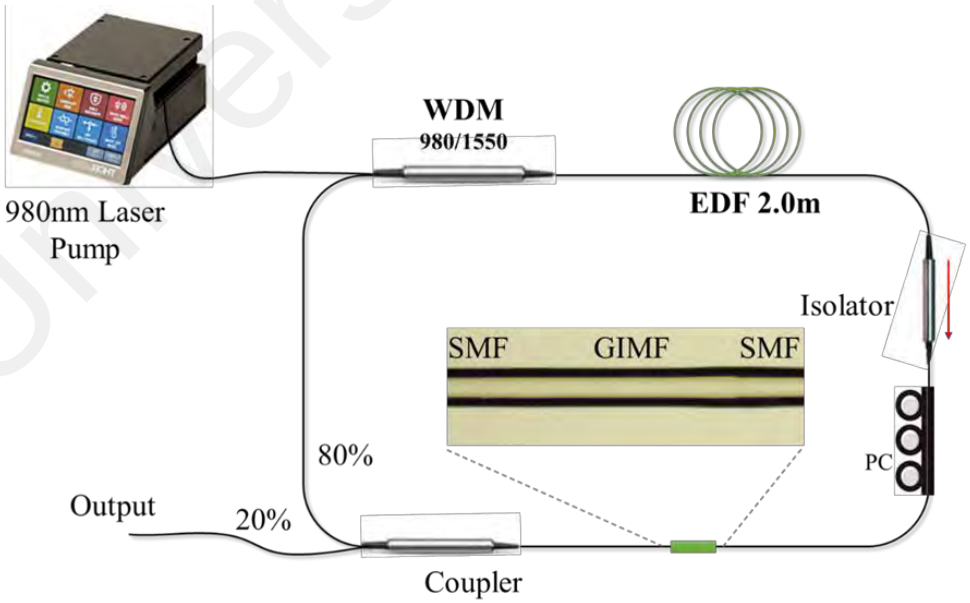

Figure 3.20: Schematic diagram of experimental setup of the ring cavity for Mode-locked pulse generation using GIMMF as artificial SA.

3.3.3 Mode-locking Performance with Conventional Soliton Using GIMMF based SMS Structure as Artificial SA

The laser cavity generated a CW laser when it was pumped with laser diode power (LDP) of 12 mW. As LDP reached 66.2 mW, it started to generate mode-locked pulses, and the mode-locking operation was maintained as the pump power was further increased up to 140.0 mW. However, the pulses on the OSC ceased to exist as the LDP is increased above 140.0 mW up to the maximum LDP of 350 mW due to the saturation effect. The laser operation reverted to CW mode, with no pulsing observed in the OSC. By decreasing the LDP to and below 140.0 mW, the reappearance of pulsing operation was observed, indicating that the damage threshold of the system exceeded this level (350 mW). Even though the damage threshold is higher than 350 mW, the SMS structure was tested several times, and it was found that with a 4.5 cm long GIMMF, mode-locked pulses always disappeared at 140~150 mW pump power range.

Figure 3.21 displays the output spectrum, which is centered at 1574 nm with a 3 dB spectral bandwidth of 9.0 nm. Several Kelly sidebands were discernible in the spectrum, indicating the generation of soliton pulses by the laser. Additionally, asymmetric sidebands were observed in the soliton spectrum, attributable to various factors including non-uniformity in the amplifier's gain profile, chirp within the soliton pulses, asymmetrical dispersion profiles, and nonlinear effects. For instance, if the gain profile is not uniform, it can amplify certain spectral components more than others, resulting in an asymmetric spectrum. The asymmetrical cavity dispersion also leads to different phase modulation of the soliton pulses at different wavelengths. Nonlinear effects such as self-phase modulation (SPM) and cross-phase modulation (XPM) can also contribute to asymmetric sidebands. These effects cause spectral broadening and can lead to asymmetries in the spectral distribution. Asymmetric sidebands can also be influenced by the dynamics of the laser cavity, such as mode-locking instabilities.

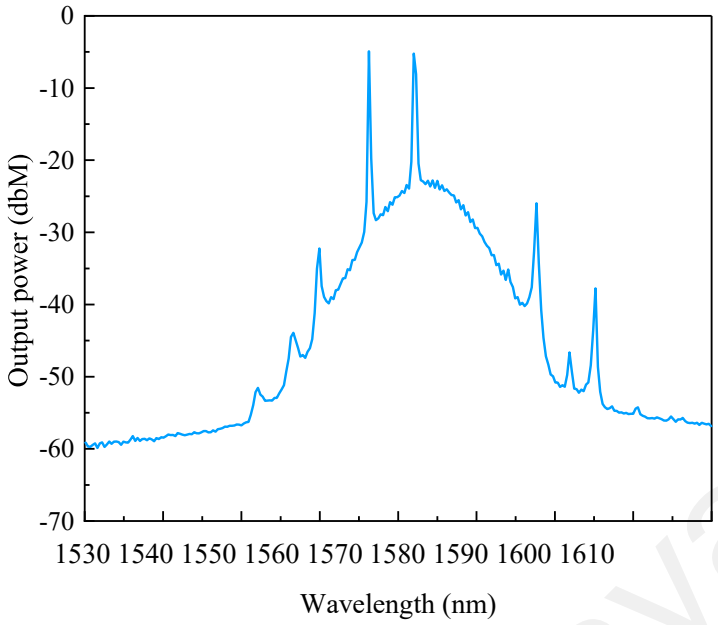

Figure 3.21: Spectrum of mode-locked laser pulse with GIMMF based structure as SA.

Figure 3.22 presents the oscilloscope trace of the mode-locked laser pulse. The pulses exhibit a uniform distribution, indicating a highly stable laser operation. The measured pulse period is 44.64 ns, which corresponds to 22 MHz repetition rate that matches with the total length of the cavity at 6.8 m.

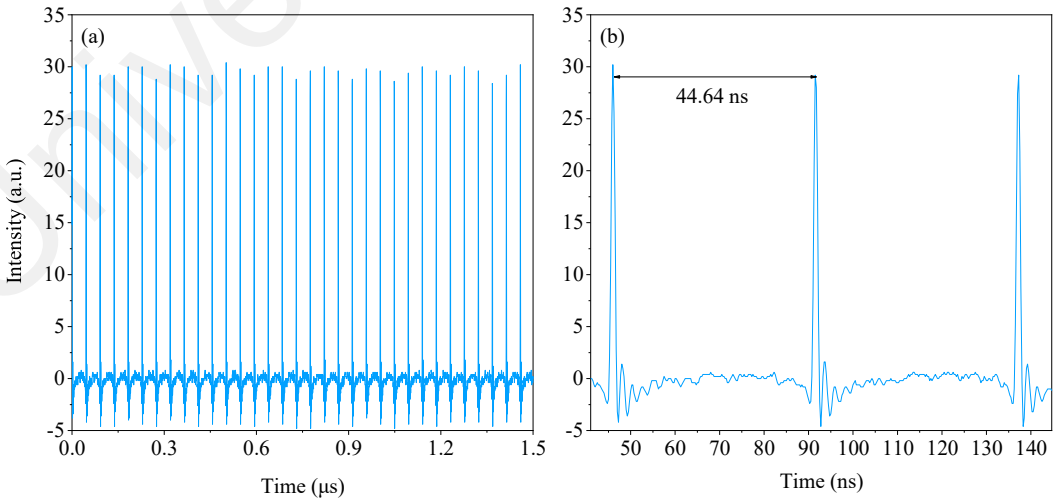

Figure 3.22: OSC trace of the mode-locked laser pulse using GIMMF based structure as SA.

The RF spectrum over a 1.0 GHz span is given in Figure 3.23 with an inset showing the enlarged RF spectrum at 22 MHz. It depicts the fundamental frequency of the pulse is at 22 MHz with a signal to noise ratio (SNR) of 43 dB. The high SNR and large number of harmonics that cover wide radio frequency spectrum up to 1.0 GHz indicate the high stability of ML operation. No other extra frequency components were found within the wide spectrum region. Figure 3.24 shows the autocorrelation trace. The autocorrelation FWHM of the ML pulse was 1.00 ps, which deconvolves to a 650-fs pulse duration assuming a sech2 pulse shape. Based on the pulse duration and 3 dB spectral bandwidth, the time bandwidth product is calculated to be 0.708 according to Equation (2.17). This indicates the ML pulses are chirped.

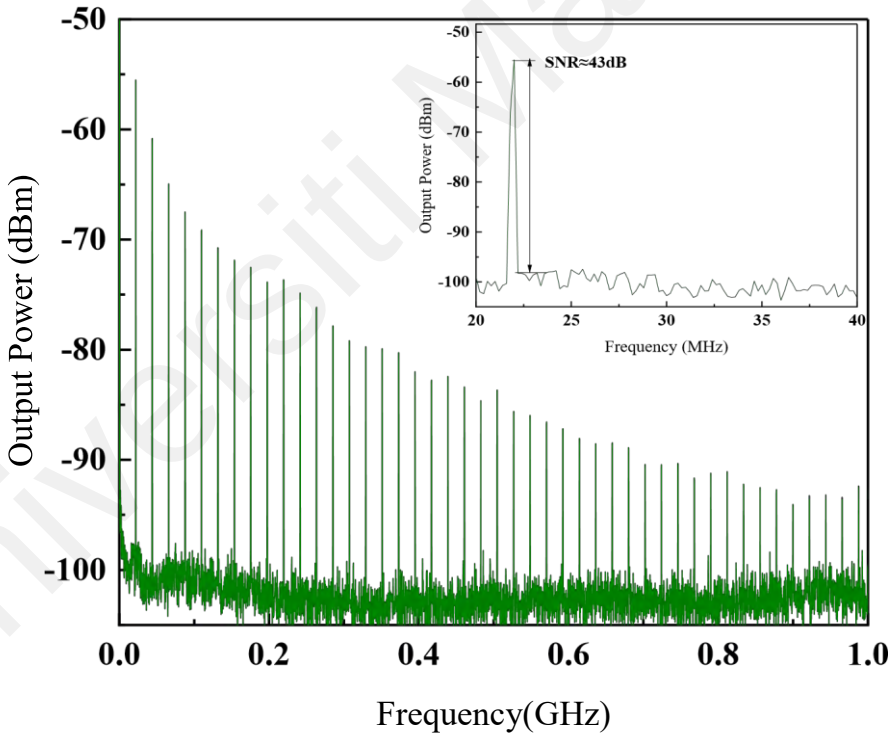

Figure 3.23: RF spectrum of the mode-locked laser pulse over 1 GHz span using GIMMF based structure as SA (inset: enlarged RF spectrum at 22 MHz).

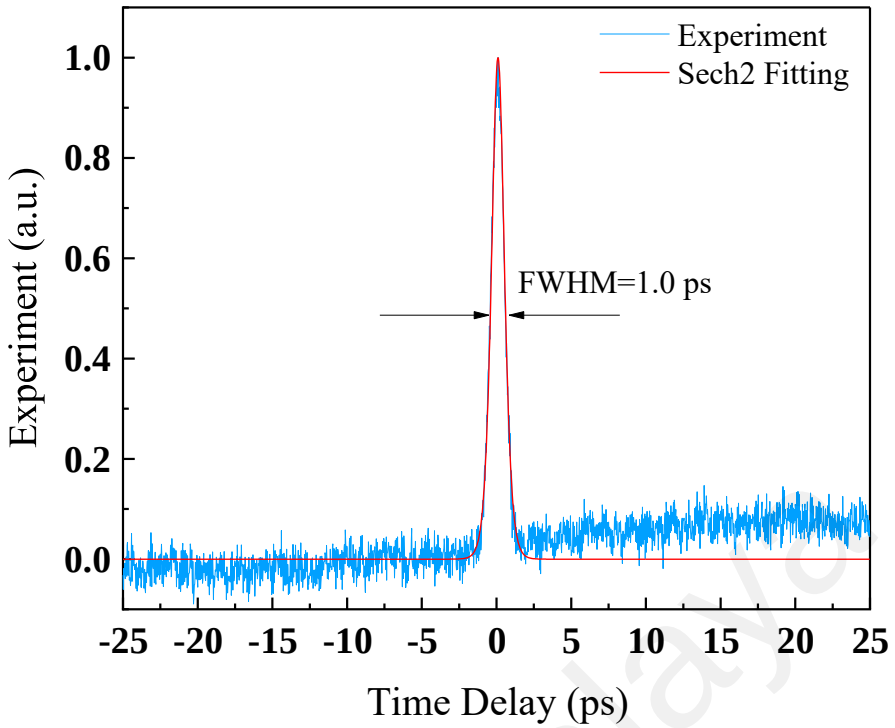

Figure 3.24: Autocorrelator trace of the mode-locked laser pulse using GIMMF based structure as SA.

When the LDP was varied from 66.2 to 140.0 mW, both the average output power and pulse energy exhibited a linear increase, rising from 3.97 to 9.82 mW and from 181 to 448 pJ, respectively, as depicted in Figure 3.25. The laser demonstrates a slope efficiency of 8.0%. However, despite surpassing the efficiency of the 15.8 cm SIMMF in Q-switching operation, this efficiency remains relatively low, indicating suboptimal conversion of pump power into laser light. This inefficiency is attributed to the relatively high cavity loss, primarily stemming from the insertion loss of the SMS structure.

To evaluate the long-term stability of the mode-locked laser, the mode-locked operation was left to run for 6 hours, and spectrum data was taken every hour. Figure 3.26 shows the spectrum result did not vary over time, indicating a good long-term stability of the mode-locked pulse.

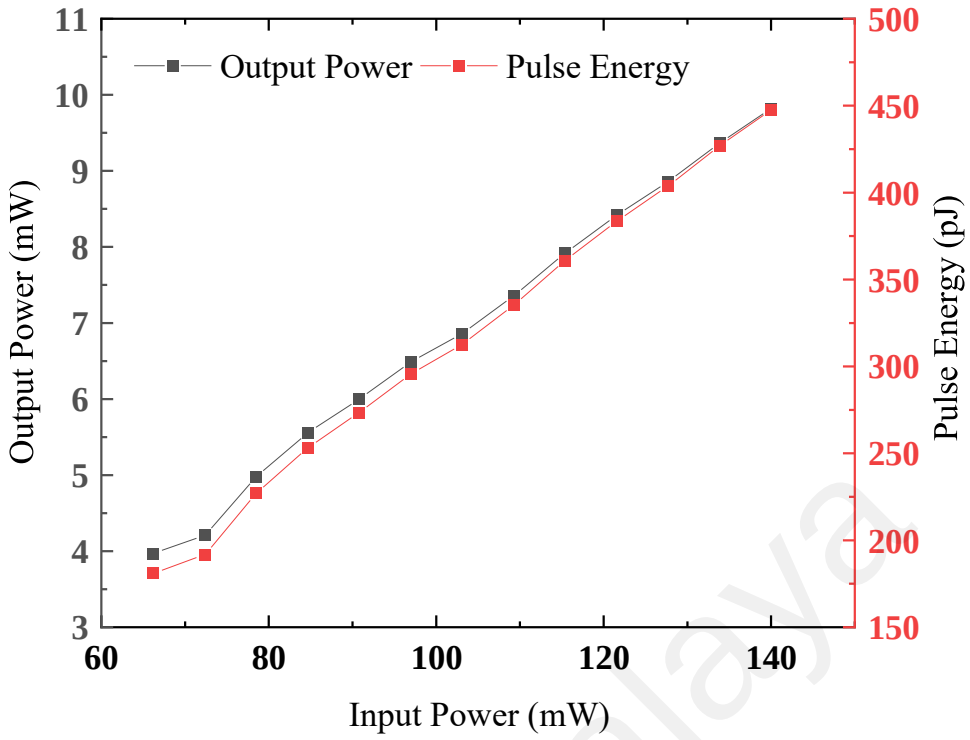

Figure 3.25: Pulse energy and output power vs LDP the mode-locked laser pulse using GIMMF based structure as SA.

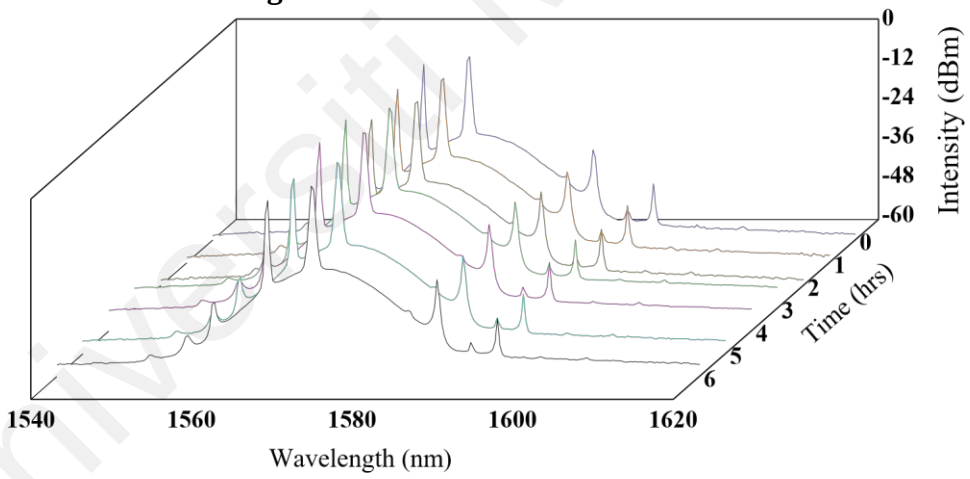

Figure 3.26: Long-term stability of the Mode-locked operation with GIMMF based structure as SA.

To summarize, this section has showcased the generation of femtosecond modelocked pulses in an EDFL employing a 4.5 cm length of GIMMF-based SMS structure as an artificial SA. Unlike Q-switched pulses, mode-locked pulses exhibit a high repetition rate of up to 22 MHz, and the round-trip time aligns well with the cavity length. While the

operation can withstand high pump power, the single pulse energy is limited to 448 pJ due to the high repetition rate. The net anomalous dispersion within the cavity supports bright solitons with Kelly sidebands; however, due to nonuniformity in cavity dispersion, nonlinearity, and gain level, the Kelly sidebands were not symmetric. Despite this, the operation demonstrates good long-term stability in a disturbance-free laboratory environment, suggesting the feasibility of employing the proposed structure in practical applications as an artificial SA. Furthermore, the proposed SMF-GIMMF-SMF structure as an artificial SA offers simplicity, low cost, and provides stable laser performance, making it an attractive candidate for modelocked pulse generation. However, it is worth noting that although the mode-locking operation exhibits good long-term stability, the proposed SMS structures were observed to be notably more sensitive to environmental changes than thin film SAs, which could pose stability challenges in real-world applications.

3.4 Harmonic Mode-locking Using GIMMF based Artificial SA

Ultrashort fiber laser with high repetition rate have been extensively investigated due to their numerous applications in precision measurement (Na et al., 2020), telecommunication (Wun et al., 2014), high-speed optical sampling (C. Li et al., 2017), biomedical treatment (C. Wang et al., 2018) and optical sensing (M. Wang et al., 2021). Typically, there are several ways to achieve a high pulse repetition rate. The direct method is by shortening the cavity length, which usually brings difficulties to the design of cavity. Secondly, active modulation is also possible to obtain high repetition rate pulses, but complex structure is involved. Harmonic mode-locking (HML) is the commonly adopted approach. It is preferable because the constraint of cavity length is no longer a limiting factor. In this section, experimental demonstration of the generation of HML pulses using

a GIMMF-based SMS structure as an artificial SA in an EDFL operating in the anomalous dispersion regime shall be conducted and performance shall be evaluated.

3.4.1 Mechanism of HML Operation Based on SMS structure.

The generation of harmonic bright pulses can be illustrated by several steps. First, the cavity was set in anomalous dispersion regime, which supports the formation of bright pulses. With a suitable PC state, additional group delay can be introduced from the principal modes in the GIMMF to further support bright pulses. Second, the GIMMFbased SMS structure allows high intensity light to pass and block low intensity light for mode-locking. The pulse shaping by nonlinear effect occurs in fiber laser, and the peak of a pulse increases per round trip, leading to the growth of efficient gain. Because of the pulse shaping, the bandwidth of pulse increases. But the time-domain narrowing is limited by gain medium and cavity dispersion. Thus, the pulse splits into two pulses to extract a maximal amount of gain. A chaotic process exists before the generation of stable two bright pulses, in which the gain gradually reaches a stable value. Finally, the repulsive force, resulting from interactions of pulses by radiation wave in cavity drives the pulses to move away from each other, resulting in uniform pulse distribution throughout the cavity. As a multiple pulse state, harmonic mode-locking needs enough pumping strength and stabilizing mechanisms to support its existence.

3.4.2 Experimental Arrangements

A section of GIMMF (YOFC, OM4) was directly spliced with standard SMFs (Corning, SMF-28) on each side to develop the SMF-GIMMF-SMF structure. Except the length of the GIMMF is changed to 10.3 cm, rest is the same as in section 3.3. The schematic drawing of the SMS structure refers to Figure 3.17.

Linear and nonlinear characterization were performed for this SMF-GIMMF-SMF structure. Figure 3.27 presents the spectral transmission characteristic of the GIMMF,

which was obtained by launching a home-made ASE light source into the structure. It shows a periodic interference pattern due to MMI induced by several excited modes as the laser light propagates in the GIMMF. A nonlinear response function of the GIMMF based SA with peak power growth was also investigated by launching a home-made amplified ultrashort pulse into the SMF-GIMMF-SMF structure. The home-made ultrashort pulsed laser operated at a center wavelength of 1567 nm. The repetition rate and pulse width were 21.5 MHz and 700 fs respectively. Figure 3.28 shows the nonlinear characteristics of the proposed SMF-GIMMF-SMF structure. It shows a modulation depth of 7.6 %, which was higher than that of the 15.8 cm SIMMF indicating a better modulation capability. The saturable intensity of this structure was 86 MW/cm^2, showing a high saturation threshold. The non-saturable loss was 22.5%, much smaller than the SIMMF structure form section 3.2. This is due to the low loss of this structure.

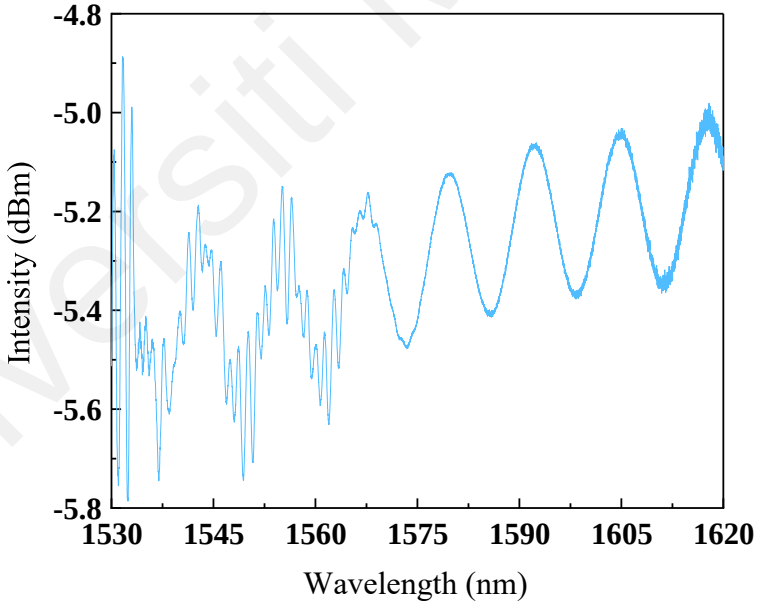

Figure 3.27: Spectral transmission of the 10.3 cm GIMMF based SA.

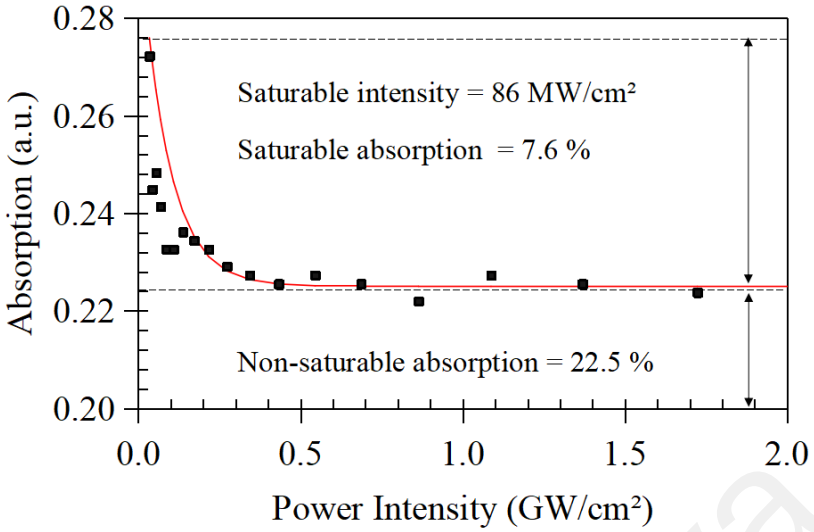

Figure 3.28: Absorption curve of the 10.3 cm GIMMF based SA.

The cavity settings for harmonics of conventional soliton are similar to that of the mode-locked pulse with conventional soliton generation. Except that the length of the GIMMF is 10.3 cm instead of 4.5 cm. Thus, the readers can refer to Figure 3.20 for the cavity settings.

3.4.3 HML Performance Using SMF-GIMMF-SMF as Artificial SA

The laser cavity produced a CW laser when the pump power remained below 47.8 mW. Upon increasing the pump power to 47.8 mW, and through proper adjustment of the polarization controller (PC), the initiation of the 2nd harmonic mode-locking (HML) occurred. This 2nd HML state persisted until further increasing the pump power to 164.6 mW, at which point the appearance of the 3rd harmonic was observed. Subsequently, the 4th harmonic emerged as the pump power reached 176.9 mW. However, noticeable instability ensued with a further increase in power, culminating in the disappearance of pulses at 183.1 mW. Upon decreasing the pump power without adjusting the PC, no HML was observed. In another series of mode-locking operation experiments using a 10.3 cm GIMMF-based SA, it was found that the proposed SMS structure exhibited a damage

threshold well exceeding 350 mW. Consequently, the inability to recover HML by power reduction suggests that once the conducive environment for HML formation is disrupted, it cannot be reinstated.

In Figure 3.29, the output spectrum during the 2nd harmonic mode-locking is depicted. The spectrum is centered at 1567 nm, exhibiting a narrow 3 dB spectral bandwidth of 1.2 nm. Notably, the absence of Kelly sidebands in the spectrum suggests that the mode-locked laser generated a stretched pulse. Figure 3.30 and Figure 3.31 present the oscilloscope trace of the 2nd and 3rd HML. The pulses exhibit a uniform distribution, indicating the HML is a highly stable operation. The measured pulse period decreases from 22.9 ns to 15.7 ns when changing from the 2nd HML to the 3rd HML, which aligns well with the cavity length. The pulse width increased from 2.13 ns to 3.26 ns. This might be because of the measurement problem due to the limited resolution of the devices. The 4th HML with a repetition rate of 87.1 MHz was also observed. The period and pulse width were 11.5 ns and 2.29 ns. This result shows good alignment with the 2nd HML. Even though the period of the 4th HML reduced to half of the 2nd HML period, the pulse width remained somewhat close to the 2nd HML.

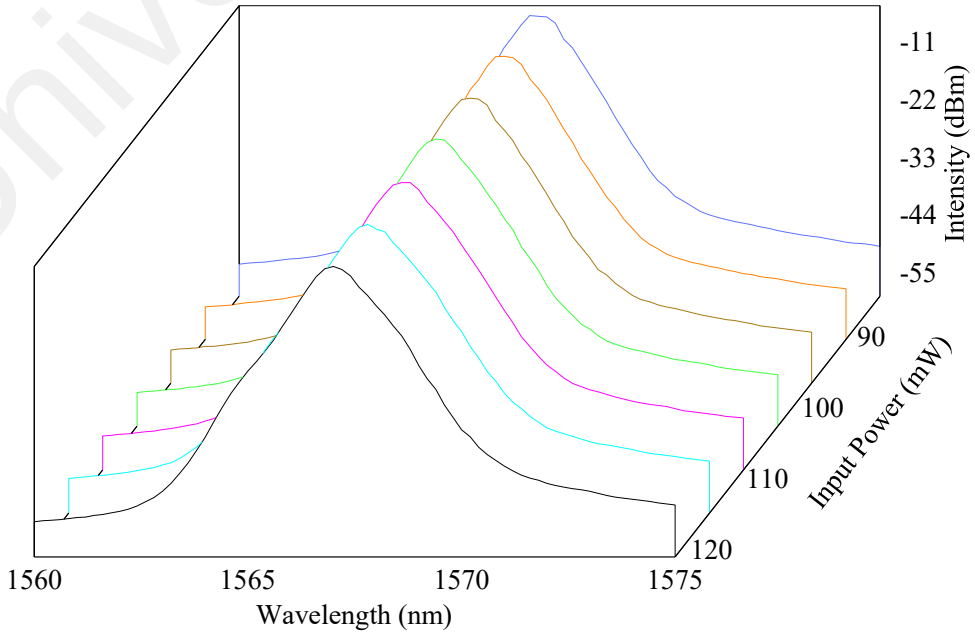

Figure 3.29: Spectrum of HML with GIMMF based structure as SA.

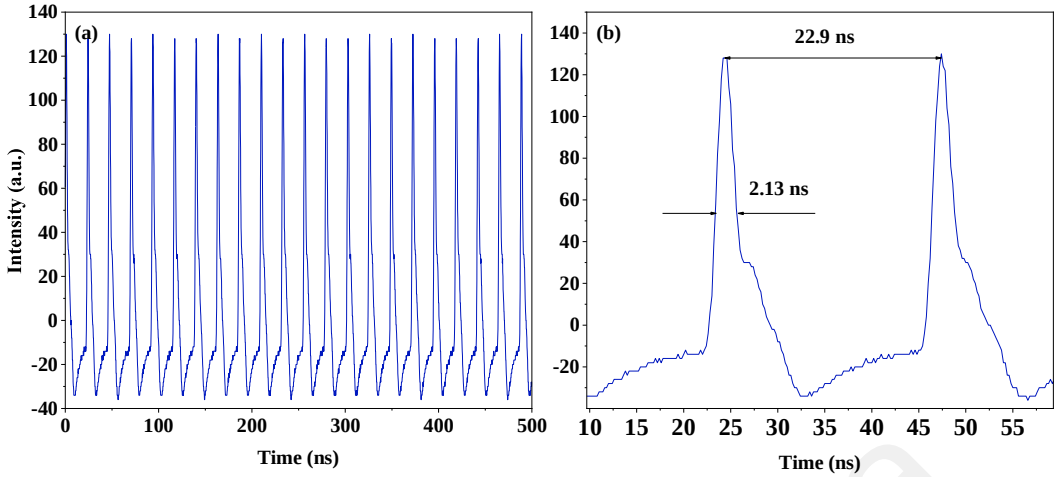

Figure 3.30: Pulse Train of the 2nd HML using GIMMF based structure as SA.

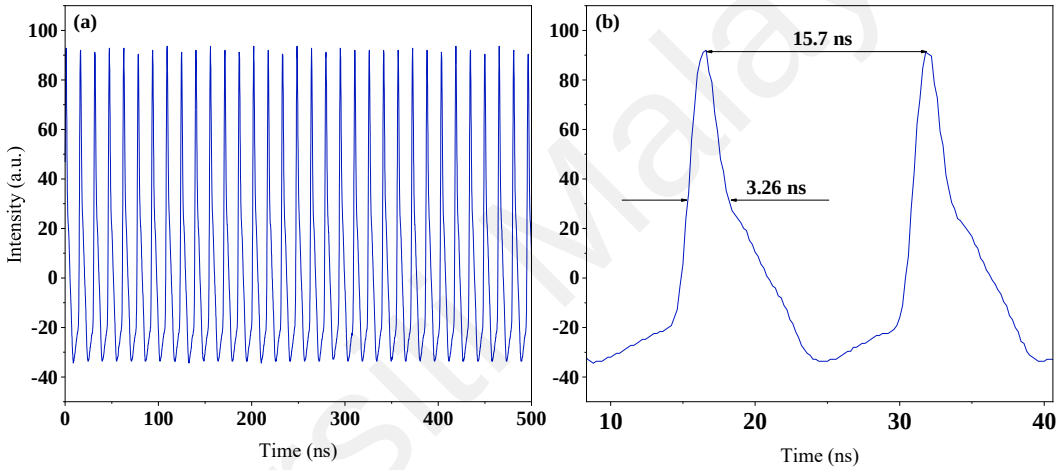

Figure 3.31: Pulse Train of the 3rd HML using GIMMF based structure as SA.

Figure 3.32 (a) and (b) display the RF spectrum over a 500 MHz span for the 2nd HML and 3rd HML, respectively. Given the length of the laser cavity, the fundamental repetition rate is approximately 21.6 MHz. However, the repetition rates observed in Figure 3.32 (a) and (b) are approximately 43.4 MHz and 63.7 MHz, indicating the presence of pulses in the 2nd HML and 3rd HML regimes. The SNRs for the 2nd HML and 3rd HML are measured at 34 dB and 31 dB, respectively. The high SNRs and the presence of numerous harmonics covering a wide RF spectrum of over 500 MHz indicate the remarkable stability of the

HML operation. Notably, no additional frequency components were identified within this broad-spectrum region.

The autocorrelation trace of the 2nd HML is shown in Figure 3.33. The autocorrelation FWHM of the 2nd HML pulse was 1.02 ps. Assuming the pulse is a $sech^2$ pulse shape, the pulse FWHM is about 650 fs. Due to the HML is highly sensitive to environment perturbation, the autocorrelation FWHM was not obtained for the 3rd and 4th HML during the experiment. However, according to the pulse clamping effect (Gene et al., 2023), it is likely that the pulse widths of the 3rd and 4th HML are very similar to the 2nd HML.

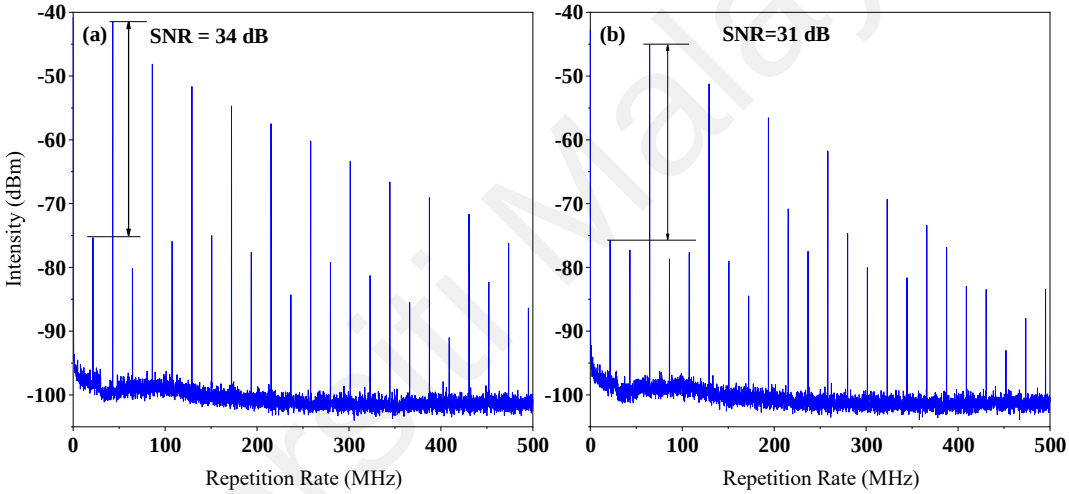

Figure 3.32: RF spectrum of (a) 2nd HML and (b) 3rd HML over 500 MHz span using GIMMF based structure as SA.

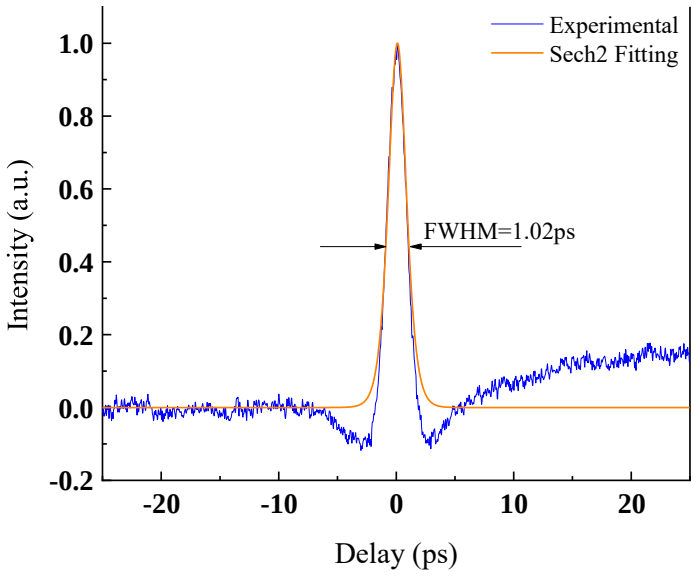

Figure 3.33: Autocorrelator trace of 2nd HML using GIMMF based structure as artificial SA.

When the pump power ranged from 84.7 to 183.1 mW, the average output power exhibited a linear increase from 6.78 to 16.04 mW. In the 2nd HML, the pulse energy rose from 156 to 359 pJ. However, at the 3rd and 4th HML, the pulse energy decreased due to the higher repetition rate. The relationship between output power, pulse energy, and input pump power is illustrated in Figure 3.34. The laser demonstrates a slope efficiency of 9.8%, surpassing that of the 4.5 cm GIMMF-based SA mode-locking operation. One potential explanation for this higher slope efficiency is that the length of the GIMMF is closer to the exact self-imaging point, resulting in improved transmission quality.

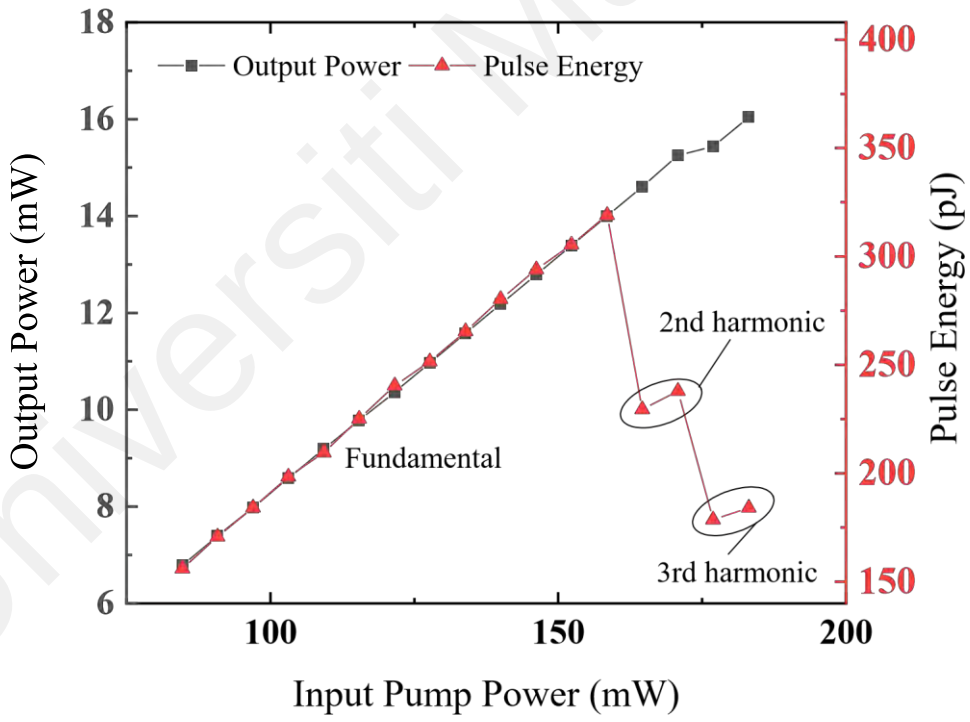

Figure 3.34: Pulse energy and output power vs input pump power of the HML using GIMMF based structure as SA.

In conclusion, HML in an EDFL in anomalous dispersion regime with the SMFGIMMF-SMF structure as SA was demonstrated in this section. A 10.3 cm long

GIMMF was used to form the SMS structure. This SMS structure has an even higher damage threshold than the 4.5 cm long GIMMF based SMS structure. The spectrum bandwidth was small compared with fundamental mode-locking with the 4.5 cm GIMMF based SMS structure as artificial SA. The repetition rate aligned well with the cavity length for each HML. In the meantime, the HML showed high stability with the SNR more than 50 dB. However, chaotic was obvious when the pump power was high enough for the HML to change to a higher HML, which made it very difficult to record higher HML. The input-output power showed a very good linear relationship and a slope efficiency of 9.8% were obtained, which was higher than the 4.5 cm long GIMMF based SMS structure fundamental mode-locking operation. With almost the same cavity settings, the different slope efficiency showed the HML has higher converting efficiency of the electrical power to laser.

3.5 Discussion

This chapter presents the experimental demonstration of short and ultrashort pulsed laser generation in the anomalous dispersion regime using SMS structures as artificial SAs in an EDFL. Q-switched pulses, conventional soliton mode-locking, and harmonic mode-locking pulses were observed using three different SMS structures with similar cavity settings.

Linear characterization results of all three SMS structures revealed periodic interference patterns indicative of MMI within the MMFs. Nonlinear characterization showed that the SMF-SIMMF-SMF based SMS structure had low modulation depth, low saturation intensity, and high non-saturable losses, rendering it unsuitable for modelocking. In contrast, GIMMF-based structures exhibited higher modulation depth, saturation intensity, and lower non-saturable losses, attributed to differences in core diameter and refractive index profile between the two MMFs. Longer GIMMF segments

increased the damage threshold without significantly affecting losses, enabling larger saturation intensity and modulation depth.

The proposed SMF-SIMMF-SMF structure for Q-switching exhibited a unique spectral profile with multiple lower peaks in the 1.5 μm range due to MMI. Although stable, it was sensitive to environmental perturbations, and its large core diameter introduced significant losses, resulting in low slope efficiency and operation wavelength at 1530 nm. Repetition rate increased from 87.4 kHz to 157.7 kHz with pump power increasing from 115.4 mW to 343 mW, while pulse width decreased from 4.2 μs to 2.4 μs, typical of Q-switching. Comparisons with MoS_2 as SA for Q-switching highlighted the advantages of SMS structures in terms of stability, ease of fabrication, low cost, and high damage threshold.

Mode-locking with conventional soliton and HML using SMF-GIMMF-SMF structures demonstrated good input-output linearity and stability. HML effectively increased repetition rate without shortening cavity length, with harmonics operating at a center wavelength of 1567 nm and repetition rates of 43 MHz and 64.6 MHz for the 2^{nd} and 3^{rd} harmonics, respectively. However, HML exhibited high chaos at higher pump powers, making pulse recovery challenging compared to mode-locking with conventional soliton.

3.6 Summary

This chapter experimentally demonstrated Q-switching, mode-locking with conventional soliton, and harmonic mode-locking in the anomalous dispersion regime. Mechanisms of pulse formation were studied, and experimental results with analysis were presented. The objective of evaluating SMS structure as artificial SA to generate Q-switched pulse, conventional soliton pulse and HML pulse is accomplished.

CHAPTER 4: UNCONVENTIONAL SOLITONS IN EDFL USING SMS STRUCTURE AS ARTIFICIAL SA

4.1 Introduction

Solitons, characterized by their localized wave packets capable of propagating long distances without distortion, have captured the interest of researchers due to their particle-like stability during transmission, making them valuable in telecommunications and other applications. In addition to conventional bright solitons discussed in Chapter 3, various other optical solitons have been observed experimentally, including dissipative solitons, soliton molecules (bound states), soliton rain, multiple pulsing, and noise-like pulses. Understanding the dynamics of these solitons is crucial given their potential practical applications.

Bound solitons, a form of multi-pulsing, while slightly less stable than conventional solitons, exhibit relatively good stability and are increasingly garnering attention as demand grows for higher data transmission speeds. Shannon's law dictates that data transmission rates are bounded by channel capacity, prompting the exploration of new coding formats. Unlike conventional solitons, bound solitons have the potential to encode more than just binary information (Stratmann et al., 2005).

In the normal dispersion regime, multi-pulsing manifests in various forms such as noise-like pulses (NLP) and dissipative soliton resonance (DSR). NLP, less stable than bound state solitons, is identifiable by its extremely wide bandwidth and a center peak with a large base in the autocorrelator trace. DSR, on the other hand, is characterized by its rectangular pulse shape. Harmonic mode-locking (HML) represents another form of multi-pulsing, wherein the power reaches a certain level, leading to evenly distributed multi-pulsing.

This chapter is structured as follows: Section 4.2 presents the experimental demonstration of bound state solitons using the proposed SMS structure, along with methods for identifying tightly and loosely bound solitons and the mechanisms behind bound state soliton formation. In section 4.3, the formation mechanism of multi-pulsing is discussed, with an experimental demonstration of ultra-broadband dissipative solitons featuring multiple pulsing at low input power. Section 4.4 explores the harmonics of dissipative solitons in an Erbium-doped fiber laser (EDFL). Finally, section 4.5 provides a summary of the chapter's findings and section 4.6 concludes this chapter.

4.2 Bound Soliton in Anomalous Dispersion Regime

Bound solitons are formed when multiple solitons attract each other due to the nonlinear interaction. Bound solitons using SMS structure as SA were experimentally observed in both anomalous dispersion regime (Gan et al., 2020; Zhu et al., 2019) and normal dispersion regime (Lv et al., 2019; Wang et al., 2019). However, bound solitons in anomalous dispersion tend to have larger pulse durations and broader spectra compared to solitons in the normal dispersion regime. Besides, unlike bound solitons in normal dispersion regime, these solitons can be either in-phase or out-of-phase, depending on their relative positions and phases.

Bound soliton could be recognized by its autocorrelator trace and by its spectrum. There is more than one peaks in the autocorrelator trace, and the spectrum shows specific characteristics depending on the phase difference of the two bounded solitons. This section focuses on bound soliton formation using GIMMF based SMS structure as artificial SA in anomalous dispersion regime.

4.2.1 Mechanism of Bound Soliton Operation

Optical solitons represent unique pulse formations within mode-locked fiber lasers, occurring when a delicate balance is struck between gain, loss, dispersion, and

nonlinearity. However, this equilibrium can be disrupted by adjustments to the polarization controller or an increase in pump power, leading to the phenomenon known as peak-power limiting effect, where a single pulse splits into multiple pulses with reduced peak energy. These pulses interact with each other through both repulsive and attractive forces.

When these individual pulses become bound together due to these forces, maintaining constant time separations and fixed phase differences, they give rise to bound solitons or higher-order solitons. Bound solitons are categorized into tightly bound solitons and loosely bound solitons, depending on the strength of their interaction. Tightly bound solitons, also referred to as soliton molecules, exhibit tightly and steadily fixed time separations and spectrum modulation periods. Conversely, loosely bound solitons feature relatively less stringent time separations and unstable spectrum modulation periods.

Distinctive features of bound solitons include modulation periods on the optical spectrum and symmetrical multiple peaks on autocorrelation traces. The intensity of these peaks indirectly reflects the intensity ratio of the solitons within a bound soliton configuration. Researchers have established a fundamental relationship between the spectrum modulation period and time separation of the peaks on autocorrelation traces, articulated in the following equation:

$$\Delta T = \frac{\lambda_0^2}{c \cdot \Delta\lambda} \tag{4.1}$$

where $\Delta\lambda$ represents the spectrum modulation period, ΔT denotes the time separation, c signifies the speed of light in a vacuum, and λ_0 corresponds to the center wavelength.

4.2.2 Experimental Approach

The SMS structure was initially constructed by fusion splicing a 45 mm length of GIMMF (50/125 core diameter) in between the SMF coming from the isolator and the SMF from the input port of the coupler using a fusion splicer (Fujikura 90S+). The losses

at both splicing points were measured approximately 0.01 dB. To avoid bending the GIMMF, which may cause a change of birefringence, the SMS structure was put in an in-line PC. The schematic diagram in Figure 4.2 illustrates the SMS structure and the locations of the splicing points. Notably, the standard SMF-28 has a core/cladding dimension of 8.2/125 µm, while the GIMMF features a larger core/cladding dimension of 50/125 µm. When light propagates from the SMF to the GIMMF, a multimode interference phenomenon occurs due to the significant difference in core diameter between the two fibers at the splicing point. This mismatched cross-section leads to mode excitation and coupling at the splicing points.

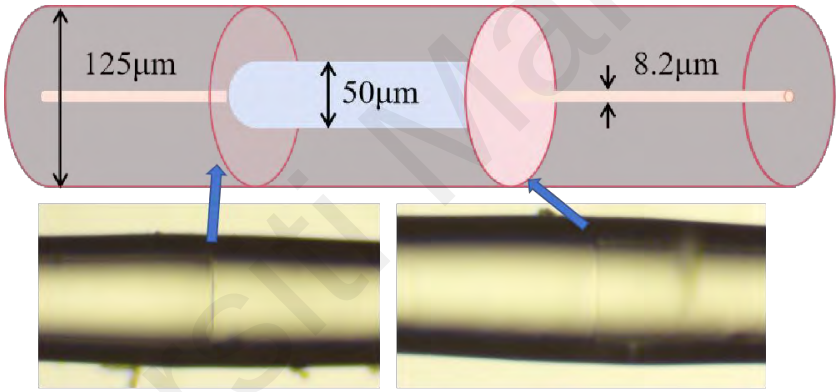

Figure 4.1: Schematic diagram of the SMS structure with the image of splicing point at both ends of GIMMF.

Figure 4.2 depicts the spectral transmission characteristic of the SMS structure, revealing a periodic interference pattern. This pattern emerges due to multimode interference induced by the excitation of several modes as the laser light propagates through the GIMMF. To assess the modulation depth and saturation intensity of the SMS structure, a balanced twin-detector system was employed. A custom-built modelocked fiber laser with a center wavelength of 1567 nm, pulse width of 700 fs, and a repetition rate of 21.73 MHz served as the laser source. The nonlinear transmission curve was fitted with Equation (2.16) and the experimental results are depicted in Figure 4.3, revealing

that the saturable absorption, saturable intensity and non-saturable absorption are 4.6 %, 19.33 MW/cm^2, and 27.4 % respectively. These findings indicate that the absorption properties of the SMS structure undergo changes with the incident light intensity. At low intensities, the device permits high transmission, but as the intensity rises, absorption saturates, resulting in reduced transmission. This characteristic can be used to modulate laser's cavity loss for mode-locking.

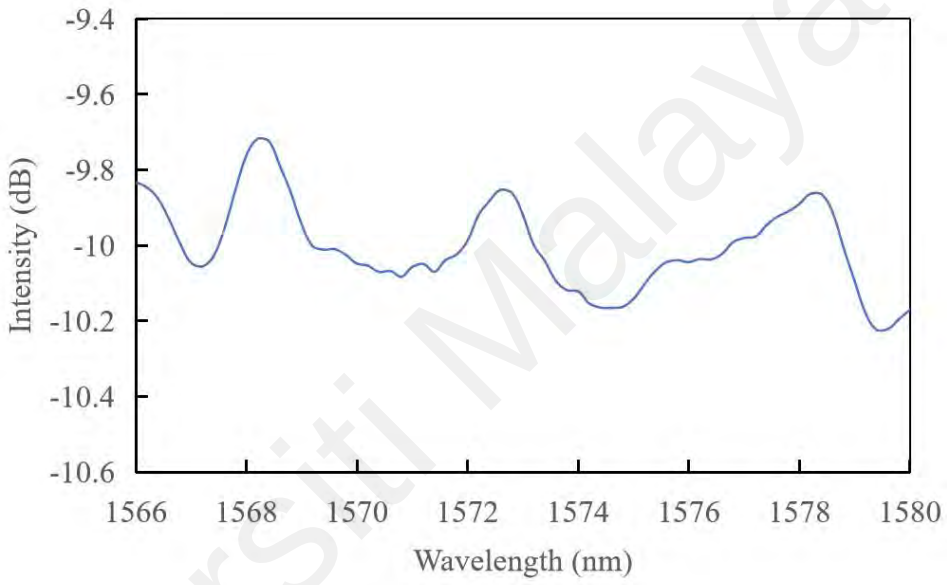

Figure 4.2: Spectral transmission characteristic of the SMS structure.

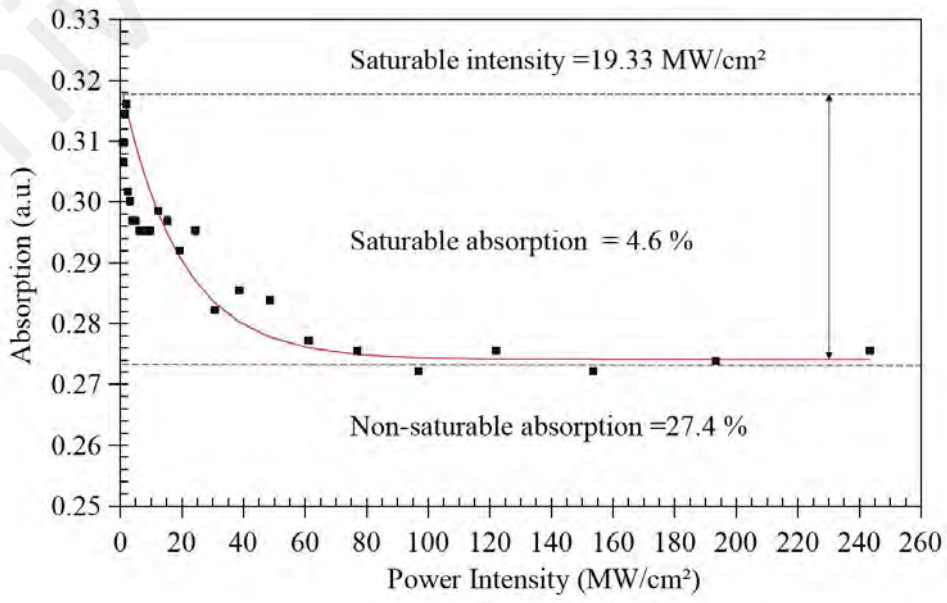

Figure 4.3: Nonlinear transmission curve of the SMS structure-based SA.

Figure 4.4 shows the schematic diagram of the proposed mode-locked fiber laser, which is based on a ring cavity. It employed a laser diode (II-VI, LC96Z400-74 980 module) with a center wavelength of 974 nm and a maximum output power of 350 mW as a pump source. The pump light was launched into a 2 m long Erbium-doped fiber (EDF) (I25 Fibercore), which functions as a gain medium through a 980/1550 nm wavelength division multiplexing (WDM) coupler. The output port of EDF was spliced to an isolator to limit the back-reflection in the ring cavity and ensure unidirectional propagation of the oscillating laser. The output port of the isolator was spliced to a three peddle polarization controller (PC), which was connected to the SMF-GIMMF-SMF structure. The PC was used to adjust the polarization for laser mode locking. To avoid bending the GIMMF, which may cause the change of self-imaging length, the SMS structure was put inside an in-line PC. The output from the PC was spliced to the input port of the output coupler (OC) with 80:20 output ratio. 80% port of the OC was connected to the input port of the WDM. 20 % port of the OC was used to monitor the performance of the mode locked EDFL. An optical spectrum analyzer (OSA) (Anritsu, MS9710C) with a resolution of 0.02 nm and a high-speed photodetector (EOT, InGaAs PIN Detector, ET-3500F) attached to digital oscilloscope (GW Instek, GDS-3352) were used to characterize the laser performance in wavelength and time domain, respectively. An optical power meter (Thorlabs, PM100D) with optical sensor (Thorlabs, S145C) and RF spectrum Analyzer (Anritsu, MS2830A) were used to measure average output power of the system and the stability of the pulse repetition rate, respectively. The total length of the cavity was about 9.35 m including the gain medium. The dispersion parameter of the Erbium-doped fiber (EDF) and the SMF were -17.3 $ps/(km \cdot nm)$ and 17 $ps/(km \cdot nm)$ respectively, resulting the net dispersion of the cavity to be -0.12 ps^2.

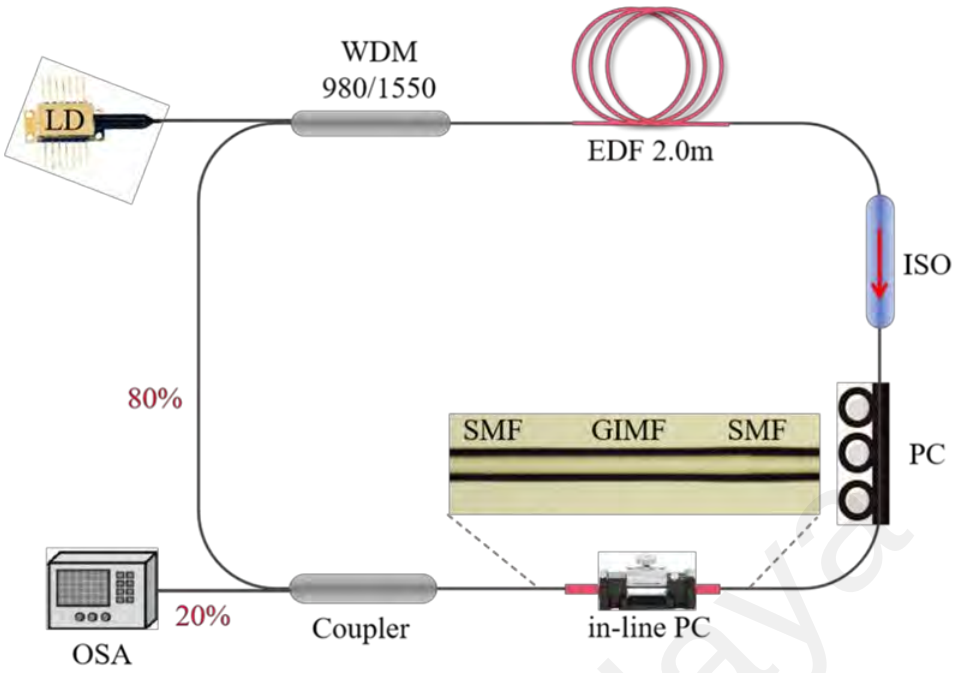

Figure 4.4: Schematic diagram of the mode-locked fiber laser

4.2.3 Bound Soliton in Anomalous Dispersion Regime Performance

As discussed earlier, the unidirectional oscillation of light within the ring cavity, resulting from mode excitation and coupling at the intersection of SMF and GIMMF, introduces wavelength-dependent transmission. The degree of this multimode interference is heavily dependent on the effective refractive index within the fiber's core. The Kerr Effect, influencing the refractive index of the optical fiber with changing light intensity, facilitates high transmission at elevated power intensity and low transmission at lower intensity. This behavior closely resembles that of a SA. In this scenario, the SMS structure is utilized as an artificial SA to modulate cavity loss for mode-locking. However, the SMS structure demonstrates sensitivity to the length of the GIMMF. To address this, an in-line polarization controller (PC) was introduced into the cavity to alleviate the GIMMF length limitation. This was achieved by straightening the GIMMF and applying pressure on the GIMMF to alter its birefringence.

There are two ways to produce pulse splitting with constant pump power and cavity length. One is to decrease the modulation depth of the SA and the other is to increase

cavity dispersion. Decreasing the modulation depth of the SA is used in this research. Based on this idea, the modulation depths of SMF-GIMMF-SMF structure with different lengths of GIMMF were tested. The shorter lengths of GIMMF results in lower modulation depths. Taking the result that shorter length of GIMMF also can withstand lower pump power into consideration, the 45 mm GIMMF-based SMS structure was chosen for this research.

With proper adjustment of the PC, a stable mode-locked laser became observable on the oscilloscope at the pump power 29.3 mW. The performance of the mode-locked laser is summarized in Figure 4.5. Figure 4.5(a) depicts a representative optical spectrum of the mode-locked pulses, showing a conventional soliton spectrum with Kelly sidebands. Operating at a center wavelength of around 1573 nm, it exhibited a 3 dB spectral bandwidth of 7.83 nm. Figure 4.5(b) presents the oscilloscope trace of the mode-locked pulse train, displaying a relatively uniform intensity with a pulse period of 44.34 ns, corresponding to the round-trip time within the cavity. The corresponding radio frequency spectrum of the generated pulse train is shown in Figure 4.5(c), revealing a robust signal peak at the cavity's fundamental repetition rate of 21.98 MHz, corresponding to a laser cavity length of 9.35 m. The signal-to-noise ratio (SNR), reached 68 dB, indicating highly stable mode-locking operation. The inset is the 1-GHzspan RF spectrum, which suggests that the fiber laser effectively operates in a continuous mode-locking state. Following a Sech ^{2}curve fitting, the autocorrelation trace in Figure 4.5(d) indicates a full-width half-maximum (FWHM) of 650 fs. Consequently, the time-bandwidth product (TBP) was calculated to be 0.615, surpassing the transform limit of 0.315, suggesting that this pulse is up chirped.

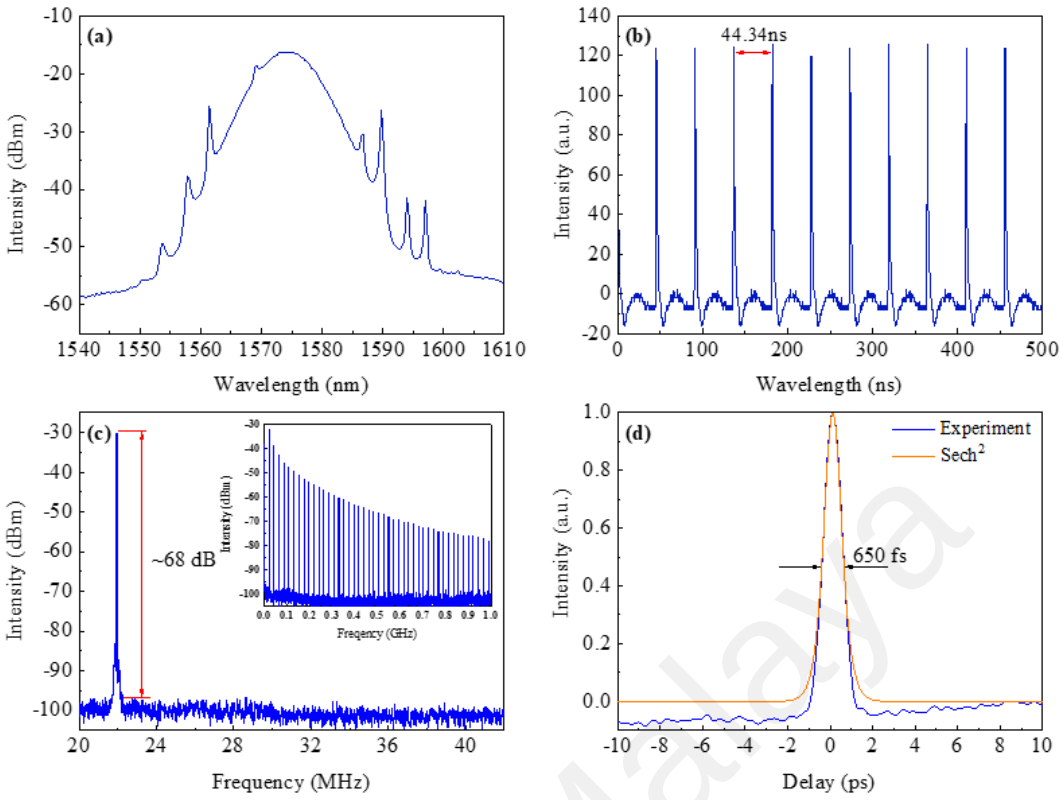

Figure 4.5: Conventional soliton performances (a) Optical spectrum; (b) pulse train; (c) RF spectrum (inset: the RF spectrum within a larger range of 1 GHz); (d) autocorrelation trace.

To evaluate the long-term stability of the conventional soliton, the optical spectrum every one hour for 6 hours was recorded at a fixed pump power of 47.8 mW. The recorded spectra maintained well over time as shown in Figure 4.6.

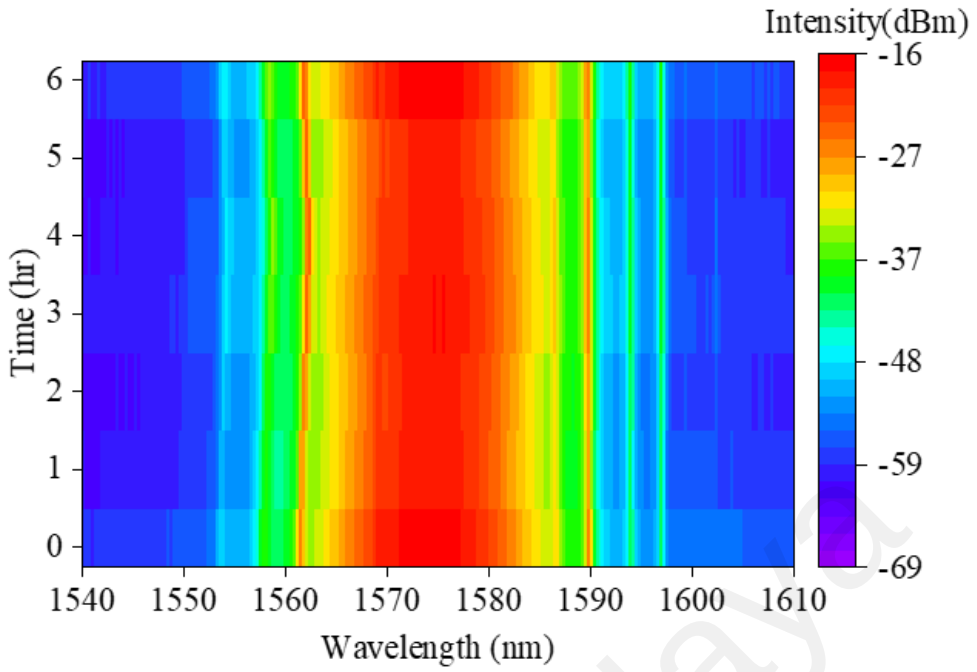

Figure 4.6: Long term stability test of the conventional soliton (Every 1 hour for 6 hours)

After the observation of conventional soliton at the highest pump power it can withstand, which was 158.5mW, the pump power was decreased to 54mW. By proper adjustment of the PC, simultaneously existing tightly and loosely bound soliton were observed. In Figure 4.7(a), the optical spectrum is presented alongside an enlarged section highlighting a regular modulation with a period of approximately 0.6 nm. The center wavelength is around 1570 nm and the FWHM is about 10 nm. Figure 4.7(b) shows the typical pulse train at pump power of 54 mW. It indicates a pulse interval of 45.54 ns, corresponding to the repetition rate of 21.98 MHz. Due to the limitation of the oscilloscope, it is not possible to zoom in to see the pulse splitting, which could be seen indirectly with the autocorrelation trace instead.

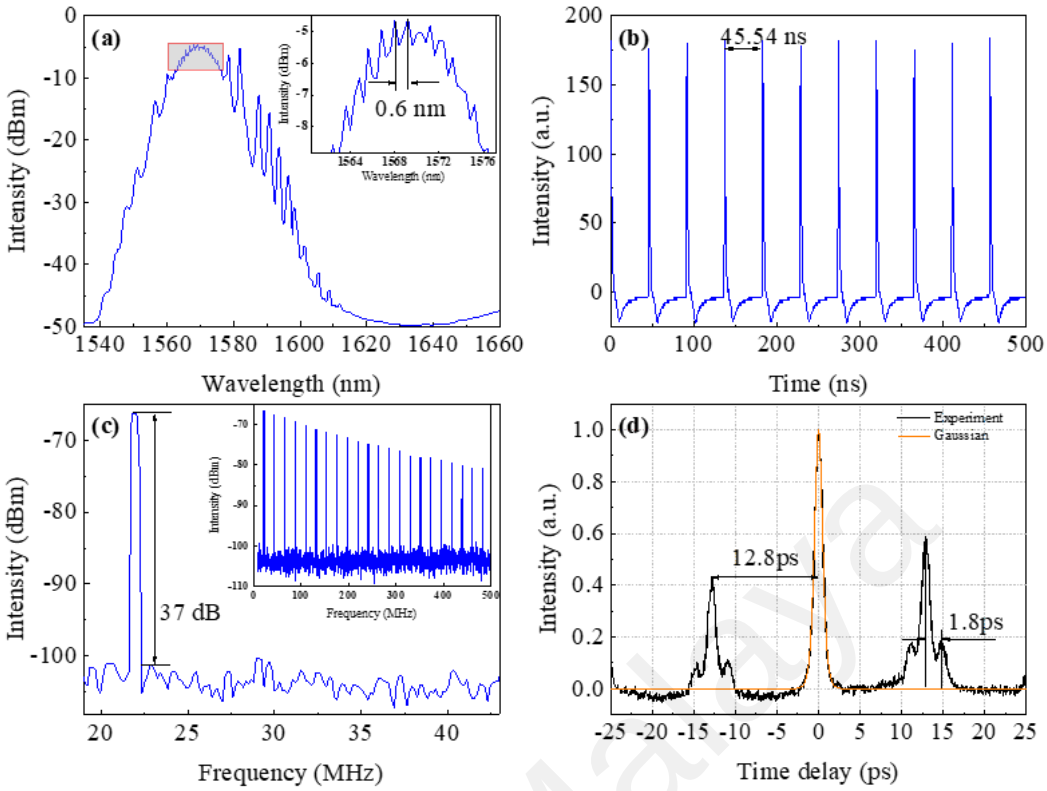

Figure 4.7: Bound soliton performances (a) Optical spectrum; (b) pulse train; (c) RF spectrum (inset: the RF spectrum within a range of 500 MHz); (d) autocorrelation trace.

In Figure 4.7(c), the corresponding RF spectrum is presented, revealing numerous harmonics within a 500 MHz frequency range. An SNR of 37 dB is observed at the fundamental frequency of 21.98 MHz. Figure 4.7(d) shows the autocorrelation trace. Due to the measurement issue, a slight asymmetry appears on the figure. The three higher peaks with an approximately 1:2:1 intensity ratio, demonstrates that the two solitons comprising the bound-state pulse exhibit nearly identical intensities. The time separation is about 12.8 ps, approximately 17.3 times of the pulse width of 740 fs, indicating the two solitons are loosely bound. The two side peaks have two even lower peaks around them. This is because one of the solitons in the loosely bound state soliton is also a bound state soliton. The time separation of this bound state soliton is 1.8 ps, about 2.4 times of the pulse width, indicating the two solitons are tightly bound. The remarkably short time

separation between the two solitons in the bound soliton suggests that their direct interaction arises from attractive or repulsive forces exerted on each soliton. The intensity ratio of the tightly bound soliton is around 1:3:1, which is likely because the intensity of the two solitons is different.

Due to the instability of the higher order soliton, by increasing the input pump power, the side peaks around the two higher side peaks disappeared. This is likely because the phase relationship between the two solitons is loosened, and the soliton is no longer bound to the side soliton. After the disappearance of the side peaks, only three peaks were left on the autocorrelation trace. Figure 4.8 (a)-(c) show the autocorrelation trace. The time separations keep at 20.4 ps while the intensity ratio of the peaks increases beyond 1:2:1 at the beginning, which indicates that the intensity of the two solitons is no longer the same and the difference between them becomes larger. With time passing by and the increase of the pump power, the intensity ratio of the peaks on the autocorrelation trace becomes greater. This is likely because the reflectivity was changed in the cavity due to the increasing pump power which caused the change of the intensity of the solitons in the bound soliton. Figure 4.8 (d)-(f) show optical spectrum. The modulation depth on the spectrum decreases with the increase of the intensity ratio of the peaks, which aligns well with the theoretical analysis. The modulation period on the spectrum remained almost the same at 0.4 nm, together with the center wavelength of 1570 nm and the time separation of 20.4 nm, it is obvious that the observed phenomenon has a good alignment with Equation (4.1).

Another interesting phenomenon is that, with the same cavity settings and the same 45 mm SA, the conventional soliton disappears at around 140mW for all of our testing, while the pump power can reach up to 250.7 mW for bound soliton operation.

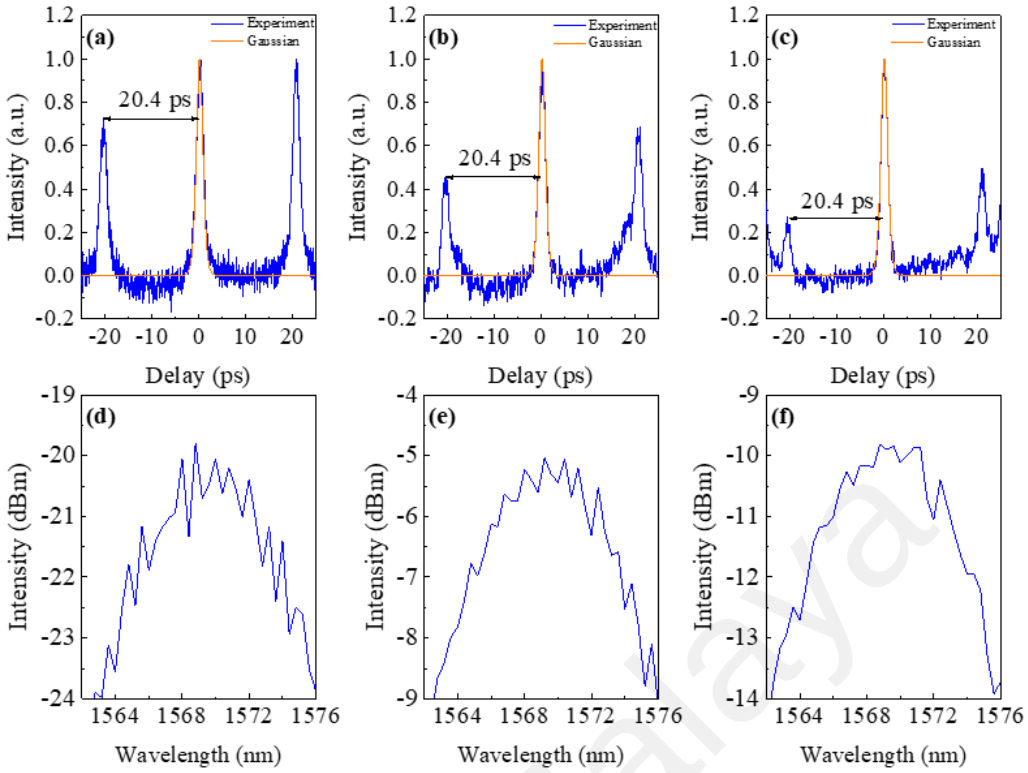

Figure 4.8: Bound soliton characteristics at different pump power levels (a)-(c) Autocorrelator trace. (d)-(f) Optical spectrums.

In conclusion, both conventional and bound solitons in mode-locked fiber laser were demonstrated using SMF-GIMMF-SMF structure as artificial SA. The conventional soliton was observed with good long-term stability while the bound soliton transformed from a simultaneously existing tightly and loosely bound soliton to a loosely soliton with the increase of the pump power. Besides, with the change of the pump power, loosely bound soliton with constant time separation but with varying peak ratios on the autocorrelation trace was also observed. The result in this section confirms the possibility of generating different kinds of solitons with SMF-GIMMF-SMF structure as artificial SA. It also helps to better understand the dynamics of transformation of bound solitons.

4.3 Ultra-broadband Dissipative Soliton with Multi-Pulses

Multi-pulsing is a prevalent phenomenon observed in passive mode-locking fiber lasers, holding significance for its ability to deliver higher pulse energy (Michalska et al., 2022). In both anomalous and normal dispersion regimes, multi-pulsing occurs when the

pump power surpasses a threshold value (Haboucha et al., 2008; Komarov et al., 2005). Recently, several instances of multi-pulsing in mode-locked fiber lasers utilizing SMS structures as artificial SA have been reported, particularly with noise-like pulses (T. Chen et al., 2021; Sobon et al., 2016; Xu et al., 2024; Yang et al., 2024) and dissipative soliton resonance (Lyu et al., 2017). These studies have highlighted the necessity of relatively high-power levels, typically in the range of several hundred milliwatts, to initiate multi-pulsing.

This section demonstrates the generation of multi-pulses within a bunch envelope from a mode-locked EDFL configured with a ring cavity. Dissipative soliton formation entails a complex interplay of dispersion, nonlinearity, gain, and loss, giving rise to stable, localized structures within the laser cavity. Effects such as self-phase modulation (SPM), cross-phase modulation (XPM), and four-wave mixing (FWM) contribute to spectral broadening and the generation of broadband dissipative solitons. As the pump power increases, the pulses within a dissipative soliton inevitably undergo multi-pulsing due to wave-breaking in nonlinear optical fibers.

4.3.1 Cavity Design

The SMS structure used in this experiment is the same with section 3.4.2, which is based on a 10.3 cm long GIMMF. Thus, the linear and nonlinear characterization of the SMS structure can be found in Figure 3.27 and Figure 3.28 respectively. Figure 4.9 shows the schematic drawing of the mode-locked EDFL cavity with dispersion management using SMF-GIMMF-SMF as SA. All the components are the same as in 4.2.2, expect that a 230 m long dispersion compensation fiber (DCF) was added into the cavity after the SMS structure. The dispersion of the DCF is -4 $ps/(km \cdot nm)$. The total cavity length was estimated at 239.5 m. The calculated dispersion in the cavity was ~1.07 ps^2, suggesting that the cavity operated in the net normal dispersion regime.

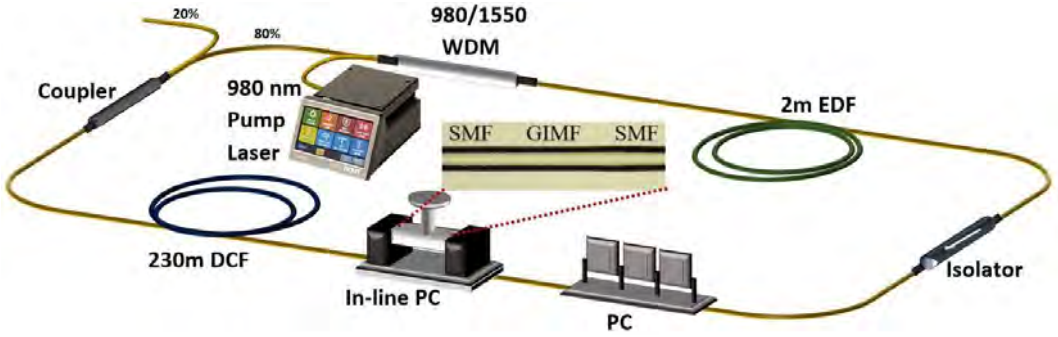

Figure 4.9: Schematic diagram of mode-locked EDFL cavity with dispersion management using SMF-GIMMF-SMF as SA.

4.3.2 Ultra-broadband Dissipative Soliton Performance

As the pump power gradually increased to 23.2 mW, and with careful adjustment of the PC, spectral broadening was observed in the OSA. The difference in core diameter between the MMF and SMF facilitated multimode interference, enabling the coupling of high-power signals and effectively simulating the characteristics of an artificial SA. The low threshold power required to initiate pulsing was attributed to the optimal length of the GIMMF and the low-loss cavity.

Figure 4.10 illustrates the pulsing spectrum observed in the OSA as the pump power changed. The spectrum exhibited broadening, spanning wavelengths from 1540 nm to 1630 nm, with a center wavelength of 1570 nm. Remarkably, the center wavelength remained stable at 1570 nm throughout the increment of pump power, ranging from 23.2 mW to 220 mW, with an approximate 6 mW interval.

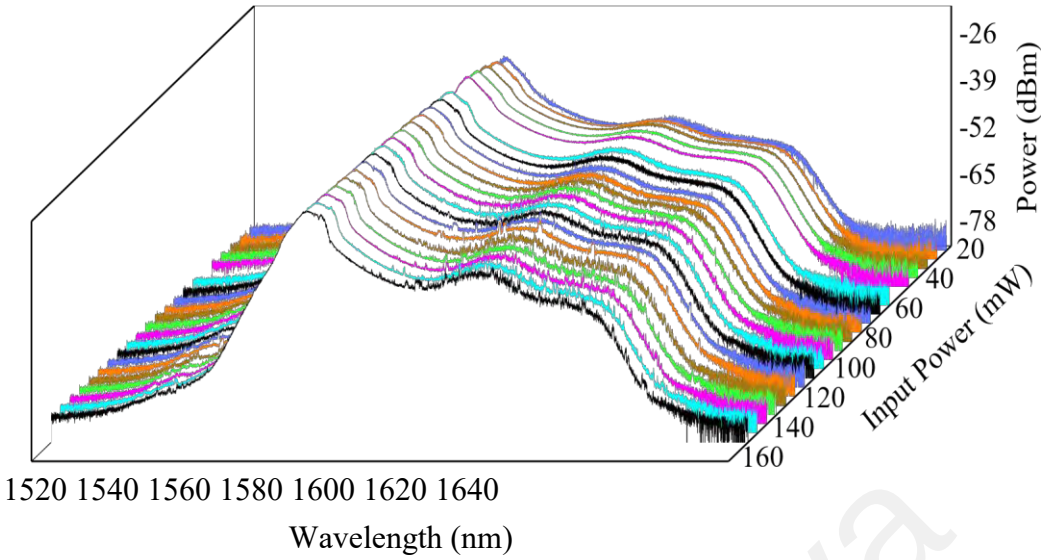

Figure 4.10: Evolution of optical spectrum with the increment of pump powers.

Figure 4.11 illustrates the temporal characteristics of the laser at four different pump powers. Unlike the conventional single pulse circulating in a cavity, it was observed that pulses were grouped within a rectangular-shaped envelope, with the number of pulses within the envelope increasing progressively with the increment of pump power. Consequently, as the number of pulses increased, the size of the bunch envelope also grew.

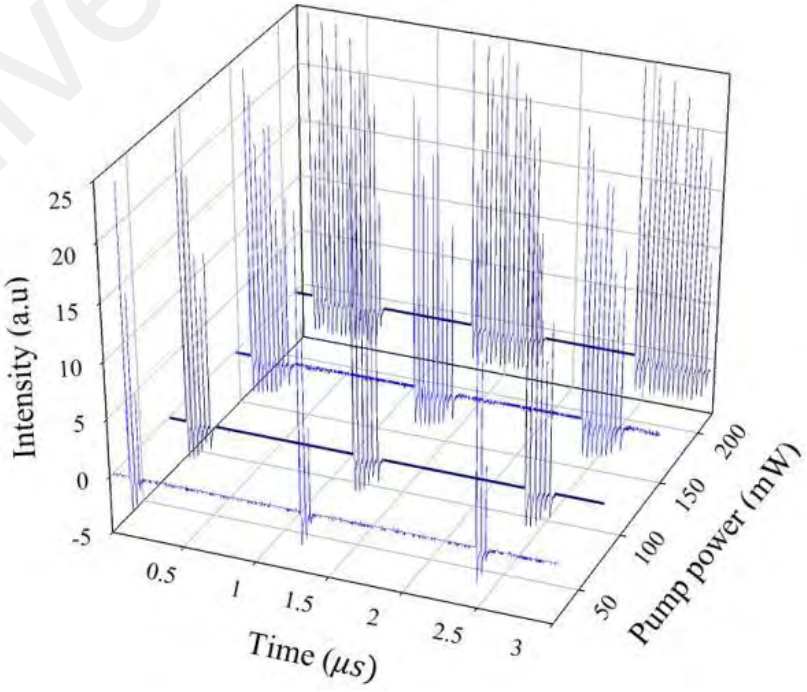

Figure 4.11: Evolution of bunch envelope with pump power.

Figure 4.12 shows the relationship between the number of pulses in a bunch envelope with pump power. The emitting number of pulses grew from three pulses (pump power 23.2 mW) to sixteen pulses (pump power 220 mW). The number of pulses was maintained at sixteen at the maximum available pump power of 220 mW. Figure 4.13 (a) and (b) depict the zoom in view of bunch envelopes at 23.3 mW and 220 mW pump power respectively. The spacing between bunch envelopes was measured at 1175 ns and this translated to repetition rate 850.8 kHz. This revealed that the pulse was circulating at its fundamental frequency, and this corresponded with the total cavity length. On the other hand, the spacing between pulses in an envelope was evenly spaced at 33.5 ns for all pump powers. Even though the peak intensity of pulses was nonuniformly distributed, its peak was kept at 25 a.u with the increment of pump power. The phenomenon of multi-pulse bunching was attributed to the high nonlinear effect, triggering pulse bunching. NL-MMI can exacerbate mode competition. When pump power was increased beyond its threshold, accumulation of nonlinear phase shift from mode-competition was more pronounced in the laser cavity which eventually led to pulse bunching. The pulse bunches were further investigated by decreasing the pump power. The formation of muti-pulse bunch corresponds to the capability of identical pulses to self-organize into bunch envelope with duration shorter than the round-trip time of cavity. The number of pulses reduced, and this confirmed the attainment of pulse bunches in the cavity.

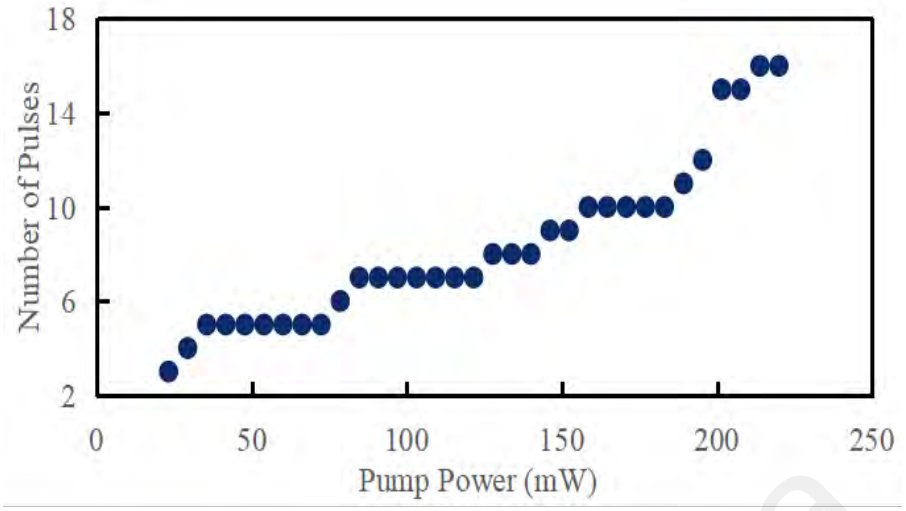

Figure 4.12: Projection of number of pulses in an envelope with pump power.

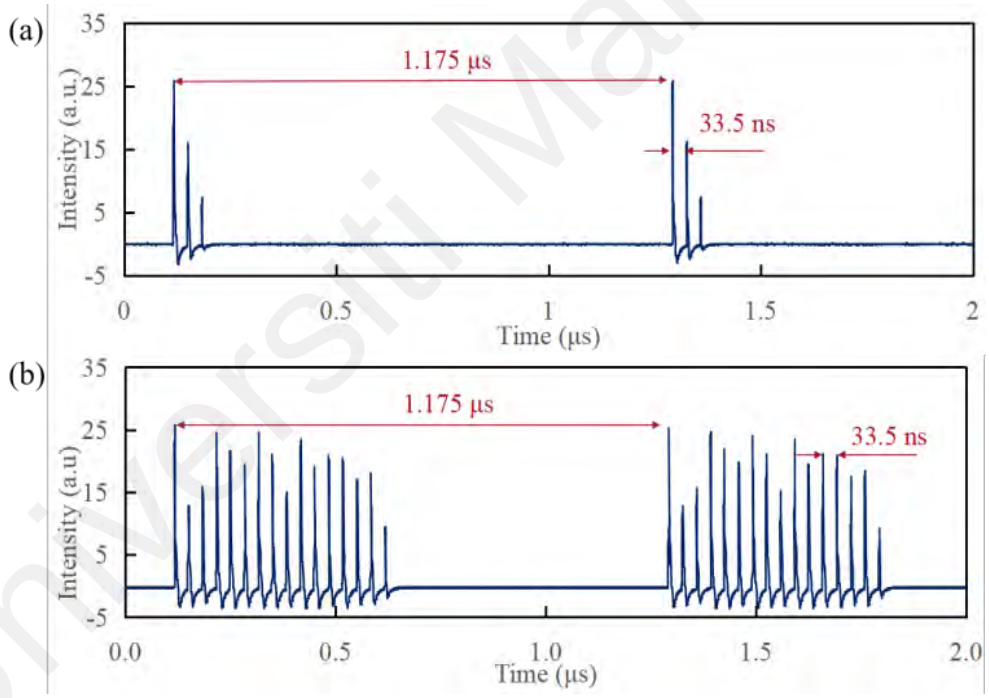

Figure 4.13: (a) Oscillation trace of pulses at pump power of 23.2 mW pump power. (b) Oscillation trace of pulses at pump power of 220 mW pump power.

At pump power 152 mW, the pulse stability was examined with Radio Frequency Spectrum Analyzer (RFSA). Referring to Figure 4.14(a), signal to noise ratio (SNR) of

64 dB was revealed at the fundamental repetition rate 850.8 kHz, signifying the stability of bunched pulses. Additionally, RF spectrum modulation was also observed in Fig. 5(b), for frequency span 0 to 40 MHz. Interestingly, additional peaks were discovered when the frequency range was increased to 200 MHz. Figure 4.14(b) shows these peaks at every 29.9 MHz interval. This 29.9 MHz corresponded to the spacing between each pulse in a rectangular envelope bunch, which was 33.5 ns. The inference RF spectrum between the bunch pulses and a single pulse resulted in frequency peaks at intervals of 29.9 MHz. Figure 4.15 shows the autocorrelation trace whereby the pulse width was ascertained at 290 fs when it was fitted to a sech2 fitting. The obtained pulse width was narrow, owing to the dispersion compensation effect from DCF. The maximum recorded average bunch pulses energy was 7.388 nJ.

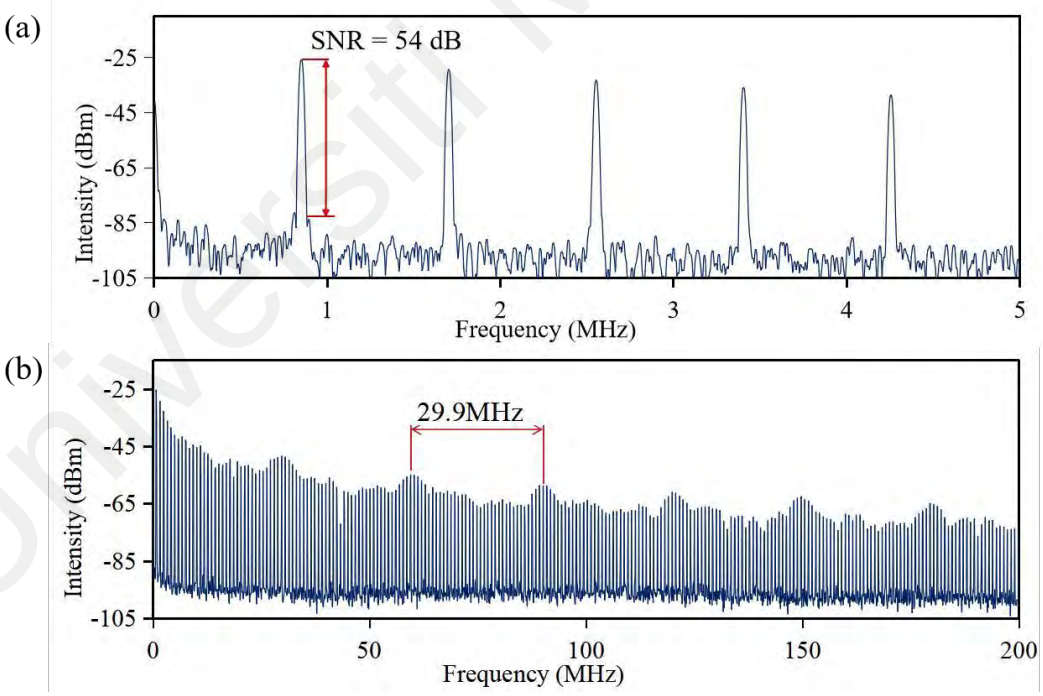

Figure 4.14: RF spectrum of bunch pulses at different frequencies span. (a) RF spectrum at 5 MHz span. (b) RF spectrum at 200 MHz span.

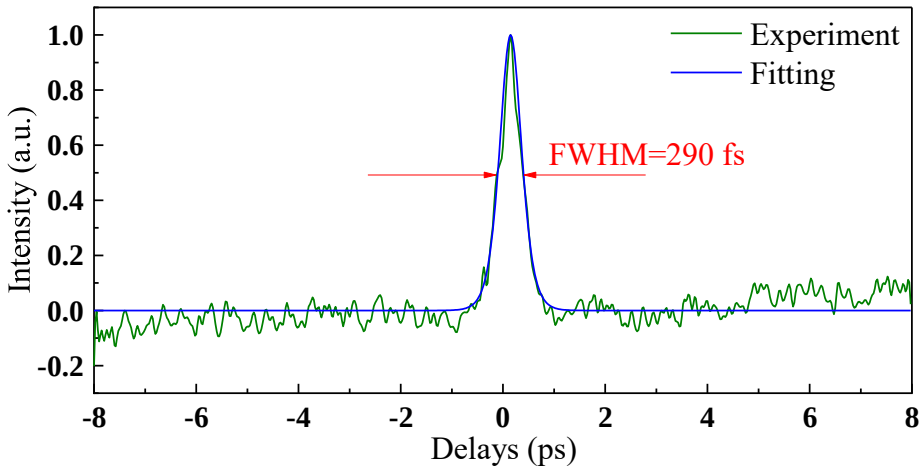

Figure 4.15: Pulse width measurement with autocorrelator.

To sum up, the generation of multi-pulses in a bunch envelope from an EDFL modelocked ring cavity was described in this section. By using DCF, the cavity operated in net normal dispersion regime. A simple SMS structure using only a segment of GIMMF was proposed to act as artificial SA. The laser was capable of generating 90 nm wide dissipative solitons with pulse width of 290 fs and repetition rate at 851 kHz. Without external perturbation, the multi-pulse operation was very stable with an SNR of 54 dB. It is believed that this work will be useful to understand the dynamics of multi-pulse in EDFL using SMF-GIMMF-SMF structure as artificial SA.

4.4 Harmonics of Dissipative Soliton

As previously discussed, HML is a commonly employed technique to achieve high pulse repetition rates. HML is typically achieved by incorporating dispersion management devices or highly nonlinear materials into the fiber laser cavity to facilitate the splitting of pulses into multiple components (Li et al., 2023; Tang et al., 2009). The investigation of HML in a net normal dispersion regime in EDFLs using artificial SAs was pioneered by Komarov et al. (2006). Recently, numerous researchers have experimentally demonstrated HML utilizing artificial SAs (Peng et al., 2013; Y. Wang et al., 2017). HML

in the net normal dispersion regime in EDFLs using SMS structures as artificial SAs has also been reported (G. Chen et al., 2021; Guangwei Chen, 2021; Li et al., 2023; Wang et al., 2022; T. Wang et al., 2020; B. Zhang et al., 2023). This section demonstrates a passive HML in an EDFL using SMS structure as artificial SA.

When the pump power surpasses a certain threshold, multiple pulses can be generated due to the overdriving of mode-locking mechanisms such as nonlinear polarization rotation (NPR). Under specific conditions, the spacing between these multiple pulses can equalize, leading to HML. Various mechanisms have been proposed to explain this phenomenon. For instance, the acousto-optic effect suggests that a pulse generates a transverse acoustic wave, which modulates the local refractive index of subsequent pulses. Additionally, it has been suggested that gain depletion within a soliton fiber laser can generate the necessary force for HML. Furthermore, the interaction between soliton pulses and the continuum wave can generate a pulse-topulse repulsive force, also contributing to HML.

4.4.1 Experimental Setup

The SMS structure and the cavity used in this experiment is the same as in 4.3.1. Thus, the linear and nonlinear characterization of the SMS structure can be found in Figure 3.27 and Figure 3.28 respectively. The schematic drawing of the mode-locked EDFL cavity with dispersion management using SMF-GIMMF-SMF as SA is shown in Figure 4.9. The description of the cavity components could be found in sections 4.2.2 and 4.3.1.

4.4.2 Harmonics of Dissipative Soliton Performance

Pump power is gradually increased to 23.2 mW and with the appropriate rotation of PC, mode-locking operation is observed. The variance of core diameter between SMF and

MMF promotes multimode interference and coupling of high-power signals, effectively simulating an SA. The optimal length of GIMMF, together with the low loss cavity contributed to the low threshold power to initiate mode-locking. The repetition rate is revealed at fundamental mode-locking (FML) of 858 kHz, and it corresponded with the total cavity length of 239.5 m. Without changing the orientation of PC, the pump power is further increased. When it reached 36 mW, the fundamental repetition rate doubled to 1.72 MHz, and it regarded as 2^{nd} harmonic mode-locking. 3^{rd} (2.56 MHz) and 4^{th} (3.40 MHz) harmonic mode-locking commence at pump power 53.9 mW and 73.4 mW, respectively. Once the pump power touches 97 mW, the repetition rate changes from 3.40 MHz to 4.29 MHz. As the pump power is further increased up to the maximum available pump power, 5^{th} harmonic mode-locking remained. This process is reversible, indicating that when the pump power is reduced, the harmonic order reduces from 5^{th} harmonic to fundamental mode-locking. The occurrence of harmonic modelocking can be explained as follows. When pump power is raised, the pulse intensity circulating in the cavity increases along. Nevertheless, the increase of pulse intensity is limited due to gain depletion in the laser cavity. In this scenario, the pulse peak power is kept to a limit. The clamping of the pulse modulates the intensity of pulse train, hence causing it to exhibit periodic modulation behavior at multiples of the fundamental frequency, and equally distributed. Additionally, the nonlinear phase modulation induced GIMMF can effectively phase lock the pulses at multiple of the fundamental repetition rate. The evolution of pulse train from fundamental repetition rate to 5^{th} harmonic is represented in Figure 4.16. The spacing between oscillation traces gets closer to each other as pump power is increased. As the oscillation traces are nearer to each other, the repetition rate increases. Figure 4.17 illustrates the contour view of the pulse train transformation, showing that the number of peak oscillations increases with pump power.

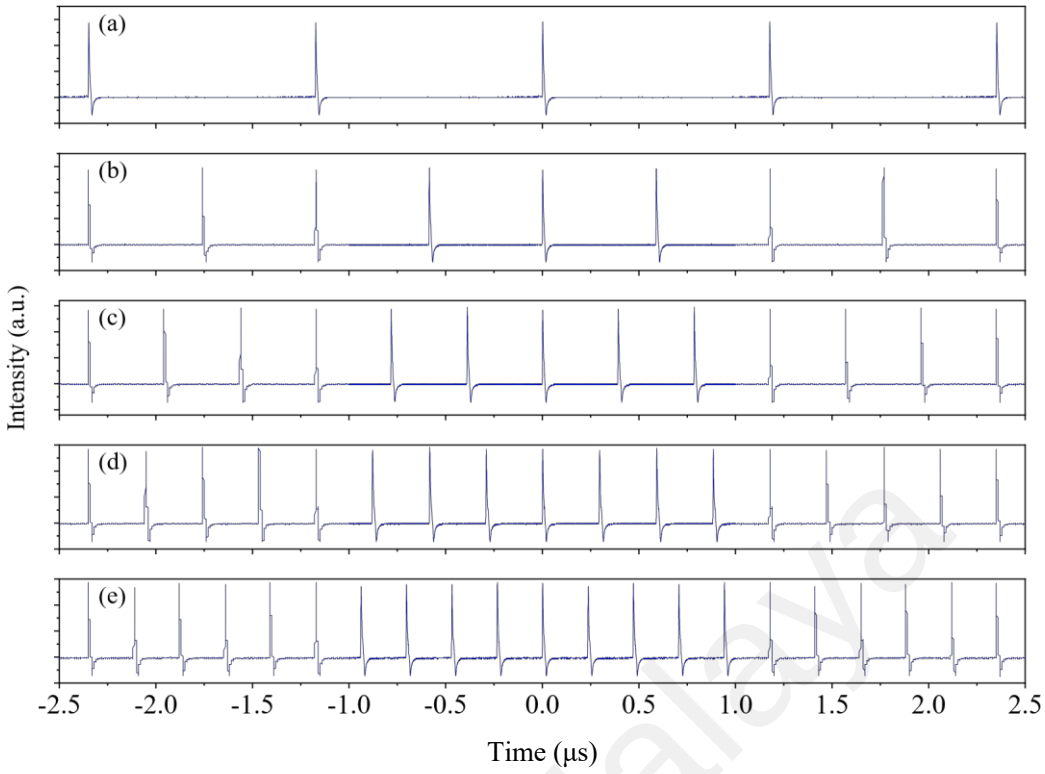

Figure 4.16: Pulse trains of the laser: (a) FML at 858 KHz, pump power 23.2 mW (b) 2nd HML at 1.72 MHz, pump power 36.0 mW (c) 3rd HML at 2.56 MHz, pump power 53.9 mW (d) 4th HML at 3.40 MHz, 73.4 mW (e) 5th HML at 4.29 MHz, pump power 97.0 mW

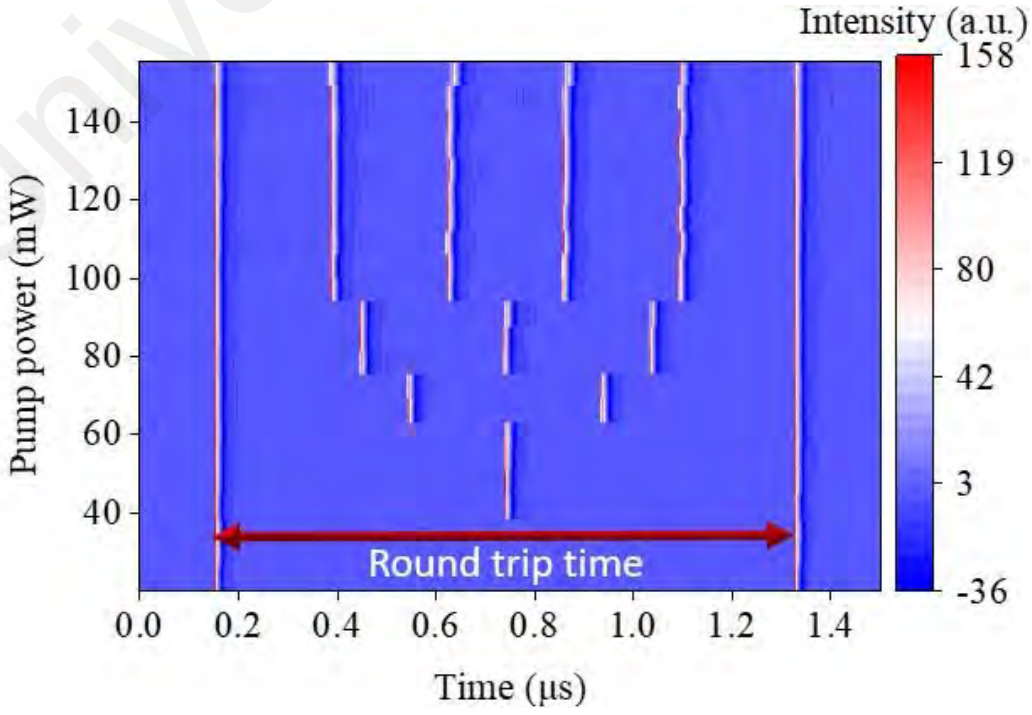

Figure 4.17: 2D contour view of pulse train at various pump power

The corresponding optical spectrum with the harmonic order is illustrated in Figure 4.18. The peak power increases while the spectrum broadens with pump power. The peak power increases from -17.96 dBm (FML) to -15.25 dBm (5th harmonic), while maintaining the center wavelength at 1572 nm.

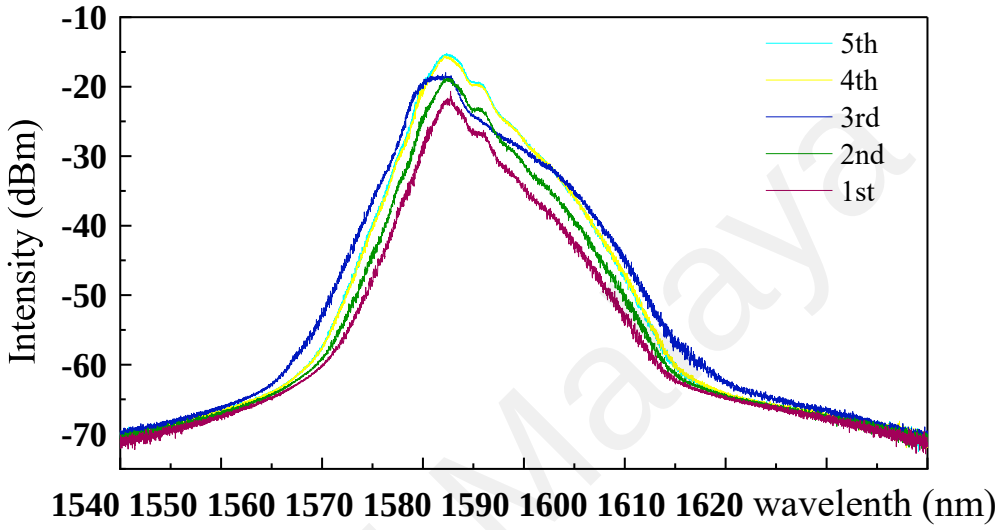

Figure 4.18: Spectrum of different orders of HML at different pump powers.

Figure 4.19 illustrates the pulse width obtained at 5th harmonic order. The estimated pulse width is 290 fs using gaussian curve fitting. The narrow pulse width is due to the pulse compression by a 3-meter long SMF outside of the cavity at the output port. The pulses are negatively chirped due to the normal dispersion, but it was recompressed by the 3-meter long SMF.

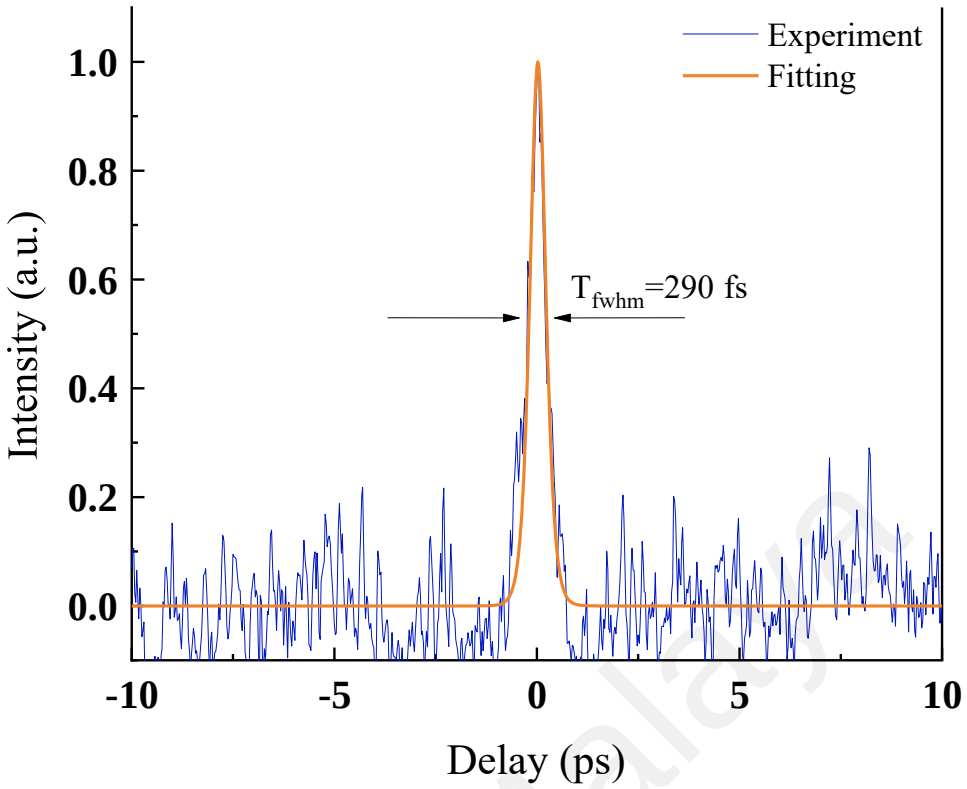

Figure 4.19: Autocorrelation trace of the pulse at 5th harmonic.

Figure 4.20 shows the signal-to-noise (SNR) ratio of the harmonic pulses. The SNR kept above 50 dB for all the harmonic orders, which indicated the switching of harmonic orders are highly stable. Insets show the broader span of frequency spectrum up to 500 MHz. No obvious spectral modulation is observed, which further validated the stability for all harmonic orders.

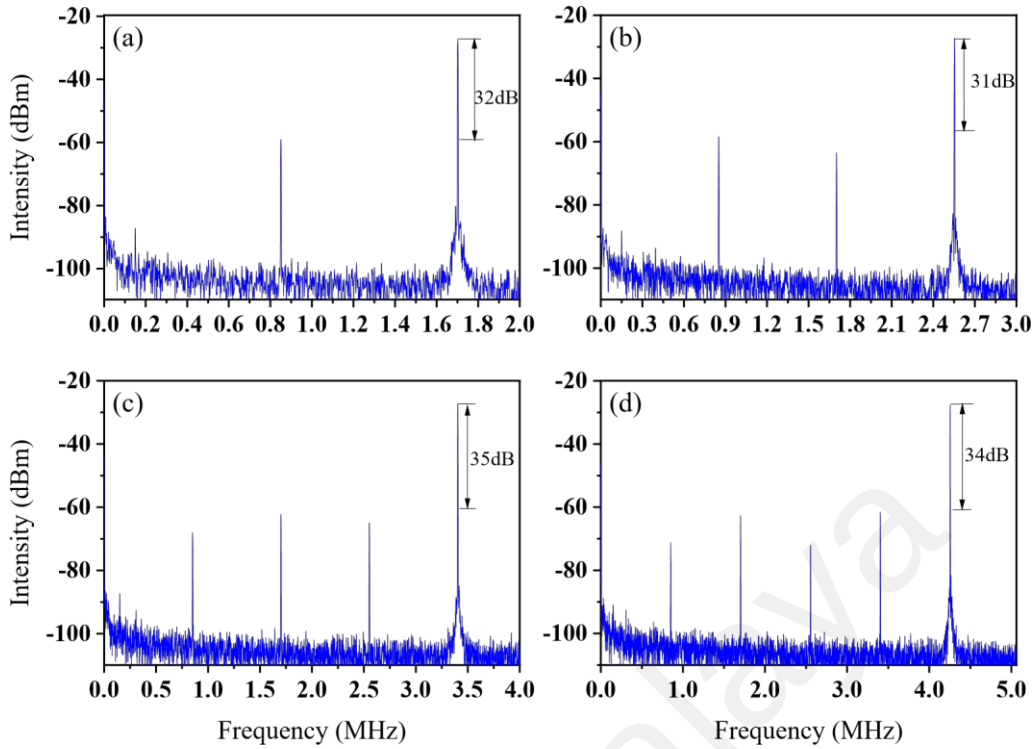

Figure 4.20: RF spectrum: (a) 2nd HML at 1.72 MHz (b) 3rd HML at 2.56 MHz (c) 4th HML at 3.40 MHz (d) 5th HML at 4.29 MHz

The output power throughout the mode-locking operation is traced as depicted in Figure 4.21. The output power increases with pump power, and the maximum output power is recorded as 12.9 mW. The corresponding pulse energy is 3.0 nJ. Harmonics order beyond 5th harmonics is not observed within the available pump power. It could probably be due to saturation of gain medium. The increment of pump power is not proportional to the increase in gain. Thus, it cannot amplify the pulse to higher harmonic order efficiently. A literature review shows that the threshold power to achieve mode-locking operation in this work is relatively lower, and the pulse width is outperformed as compared to other works.

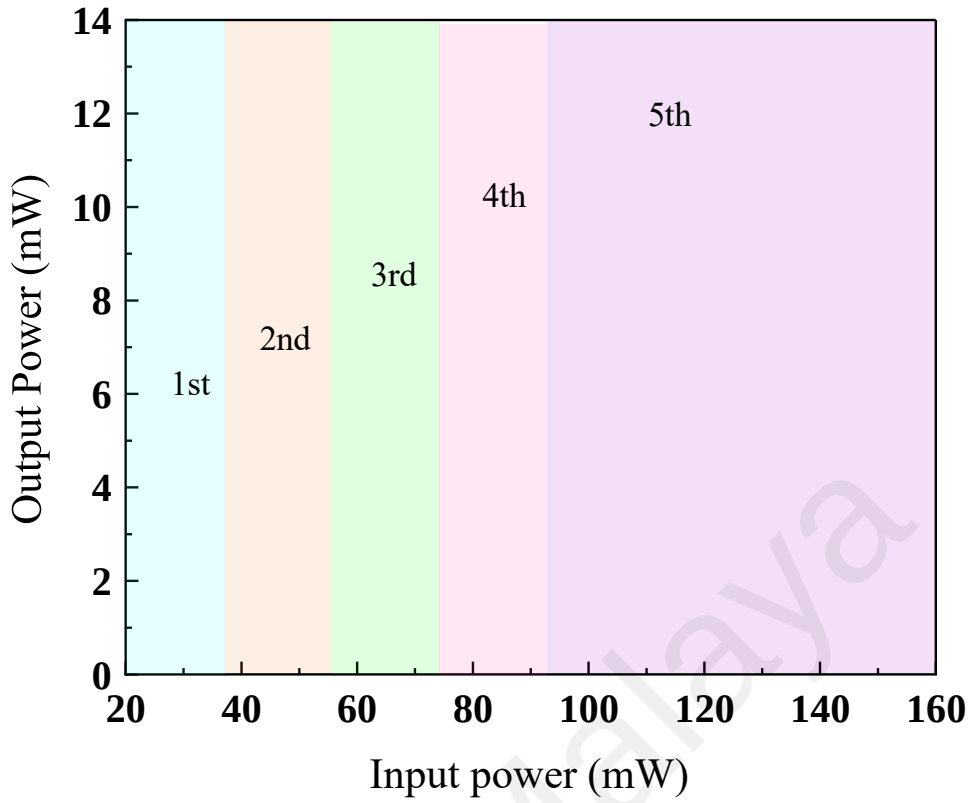

Figure 4.21: Output power vs. input power at different harmonic orders.

In conclusion, passive HML is demonstrated in an EDFL using SMS fiber as artificial SA in this section. By increasing the pump power, FML evolves progressively to 5th harmonic order, with 5th order repetition rate of 4.29 MHz. The pulse width and pulse energy at 5th harmonic is ascertained at 290 fs and 3.0 nJ, respectively. The SNRs are kept above 30 dB, demonstrating the high stability of the HMLs. This work shows that SMS structure as saturable absorber can generate stable harmonics in normal dispersion regime. For future work, the cavity design can be further optimized to avoid gain saturation so that higher harmonic orders can be generated.

4.5 Discussion

This chapter presented the experimental demonstration of bound state soliton, ultrawide spectrum dissipative soliton with multi-pulses and harmonics of dissipative soliton with SMS structures as artificial SA.

In section 4.2, mode-locked soliton and bound soliton in anomalous dispersion regime were demonstrated. After proper adjustment of the PC, loosely and tightly bound soliton were observed existing simultaneously. However, this kind of higher order soliton was not stable and quickly collapsed to a loosely bound soliton with constant time separation and varying intensity ratios. Bound soliton starts at a higher level of input pump power at 54 mW while the conventional soliton can start at as low as 29.3 mW within the same cavity. The spectrum of a bound soliton is wider than the conventional soliton. Besides, there are many ripples on the top area of the spectrum of the bound soliton, showing the special characteristics of the bound soliton. This characteristic aligned well with former theoretical and experimental studies. Recorded results showed that bound soliton had a larger pulse width at 740 fs than the conventional soliton, whose pulse width was only 650 fs.

Section 4.3 demonstrates the generation of multi-pulses in a bunch envelope from a mode-locked Erbium Doped Fiber Laser in a net normal dispersion ring cavity. A section of 10.3 cm long grade indexed multimode fiber was spliced in between single mode fibers to act as artificial saturable absorber. The mode-locking started at an extremely low pump power of 23.2 mW. By increasing the pump power from 23.2 mW to 220 mW, the number of pulses in a bunch envelope increased from three to sixteen. The repetition rate of the pulse was maintained at 851 kHz regardless of the number of pulses while obvious periodical peaks were observed in radio frequency analyzer at every 29.9 MHz. An ultra-wide spectrum was observed throughout the experiment, and it did not vary with pump power. The recorded pulse width and maximum average pulse energy was 290 fs and 7.388 nJ, respectively. The pulses were observed to be stable in the no external

perturbation lab environment. The venture of all-fiber pulse laser using the proposed artificial saturable absorber is potentially to pave the foundation toward practical applications.

Harmonics of dissipative soliton were demonstrated in section 4.4. Once fundamental mode-locking was realized, by increasing the pump power, the 2^{nd}, 3^{rd}, 4^{th} and 5^{th} harmonic were observed without adjusting the PC, and this process was reversible. The spectrum bandwidth increased with the increase of the harmonic while the SNR kept almost constant. The fundamental ML has a repetition rate of 858 kHz, and the repetition rate of the 2-5^{th} harmonic were 1.72 MHz, 2.56 MHz, 3.40 MHz, and 4.29 MHz respectively. Due to the large normal dispersion, the pulse chirped. However, it was compressed back at the output port, resulting in a narrow pulse width of 290 fs.

4.6 Summary

This chapter experimentally demonstrates three kinds of unconventional solitons, including bound soliton, ultra-broadband dissipative soliton with multi-pulses, and harmonics of dissipative soliton, using GIMMF bases SMS structures as artificial SA. The results show that GIMMF based SMS structures are good candidates for different kinds of soliton generation in EDFL. The objective for this chapter is accomplished.

CHAPTER 5: DARK PULSE OPERATION IN EDFL

5.1 Introduction

With the booming of telecommunication in the past several decades, bright solitons were used as the information carrier in the telecommunication system due to their high stability and narrow pulse width (Mollenauer & Smith, 1988). However, through indepth

study of dark solitons, researchers found that dark solitons might be even more suitable for telecommunication systems because the pulse broadening of dark solitons during propagation is nearly half the rate of bright solitons. Besides, dark solitons show more resistance to perturbations than bright solitons do, which is especially beneficial for long-haul communication systems. Moreover, dark solitons are less sensitive to background noise because the background noise affects mainly the background of the dark solitons instead of the pulses (Ge et al., 2015).

Dark solitons are recognized by the intensity dips on a constant noise background with a phase jump across their intensity minimum. According to the mechanism of the formation of the dark pulse, dark solitons can be categorized into three main types: nonlinear schrödinger equation (NLSE), Cubic-Quintic nonlinear schrödinger equation (CQNLSE) and Domain wall (DW) (Tiu et al., 2022). NLSE dark pulse relies on the change of linear refractive index coefficient in the cavity, thus, it exists only in normal dispersion regime (Boiti et al., 1982; Silva et al., 2019; Sylvestre et al., 2002). CQNLSE dark pulse only happens when there is strong nonlinearity in the cavity. While the formation of CQNLSE dark pulse requires sufficient light intensity to interact with the strong nonlinear medium to introduce higher order nonlinearities, it exists in fiber lasers operating in both normal and anomalous dispersion regimes (Tiu et al., 2015; Zhou et al., 2019). Domain wall dark pulse is formed due to the interaction of two or more lasing in different wavelengths that causes the topological defects in temporal domain. It does not rely on dispersion conditions, so it can be formed in both normal and anomalous dispersion fiber laser cavities. The most distinguishable characteristic of DW dark pulse is the dual-wavelength or multiple wavelength optical spectra of the DW dark pulse (V. E. Zakharov & A. B. Shabat, 1973).

In this chapter, domain wall (DW) dark pulses are demonstrated using single-modemultimode-single-mode (SMS) structures within both normal and anomalous dispersion regimes in an EDFL. Section 5.2 investigates the DW dark pulse generation

within the anomalous dispersion regime, while Section 5.3 highlights its occurrence within the normal dispersion regime.

5.2 Domain Wall Dark Pulse in Anomalous Dispersion Regime

Haelterman and Sheppard (1994) were the first to theoretically predict the existence of domain-wall dark pulses. Their insightful analysis revealed that the interplay between the cross coupling of two orthogonal polarization components within a dispersive Kerr medium could yield a stable localized structure, effectively delineating domains of the two orthogonal polarization fields, giving rise to the domain wall dark pulse. Importantly, their work demonstrated that this pulse type could propagate without distortion, unlike square-shaped carrier pulses, which suffer broadening due to diffraction and nonlinearity. Subsequently, Haelterman and Badolo (1995) further extended this understanding by revealing that the interaction of two optical waves with different frequencies, but the same polarization could also produce the formation of domain wall solitons, elucidating the concept of dual-wavelength domain-wall dark pulses.

Numerous researchers have previously demonstrated the existence of domain-wall dark pulses using both real and artificial saturable absorbers (SAs), predominantly in the anomalous dispersion regime. Among real SAs, Koo et al. (2019) harnessed Bi_2Te_3 to generate domain wall dark pulses within the 2 μm region. Similarly, other researchers employed black phosphorous, carbon nanotubes, and Fe_3O_4, respectively, to produce domain wall dark pulses within the 1.5 μm region (Li et al., 2018; Liu & Chow, 2014; Liu et al., 2019).

Regarding artificial SAs, the nonlinear polarization rotation (NPR) technique emerged as a widely utilized method for domain-wall dark pulse generation. Many researchers employed the NPR technique to demonstrate domain-wall dark pulses within the 1.5 μm region (Lin et al., 2012; Yin et al., 2010; Zhang et al., 2011), while P.

Wang et al. (2017) utilized NPR to demonstrate similar pulses within the 2.0 μm region. Furthermore, several researchers leveraged doped-fiber-based SMS structures as SAs for domain-wall dark pulse formation. Wenyan Zhang et al. (2019) utilized thuliumdoped fiber as an SA to generate bidirectional dark solitons, and they also demonstrated up to the 8th harmonic mode-locking of domain-wall dark pulses using a 0.8 mm long thulium-doped fiber as an SA. Notably, they observed an increase in the harmonic number with pump power, accompanied by a decrease in pulse width with the increment of the harmonic number.

This section aims to experimentally investigate the generation of domain wall (DW) dark pulses utilizing grade-index multimode fiber (GIMMF) based SMS structure as artificial SA.

5.2.1 Mechanism of DW Dark Pulse Formation.

The formation of DW dark pulses relies on the interaction of two or more lasing modes centered at different wavelengths, inducing topological defects in the temporal domain. Mathematically, DW pulses manifest as kinks, described by applying the Bäcklund transformation to the Nonlinear Schrödinger Equation (NLSE). The singlekink soliton is represented as follows:

$$_A(z,t) = 2\sigma \tanh\left[\sqrt{2}\sigma_0(t-t_0) + 4\xi_0 z\right] \exp\{i[-2\xi_0 t - 4(\sigma_0^2 + \xi_0^2)z - \theta_0]\}, \quad (5.1)$$

Here, σ_0 and ξ_0 are two real parameters, while the real constants θ_0 and t_0 determine the location of the traveling wave at the initial time. Remarkably, this equation illustrates that the formation of DW dark pulses is independent of the dispersion condition and can occur within both normal and anomalous dispersion fiber laser

cavities.

5.2.2 Experimental Setup

The SMS structure employed in this experiment mirrors the structure detailed in section 3.4.2, and its characteristics are consistent with those depicted in Figure 3.27 and Figure 3.28 in Chapter 3.

The experimental setup for the mode-locked Erbium-doped fiber laser (EDFL) utilizing the SMS structure as an artificial SA is illustrated in Figure 5.1. The fiber laser system is pumped by a laser diode (Oclaro LC96A74P-20R) emitting at a center wavelength of 974 nm. The pump laser and the oscillation light are coupled using a 980/1550 nm wavelength division multiplexer (WDM). The common port of the WDM is linked to a 2 m long Erbium-doped fiber (EDF, DF1100 Fibercore), serving as the gain medium. The laser output from the EDF is spliced to an isolator to ensure unidirectional light oscillation inside the ring cavity.

A 10.3 cm GIMMF is positioned between single-mode fibers (SMFs) to form an SMF-GIMMF-SMF structure. The GIMMF is integrated within an in-line polarization controller (PC), allowing for the adjustment of light oscillation phase by compressing the GIMMF. Adjacent to the in-line PC, a 3-paddle PC is connected. Proper adjustment of the 3-paddle PC enables its function as a polarizer to filter low-intensity modes and facilitate dark pulse formation. The ring cavity is closed by a 20/80 coupler, with 80% of oscillating light looped within the ring cavity and 20% tapped out for further analysis.

The optical spectrum is analyzed using an optical spectrum analyzer (OSA) (Anritsu, MS9710C) with a resolution of 0.02 nm. Real-time signal monitoring in the temporal domain is facilitated by a high-speed photodetector (ET-3500F) connected to a digital oscilloscope (GW Instek, GDS-3352). The stability of the dark pulse is evaluated in the frequency domain using an RF spectrum analyzer (Anritsu, MS2830A). The total length of the ring cavity is approximately 9.5 meters.

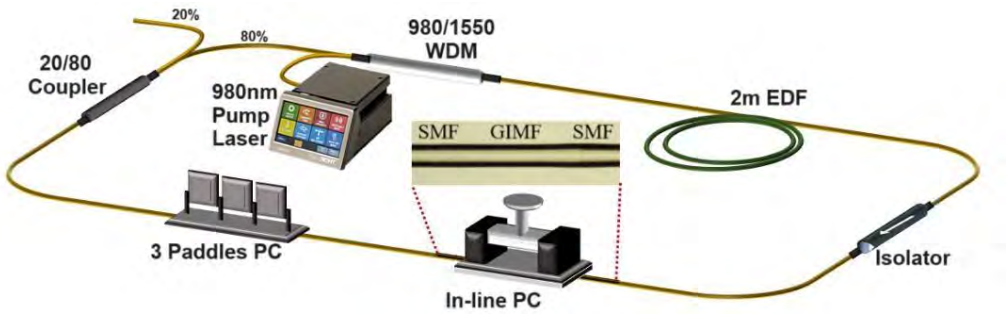

Figure 5.1: Experimental setup of the domain-walled dark pulse EDFL with SMF-GIMMF-SMF as artificial saturable absorber.

5.2.3 Laser Performances

In the proposed cavity setup, the SMF-GIMMF-SMF configuration acts as an interferometer, facilitating the generation of stable dual-wavelength emissions. Additionally, through precise adjustments of the 3-paddle PC, it serves as a polarizer, effectively filtering low-intensity modes and aiding in the formation of dark pulses. Collectively, the combination of the SMF-GIMMF-SMF structure and the PCs forms an artificial SA, crucial for inducing DW dark pulses within the cavity.

The self-starting of DW dark pulses occurs at a pump power of 97.0 mW and remains stable up to the maximum pump power of 195.4 mW. The presence of dual wavelengths, centered at 1567.2 nm and 1569.4 nm, is clearly observed, as depicted in Figure 5.2. The interaction between these dual peak wavelengths generates the topological defect in the temporal domain. Notably, the stable oscillation of the dual wavelengths within the ring cavity is consistently maintained across the entire pump power range from 97.0 mW to 195.4 mW, as evidenced by the 2D contour view.

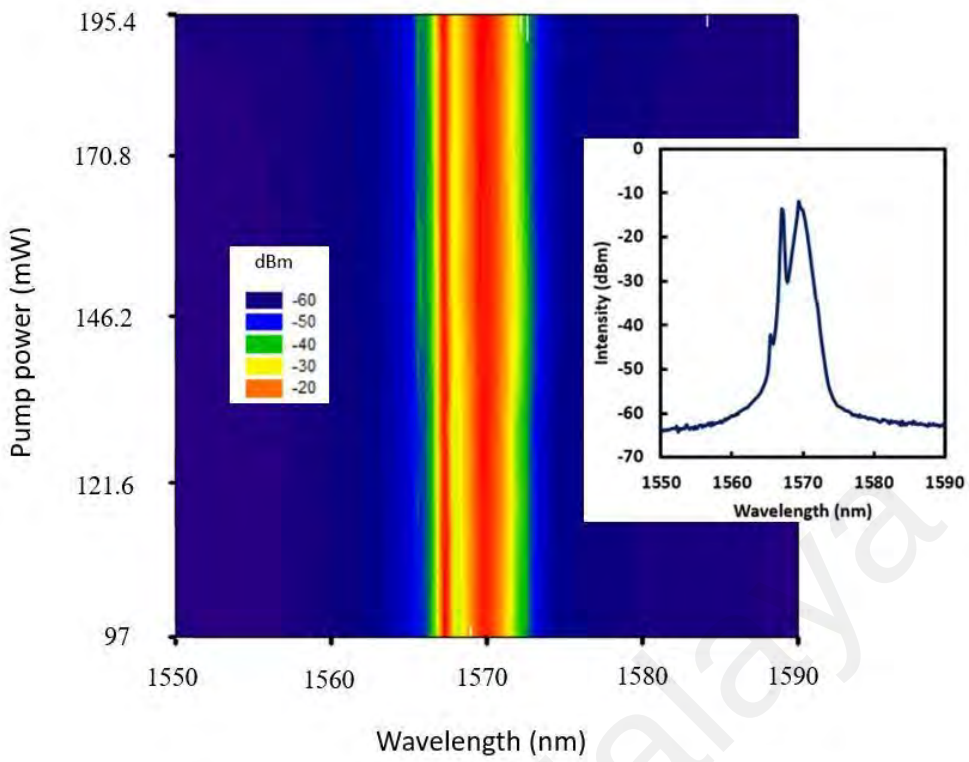

Figure 5.2: Wavelength domain of DW dark pulse throughout the operating pump power range. Inset is the optical spectrum at pump power of 195.4 mW.

The DW dark pulse is distinctly observed in the temporal domain, as depicted in Figure 5.3. As the dual lasing simultaneously occurs within the cavity, it results in the formation of topological defects in the temporal domain, manifesting as a narrow intensity dip amidst the strong continuous wave (CW) emission background. The pulse repetition rate is measured at 21.5 MHz, aligning precisely with the fundamental frequency derived from the 9.5 m cavity length. The full width half maximum (FWHM) of the dip is quantified at 5 ns. In comparison to emerging materials serving as real SAs, artificial SAs present advantages in their fabrication process. While emerging materials may offer the potential for achieving higher repetition rates, they often entail chemical fabrication processes. Conversely, artificial SAs can be constructed using optical components without the need for chemical processing, offering a more streamlined and versatile approach.

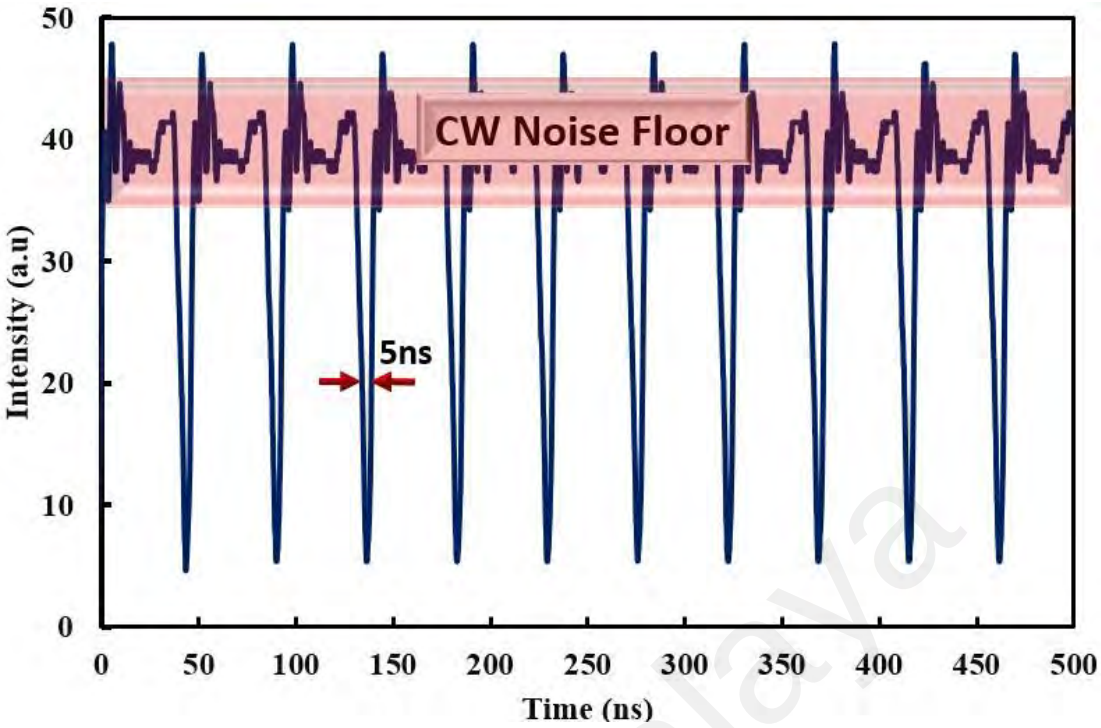

Figure 5.3: Temporal domain of DW dark pulse at pump power of 195.4 mW.

The performance of the DW dark pulse EDFL is further elucidated in Figure 5.4. Both the output power and average pulse energy exhibit a linear increasing trend with respect to pump power. Specifically, the output power escalates from 7.4 mW to 16.6 mW as the pump power rises from 97.0 mW to 195.4 mW. Similarly, the average pulse energy climbs from 345.0 pJ to 769.6 pJ within the same pump power range. Regression analysis of the output power against pump power reveals highly linear laser performance, with an impressive coefficient of determination $(R)^2$ value of 0.9999. Furthermore, the laser efficiency is quantified as 9.33%, highlighting the efficacy of the laser configuration.

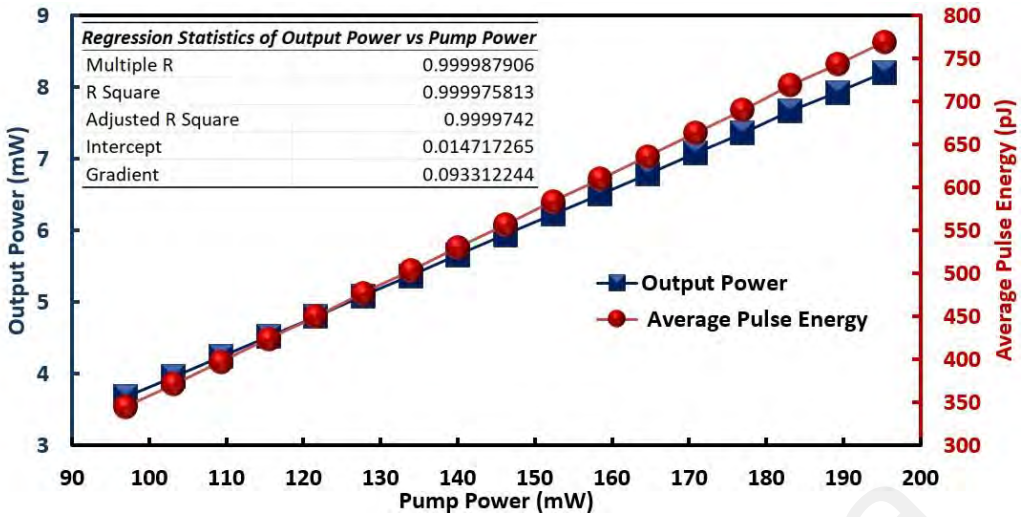

Figure 5.4: Output power and average pulse energy against pump power.

The stability of the DW dark pulse EDFL is also investigated utilizing an RF spectrum analyzer, as depicted in Figure 5.5. Notably, the DW dark pulse EDFL operates at the fundamental frequency of 21.5 MHz, in excellent agreement with the observed pulse train in the temporal domain. The signal-to-noise ratio (SNR) of the laser is measured at approximately 49 dB, indicating its operation under stable conditions. Remarkably, despite the presence of two lasing modes oscillating within the cavity, only a single frequency component is observed. This observation confirms the typical operation of DW dark pulses, wherein the topological defects induced by the interaction of the two lasing modes generate a single frequency component.

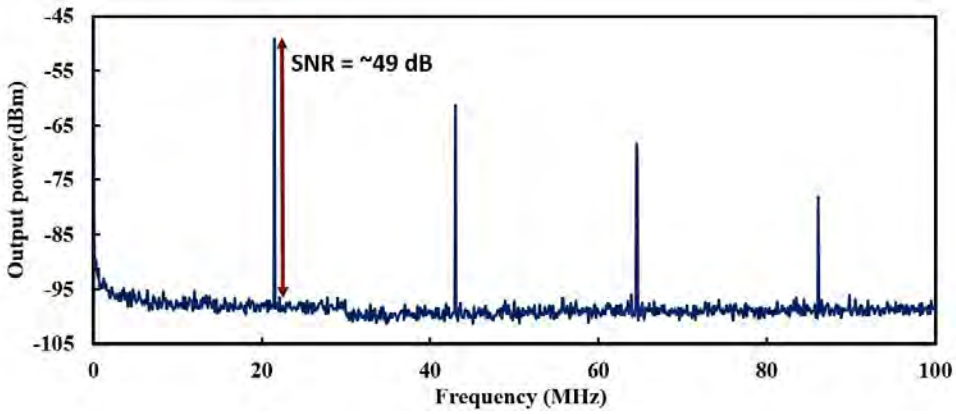

Figure 5.5：RF spectrum of DW dark pulse EDFL at pump power of 195.4 mW.

To summarize, the generation of DW dark pulses in an EDFL is successfully demonstrated utilizing an SMS fiber structure as both an interferometer and artificial SA. The SMS fiber consists of a 10 cm GIMMF sandwiched between SMFs. The interaction of dual wavelengths centered at 1567.2 nm and 1569.4 nm induces topological defects in the temporal domain, resulting in the formation of dark pulses with a repetition rate of 21.5 MHz. The highest average pulse energy recorded is 769.6 pJ, with a pulse width of 5 ns. Throughout the operational range of pump power, both average pulse energy and output power exhibit linear increases, with an R^2 value of 0.9999, achieving a laser efficiency of 9.33%. The stability of the DW dark pulse EDFL is assessed in the frequency domain, yielding a signal-to-noise ratio (SNR) of 49 dB. Compared to previous works on DW dark pulses, the proposed structure requires only a short length of multimode fiber, enabling the DW dark pulses to attain higher pulse repetition rates.

5.2.4 Performance Comparison of Dark Pulse in Anomalous Dispersion Regime Using Polyacrylonitrile as SA

To compare the performance of real SAs with the proposed SMS structure as an SA, the GIMMF was removed from the cavity, and fiber ferrules with connectors were spliced into the cavity, while keeping all other components unchanged. This re-splicing resulted

in an increased cavity length of 10.8 m due to the addition of SMF in the cavity. A polyacrylonitrile thin film was inserted between the fiber ferrules and integrated into an EDFL cavity, as illustrated in Figure 5.6. Polyacrylonitrile is a synthetic, semicrystalline organic polymer resin belonging to the family of one-dimensional structures. In this experiment, polyacrylonitrile powder was processed to form a thin film to function as a SA. The processing method can be referred to the procedure outlined in the work of Diblawe et al. (2023).

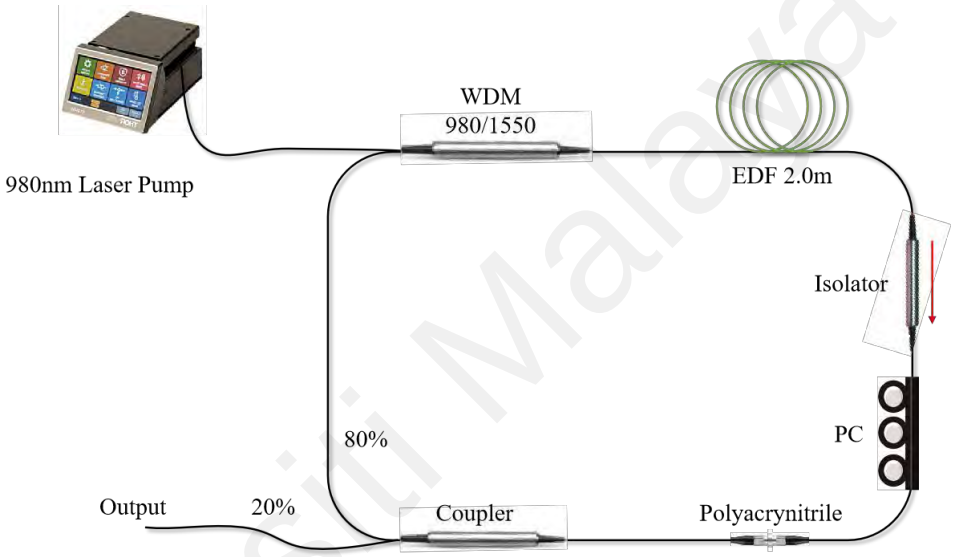

Figure 5.6: Schematic diagram of mode-locked EDFL cavity with as Polyacrylonitrile SA.

Figure 5.7 and Figure 5.8 depict the linear and nonlinear characterization of the polyacrylonitrile thin film, respectively. The linear transmission of the polyacrylonitrile thin film SA measures approximately 37.8% at a wavelength of 1570 nm. Notably, the SA exhibits a modulation depth of 7.3%, a saturable intensity of 1.18 MW/cm,² and a non-saturable loss of 37%. The high modulation depth and low saturable intensity of the polyacrylonitrile thin film affirm its suitability as a real SA. These characteristics indicate its potential efficacy in modulating cavity loss and facilitating the generation of stable mode-locked pulses within the laser cavity.

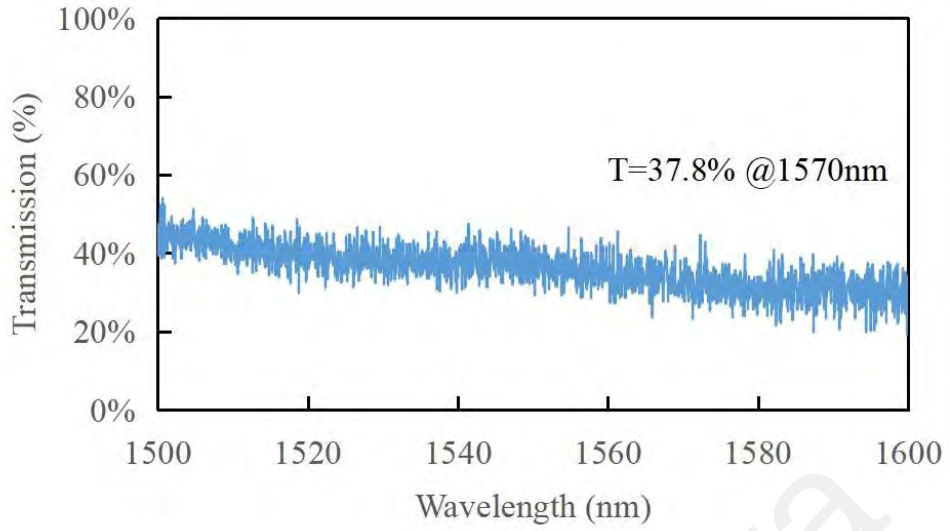

Figure 5.7: Spectral transmission of the polyacrylonitrile thin film SA.

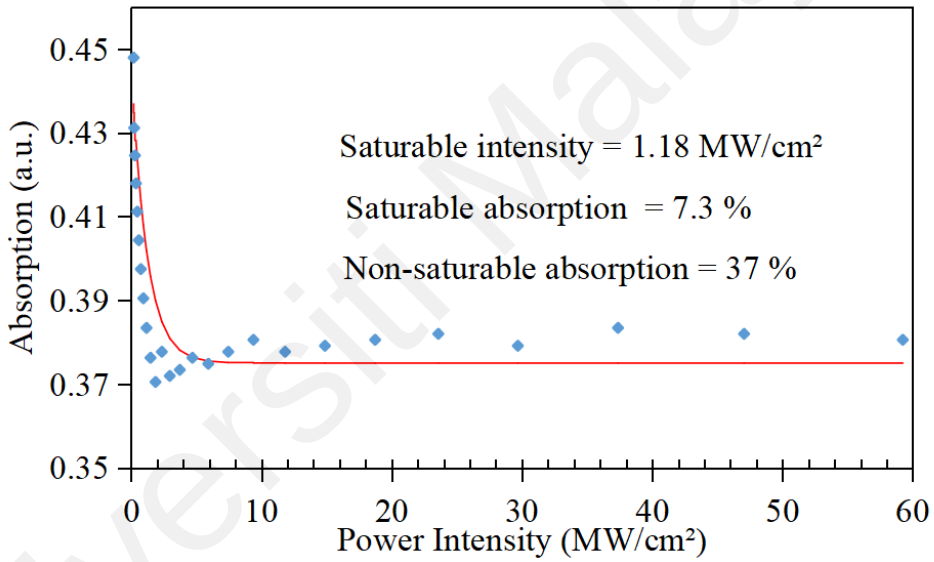

Figure 5.8: Absorption curve of the polyacrylonitrile thin film SA.

After securing the polyacrylonitrile thin film between the fiber ferrules and stabilizing it on the breadboard to prevent movement, the DW dark pulse can be easily generated by adjusting the 3 peddle PC. The dark pulse laser self-started at a pump power of 53.9 mW and its operation remained stable up to a maximum pump power of 127.7 mW. At the pump power of 53.9 mW, the presence of dual wavelengths was clearly observed, as shown in Figure 5.9. The interaction between the dual peak wavelengths centered at 1570.9 nm and 1571.9 nm induced topological defects in the temporal domain.

Additionally, two lower peaks were noticeable on each side of the higher peaks, with wavelengths centered at 1570.4 nm and 1572.7 nm.

As depicted in the 3D view, the spectra shapes evolved throughout the pump power range from 53.9 mW to 127.7 mW. However, all spectra consistently exhibited higher peaks at 1570.9 nm and 1571.9 nm, along with lower peaks at 1570.4 nm and 172.7 nm. This contrasted with the stable spectra observed for the domain wall dark pulse generated in Section 5.2.3 with the SMS structure. In this case, the domain wall dark pulse spectra demonstrated a dynamic evolution with increasing pump power.

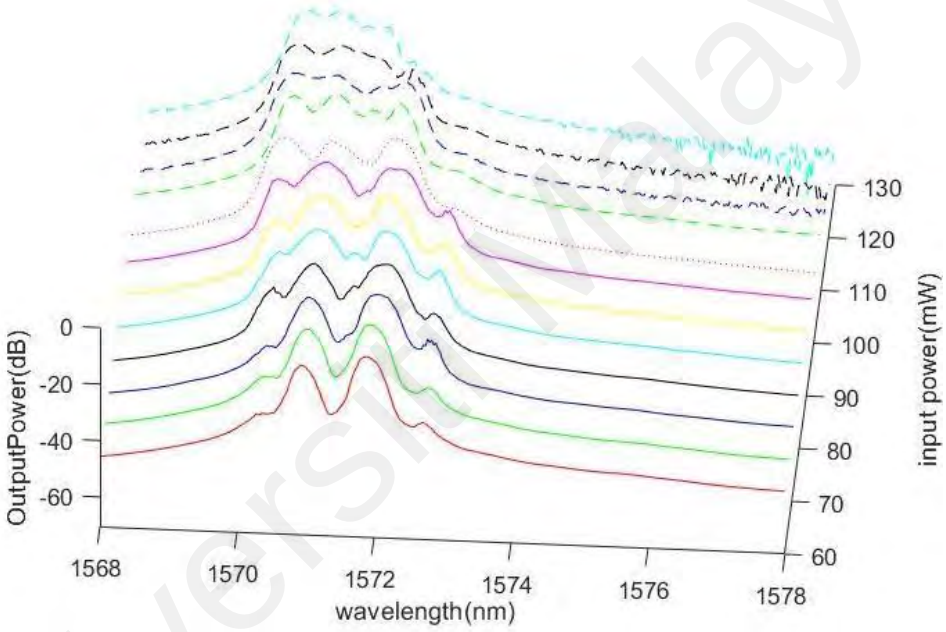

Figure 5.9：Wavelength domain of DW dark pulse throughout the operating pump power range.

The pulse train of the DW dark pulse is shown in Figure 5.10. The pulse repetition rate was recorded as 19.08 MHz, which shows the dark pulse is operating at the fundamental frequency, corresponding to the total cavity length of 10.8 m. Even though it is easier for real SAs to get higher repetition rate than the SMS structure as artificial SA, the repetition rate relies on the total cavity length. At a moderate length that leads to tens of megahertz, the real SAs don't show advantages over SMS structures. The

FWHM of the dip is measured as 1.56 ns. Compared with the FWHM of the dark pulse with SMS structure in section 5.2.3, this domain wall dark pulse has a shorter pulse width.

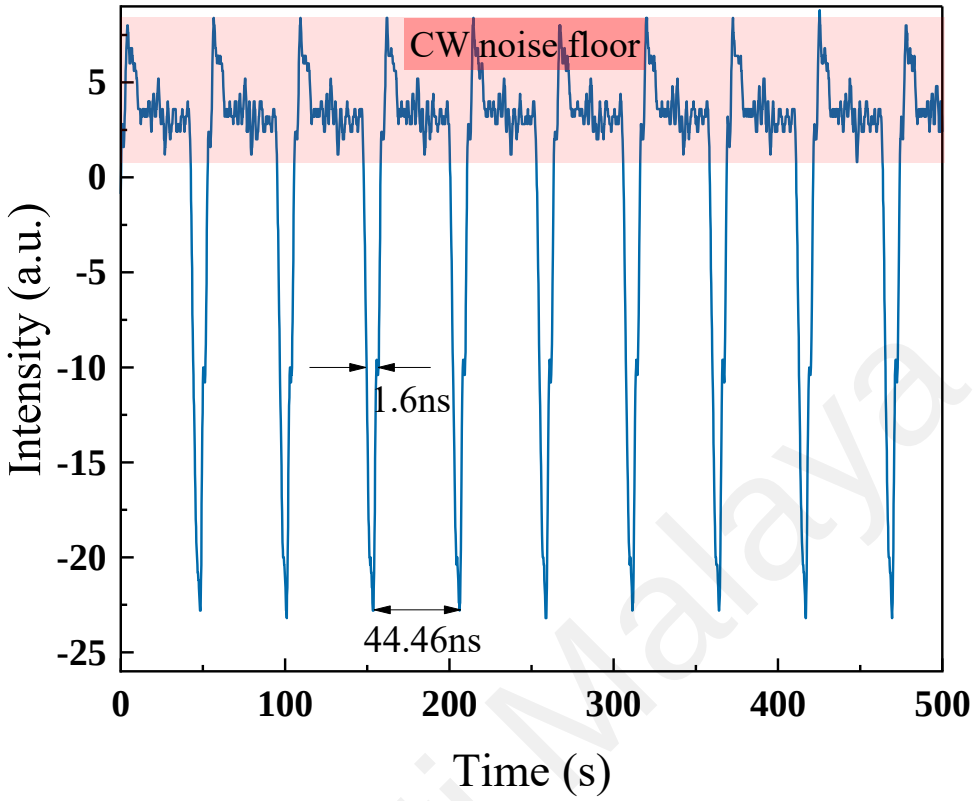

Figure 5.10: Temporal domain of DW dark pulse at pump power of 72.4 mW.

The DW dark pulse performance is further analyzed as shown in Figure 5.11. The output power and average pulse energy also exhibited a linear increasing trend against pump power. When the pump power increased from 53.9 mW to 127.7 mW, the output power increased from 4.59 mW to 12.23 mW and the average pulse energy increased from 241.6 pJ to 641.4 pJ. From the regression statistics of output power against pump power, the laser performance is highly linear with R^2 of 0.9998 and the slope efficiency is calculated to be 10.35%. The higher slope efficiency shows a better energy conversion with less loss in the cavity.

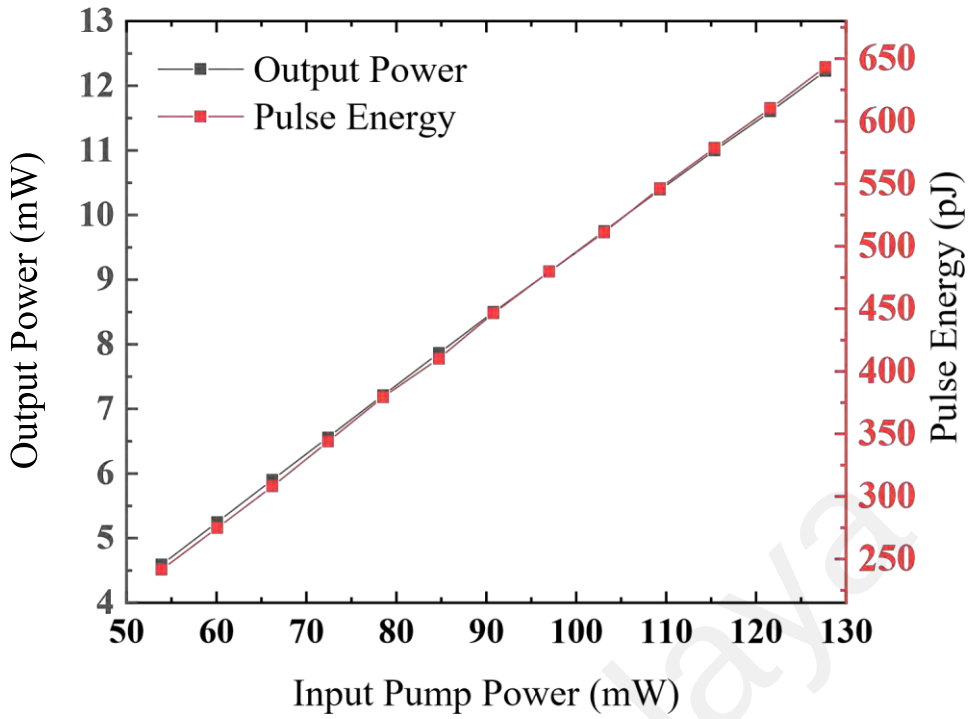

Figure 5.11: Output power and average pulse energy against pump power.

The stability of the DW dark pulse EDFL employing polyacrylonitrile thin film as a SA is also analyzed using an RF spectrum analyzer, as depicted in Figure 5.12. Notably, the DW dark pulse EDFL operates at a fundamental frequency of 19.08 MHz, which closely aligns with the observed pulse train in the temporal domain. The SNR of the laser measures approximately 58 dB, indicating a high degree of stability. Moreover, the presence of more harmonics over a larger frequency span in the RF spectrum analysis further substantiates the enhanced stability of this dark pulse compared to that generated in the previous section. Despite the presence of multiple lasing modes within the cavity, only a single frequency component is observed, confirming the typical operation of domain wall dark pulses.

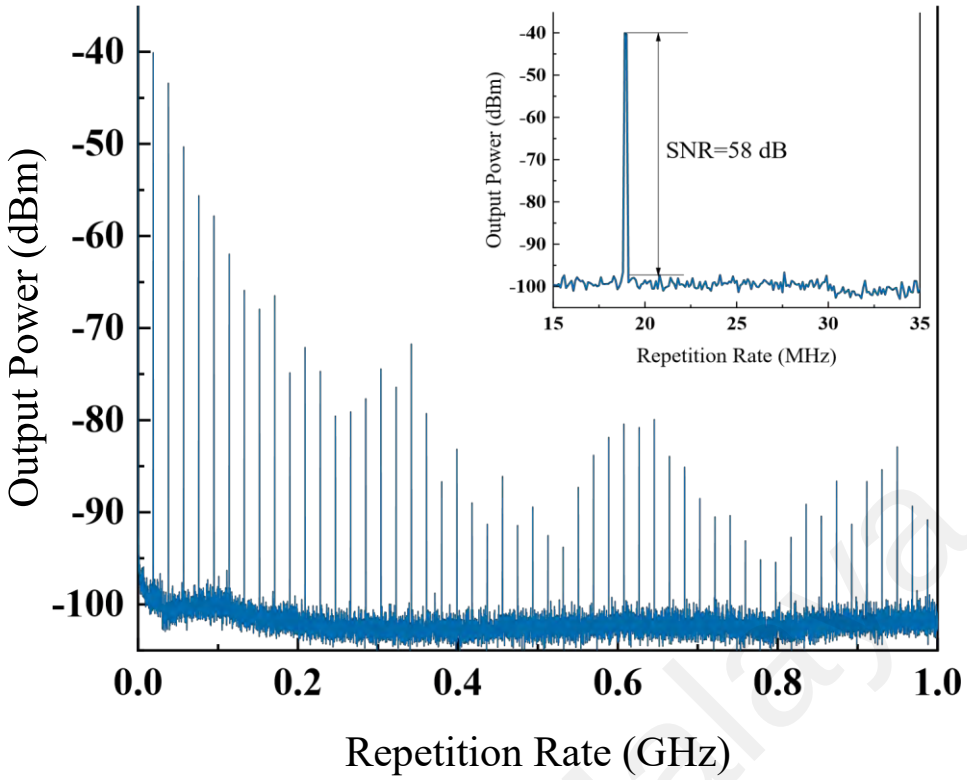

Figure 5.12： RF spectrum of DW dark pulse EDFL at pump power of 72.4 mW. Inset is the enlarged view of RF ranging from 15-35 MHz.

To summarize, domain wall dark pulses were successfully demonstrated in this section using two different approaches: the GIMMF-based SMS structure and polyacrylonitrile thin film as a SA. Both experiments were conducted within the same cavity under anomalous dispersion regime. In the case of the GIMMF-based SMS structure, the spectra of the domain wall dark pulse remained stable, with two peaks consistently observed at wavelengths of 1567.2 nm and 1569.4 nm across a wide range of pump powers from 97.0 mW to 195.4 mW. The spectra did not exhibit variations with increasing pump power, and the pulse train displayed uniform distribution with a narrow pulse width of 5 ns. On the other hand, employing polyacrylonitrile thin film as the SA resulted in dark pulse spectra that varied with increasing pump power. However, higher peaks at 1570.9 nm and 1571.9 nm, along with lower peaks at 1570.4 nm and

172.7 nm, remained visible for all pump powers ranging from 53.9 mW to 127.7 mW.

The pulse train remained uniform with a pulse width of 1.56 ns, showing no changes with increasing pump power. Interestingly, the SMS structure exhibited mode-locking at higher pump powers and sustained it up to higher pump powers compared to the polyacrylonitrile thin film. This suggests that the proposed SMS structure can withstand higher power levels than thin films. However, the slope efficiency of the dark pulse generated with polyacrylonitrile thin film was higher at 10.35%, indicating that it introduced less loss compared to the proposed SMS structure.

5.3 Harmonics of Domain Wall Dark Pulse in Normal Dispersion Regime

Indeed, while DW dark pulses can be generated in both anomalous and normal dispersion regimes, the majority of current experimental work has focused on demonstrating them in anomalous dispersion regime. One of the earliest experimental demonstrations was conducted by Zhang et al. (2011), who demonstrated dual wavelength DW dark pulses in an all-normal dispersion EDFL utilizing a polarizationdependent isolator. Notably, they observed a decrease in the pulse width of the dark pulses with increasing pump power, which was an intriguing finding. However, experimental results on harmonic mode-locked domain wall dark pulses are relatively scarce.

Lv et al. (2016) contributed to this area by conducting an experimental study on harmonic mode-locked dark solitons and bright-dark soliton pairs in an all-normal dispersion Ytterbium fiber laser with a long cavity length based on nonlinear polarization rotation. They observed up to the 4^{th} order harmonic mode-locked dark solitons when the pump power reached 611 mW. They noted that the spectra
characteristics of the bright-dark soliton pairs were similar to those of the single dark soliton mode-locked pulses, while the spectra of harmonic mode-locked dark pulses exhibited multiple peaks.

Additionally, W. Zhang et al. (2019) experimentally demonstrated harmonic modelocked bidirectional dark solitons in the anomalous dispersion regime for the first

time. They observed up to the 8th harmonic when increasing the pump power to 542.5 mW.

This section of the study focuses on the generation of harmonic mode-locked DW dark pulses with a GIMMF-based SMS structure. To the best of my knowledge, this is the first reported instance of high harmonic order domain wall dark pulse EDFL in the normal dispersion regime using a GIMMF-based SMS structure as an artificial SA.

5.3.1 Experimental Setup

The SMS structure utilized in this experiment aligns with the configuration described in section 3.4.2, which is based on a 10.3 cm long GIMMF. Therefore, the linear and nonlinear characterization of the SMS structure can be referenced from Figure 3.27 and Figure 3.28, respectively. In addition, Figure 4.9 in section 4.3 provides a schematic drawing of the mode-locked EDFL cavity with dispersion management using SMFGIMMF-SMF as the SA. All components within the cavity are identical to those described in section 4.3.1, except for the inclusion of a 230 m long dispersion compensation fiber (DCF) after the SMS structure. The dispersion of the DCF is specified as -4 ps/(km·nm). Consequently, the total cavity length is estimated to be 239.5 m. The calculated dispersion in the cavity is approximately 1.07 ps,² indicating that the cavity operates in the large net normal dispersion regime.

5.3.2 Domain Wall Dark Pulse in Normal Dispersion Regime Performance

The experiment commenced with the pump power set at 72.4 mW. With proper adjustment of the 3-paddle PC, clear mode-locked pulses became visible on the oscilloscope. These pulses persisted until the pump power decreased to 53.9 mW or increased to 176.9 mW. Figure 5.13 illustrates the presence of dual wavelengths, where the interaction between peaks centered at 1562.5 nm and 1569.9 nm induces topological

defects in the temporal domain. Analysis in a 2D contour view revealed minimal variation in spectra when the pump power was increased from 53.9 mW to 176.9 mW, indicating stable oscillation of the dual wavelength within the ring cavity across this range of pump power adjustments.

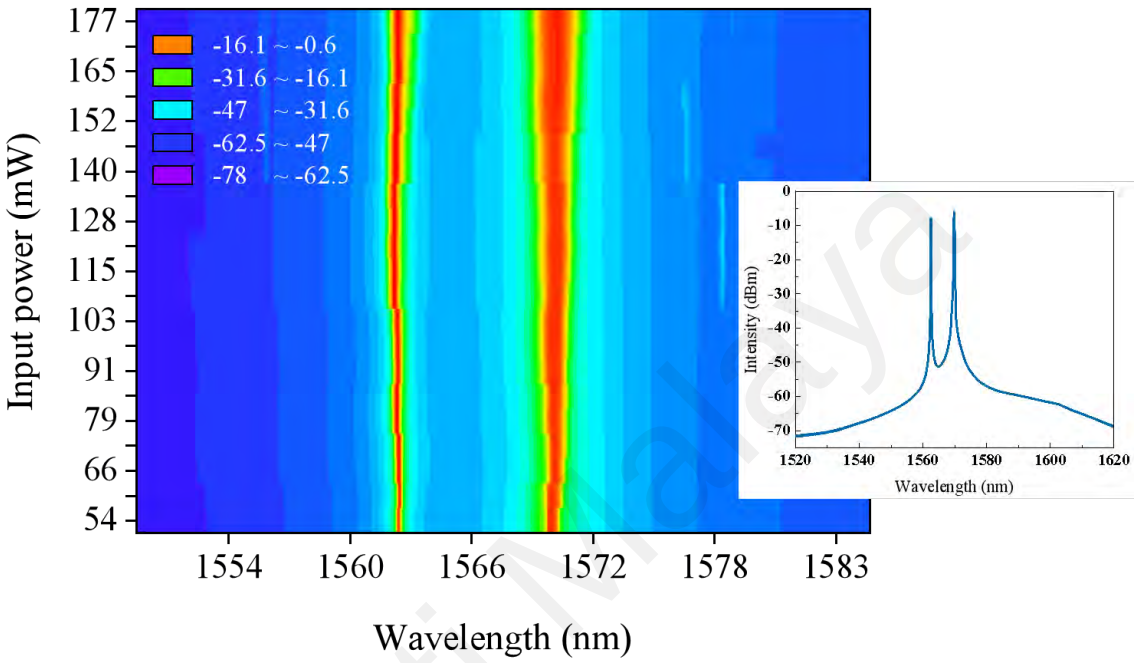

Figure 5.13: Wavelength domain of harmonic DW dark pulse throughout the operating pump power range in normal dispersion regime.

Figure 5.14 presents a typical pulse train of the DW dark pulse within the normal dispersion regime. In Figure 5.14 (a), the pulse exhibits uniform distribution in the time domain, indicating its high stability. The repetition rate of the pulse is measured at 139.8 MHz, corresponding to the operation at the 163rd harmonic considering the total cavity length, resulting in a fundamental repetition rate of approximately 858 kHz.

In Figure 5.14(b), an enlarged view of the pulses reveals a triangle shape attributed to the high order of harmonics. This phenomenon arises from the delicate balance between dispersion and high nonlinearity. Within a large net normal dispersion regime, lower frequency pulses travel faster than higher frequency pulses. However, the latter experiences larger intensity-dependent refractive index and smaller group velocity. Consequently, the co-propagating dark pulses couple and move together within the cavity,

ultimately forming a triangle pulse shape (W. Zhang et al., 2019). Even though the noise floor of the pulse was not obvious, the spectra together with the cavity setting in normal dispersion confirmed that the pulse was dark pulse. The FWHM of the pulse was measured as 4.21 ns with a pulse period of 7.18 ns. The harmonic mode-locking produced a higher repetition rate with the relatively long cavity length.

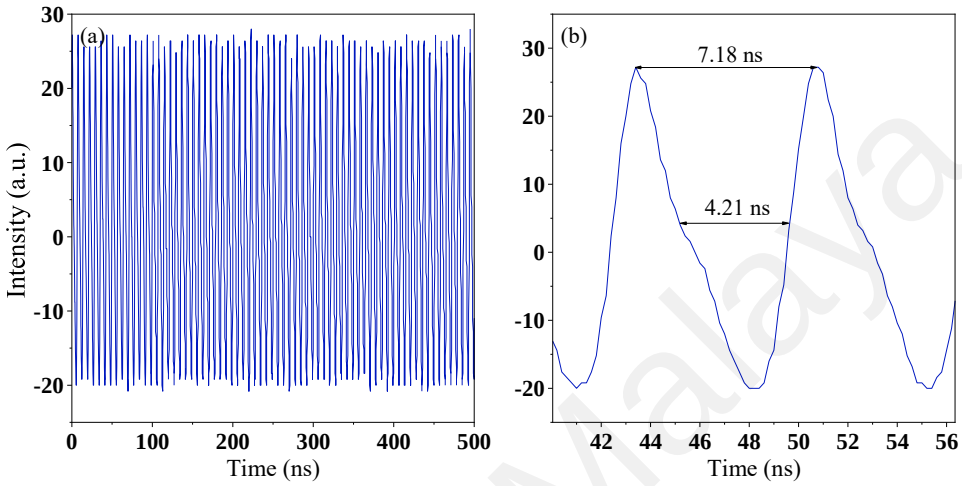

Figure 5.14: Pulse train of the harmonic DW dark pulse at pump power of 53.9 mW.

The stability of the harmonic of the DW dark pulse EDFL is investigated using RF spectrum analyzer. Figure 5.15 is the RF spectrum of the harmonic of DW dark pulse EDFL at pump power of 53.9 mW. It shows that the DW dark pulse EDFL operated at a repetition rate of 139.8 MHz, which was the 163rd harmonics of the fundamental pulse repetition rate. The SNR of the laser was around 35 dB with few super-mode noise shown on the RF spectrum, which indicated that the laser operated in a relatively stable condition. Even though there are two lases oscillating in the cavity, only a single frequency component was observed, which confirmed a typical DW dark pulse operation.

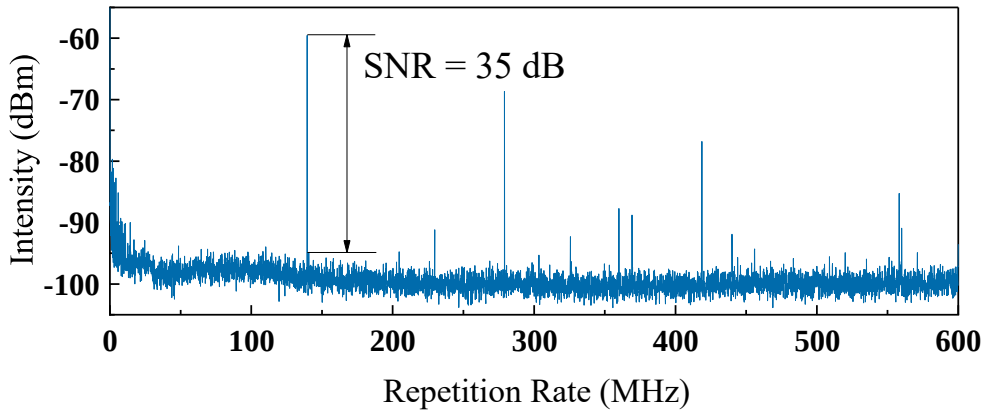

Figure 5.15: RF spectrum of the harmonic DW dark pulse EDFL at pump power of 53.9 mW.

The output vs. input power and the average pulse energy vs. input power of the DW dark pulse EDFL is shown in Figure 5.16. Both output power and average pulse energy linear increased against pump power. The output power increased from 3.67 mW to 15.31 mW as pump power increased from 53.9 mW to 176.9 mW. Due to the high repetition rate, the average pulse energy was relatively small. The average pulse energy increased from 26.3 pJ to 109.7 pJ when the pump power increased from 53.9 mW to 176.9 mW. A linear fitting was done for the output power vs. the input pump power, the laser performance was highly linear with R^2 of 0.9999 and the laser efficiency is reported as 9.51%.

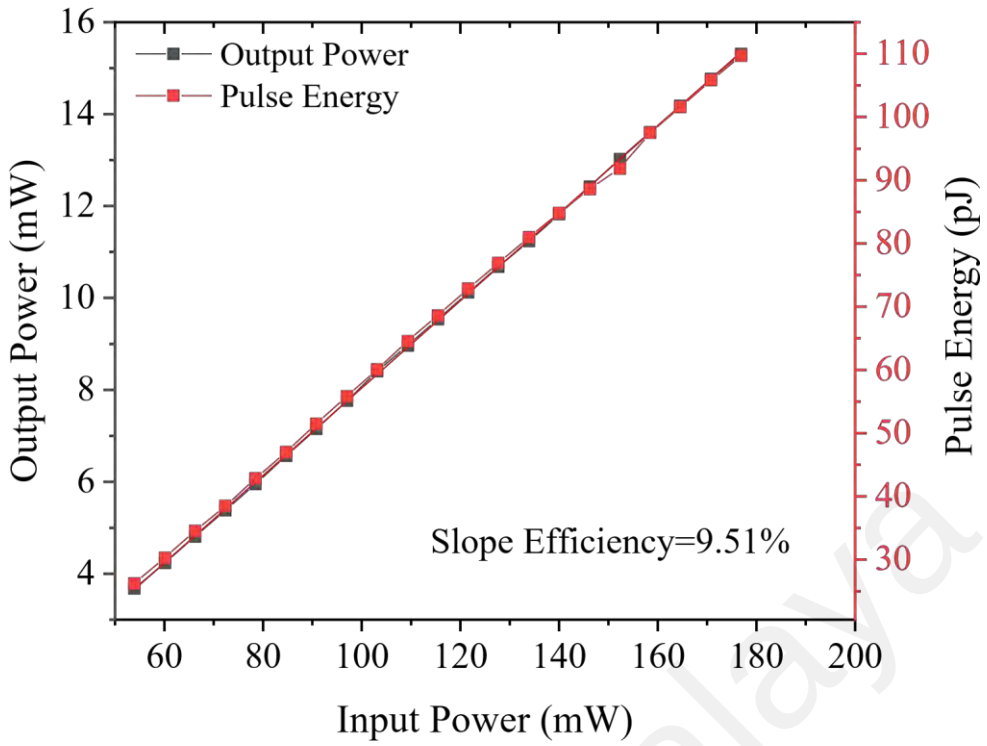

Figure 5.16: Output power and average pulse energy against pump power of harmonic DW dark pulse in normal dispersion regime.

In conclusion, the 163rd harmonic of DW dark pulse in normal dispersion regime is demonstrated in this section. Due to the interaction of lasing at different frequency, dual peak wavelengths centered at 1562.5 nm and 1569.9 nm were observed in the wavelength domain. Due to the high harmonic order, the pulse didn't show strong noise floor. Instead, a triangle pulse with a pulse width of 4.21 ns was observed. Even though the super mode noise was small, the SNR of the operation was 35 dB, showing a relatively stable operation. The pulse was maintained with an input pump power range from 53.9 mW to 176.9 mW. The output power and pulse energy showed a highly linear relationship with the input power, with a slope efficiency of 9.51%, indicating a relatively low loss in the cavity. This work confirms that SMS structure is a good candidate for DW wall dark pulse formation, providing a new way of dark soliton generation and a background to further understand the dynamics of harmonic modelocked dark pulse. In the meantime, it also confirms that dark solitons, just as the bright solitons, are intrinsic features of mode-locked lasers.

5.4 Discussion

This chapter details the generation of DW dark pulses in an EDFL utilizing SMS structure as a SA. These dark pulses were successfully generated in both normal and anomalous dispersion regimes.

In section 5.2, domain wall dark pulses were generated in the anomalous dispersion regime. The pulse exhibited a spectrum with two distinct peaks at 1567.2 nm and 1569.4 nm, consistent with DW dark pulse characteristics. The pulse initiation occurred at a pump power of 97.0 mW and sustained until 195.4 mW, displaying good inputoutput linearity. Moreover, no significant changes were observed in the spectra with increasing pump power, indicating stable operation. The uniform pulse train and a high SNR of 49 dB highlighted the mode-locked pulse's high stability. The repetition rate and FWHM of the pulse were measured at 21.5 MHz and 5 ns, respectively. To compare the results with real SA, the SMS structure was replaced with a piece of polyacrylonitrile thin film. The thin film exhibited higher modulation depth and lower saturable intensity compared to the SMS structure. The resulting DW dark pulse with polyacrylonitrile thin film as SA displayed more than two peaks in the spectra, which varied with increasing pump power. Despite having a smaller FWHM, it exhibited a higher SNR. However, the maximum power that the polyacrylonitrile thin film could withstand was smaller than the proposed SMS structure, highlighting the latter's higher damage threshold.

In section 5.3, the generation of the 163rd harmonic mode-locked DW dark pulse was demonstrated for the first time. The cavity was set in a large normal dispersion regime, and the pulse exhibited dual wavelengths on the spectra, consistent with DW dark pulse characteristics. Despite the high harmonic order, the pulse train displayed minimal super-mode noise, indicating excellent stability. A linear relationship between input and output power was observed, with a slope efficiency of 9.51%, indicative of low cavity losses.

5.5 Summary

This chapter demonstrates the potential of the proposed SMS structure as an SA for DW dark pulse formation, furthering the understanding of dark pulse dynamics. It reaffirms the SMS structure's versatility as an artificial SA, promising in various soliton formation applications. The objective of dark pulse formation with SMS structure and evaluation of SMS performance is accomplished.

CHAPTER 6: CONCLUSION AND FUTURE WORK

6.1 Conclusion

This thesis aims to demonstrate passive Q-switched and mode-locked pulse generation by leveraging SMS structures as artificial saturable absorbers (SAs) within an Erbium-doped fiber laser (EDFL). The primary objective is to assess the feasibility and efficacy of employing these SMS structures to produce ultrashort pulses. Within the 1.5 μm wavelength range, various pulse types were investigated and demonstrated in a ring cavity setup. These included Q-switched pulses, conventional mode-locked pulses, bound-state soliton pulses, dissipative solitons featuring multi-pulses, harmonics, dark pulses arising from domain-wall (DW) interactions, and dark pulses governed by the nonlinear Schrödinger equation (NLSE). The thesis describes the mechanisms underpinning the formation of each pulse type, offering comprehensive analysis of the performance of these ultrashort laser systems.

This study outlines four objectives aimed at achieving the research goal. The first objective involves demonstrating the efficacy of SMS structures as artificial SAs in Qswitched EDFLs and analyzing the performance of the Q-switched pulses. In Chapter 3, Q-switched pulses were observed utilizing an SMS structure based on step-index multimode fiber (SIMMF) as the SA. A SIMMF with a 105 μm core diameter and a length of 158 mm formed the SMS structure. The SA modulated cavity loss for Qswitching through nonlinear multimode interference. At a maximum pump power of 343 mW, the system achieved a maximum pulse repetition rate of 157.7 kHz, with the shortest pulse width recorded at 2.4 μs and a maximum output power of 2.35 mW, corresponding to a pulse energy of 15.0 nJ. A comparison of Q-switching performance between the deployment of natural material (MoS_2) and SIMMF-based SMS structure as SA revealed

that the SMS structure exhibited superior pulse shaping capabilities, enhanced stability, and a higher damage threshold.

The first objective of this study also includes to generate bright solitons in EDFLs through a mode-locking approach employing SMS structures as artificial SAs. Setting the EDFL cavity in the anomalous dispersion regime enabled the realization of conventional soliton and harmonic mode-locked pulses, as detailed in Chapter 3. In Section 3.3, a mode-locked fiber laser with a conventional bright soliton, utilizing a GIMMF-based SMS structure as the artificial SA, was successfully demonstrated. The GIMMF, with a length of 45 mm and core and cladding diameters of 50 μm and 125 μm respectively, was employed. To maintain a high fundamental repetition rate, the total cavity length was kept under 10 meters. Through adjustments in the polarization controller and pump power, a stable soliton Mode-Locked Fiber Laser (MLFL) operating at 1574.1 nm was achieved, boasting a repetition rate of 22 MHz and a pulse duration of 650 fs, facilitated by the self-imaging effect in GIMMF. At a maximum pump power of 140 mW, an average output power of 9.82 mW and a pulse energy of 448 pJ were recorded.

In Section 3.4, observations of the 2^{nd} and 3^{rd} harmonic mode-locking in the anomalous dispersion regime were reported, utilizing a 100 mm GIMMF-based SMS structure as the artificial SA. The 2^{nd} harmonic commenced at 84.7 mW input pump power and maintained a repetition rate of approximately 43.6 MHz until 158.5 mW input pump power. Meanwhile, the third harmonic, with a repetition rate of approximately 64 MHz, commenced at 164.6 mW input pump power. Additionally, the 4^{th} harmonic was observed with a repetition rate of approximately 87 MHz. Stable 2^{nd} HML pulses with a center wavelength of 1576 nm, super mode noise of 34 dB, and a pulse width of 1.02 ps underscored the stability of the pulses throughout the experiment.

It is found in Chapter 3 that the SMS structure based SAs are capable to generate stable pulses in the anomalous dispersion regime with remarkably narrow pulse widths, while also demonstrating the high damage threshold characteristic.

Chapter 4 delves into the generation of bound solitons, ultra-broadband dissipative solitons, and harmonic mode-locking with dissipative solitons utilizing SMS structures as artificial SAs. In section 4.2, the cavity was configured in the anomalous dispersion regime, employing a short segment of GIMMF-based SMS structure to observe soliton formation. Initially, conventional solitons were observed starting at 29.3 mW pump power, exhibiting good long-term stability. These solitons operated at a center wavelength of approximately 1573 nm with a 3 dB spectral bandwidth of 7.83 nm. The Time Bandwidth Product (TBP) of 0.615 indicated chirped pulses. Upon increasing the pump power, tightly and loosely bound solitons coexisted. The time separation between the bound solitons was observed to be 17.3 times and 2.4 times the pulse width, signifying loosely and tightly bound solitons respectively. Subsequently, as the pump power was further increased, only loosely bound solitons were observed, maintaining a constant time separation of 20.4 ps but exhibiting varying peak ratios on the autocorrelation trace. This variation suggests an unequal intensity between the two solitons, with the disparity between them growing larger.

The second objective focuses on generating dissipative solitons in EDFLs utilizing SMS structures as artificial SAs. In sections 4.3 and 4.4, the cavity was configured in the normal dispersion regime by incorporating a 230-meter-long dispersion compensation fiber (DCF). This adjustment facilitated the observation of ultrabroadband dissipative solitons featuring multiple pulses. The spectral profile spanned from 1540 nm to 1630 nm, with a center wavelength around 1570 nm. Remarkably, multi-pulsing commenced at an exceedingly low pump power of 23.2 mW. As the pump power increased up to 220 mW, the number of pulses escalated from 3 to 16, while the pulse width remained constant at approximately 290 fs regardless of the pulse count. An intriguing observation was the

fundamental repetition rate of 851 kHz, accompanied by periodic peaks occurring every 29.9 MHz, aligning well with both the pulse interval and the interval of the pulse clusters. In section 4.4, up to the 5th harmonics of dissipative solitons were demonstrated utilizing a GIMMF-based SMS structure. Fundamental mode-locking was initiated at 23.2 mW with a repetition rate of 858 kHz. Upon increasing the pump power to a maximum of 152.3 mW, the 2nd, 3rd, 4th, and 5th harmonic mode-locking (HML) were observed, exhibiting repetition rates of 1.72 MHz, 2.56 MHz, 3.40 MHz, and 4.29 MHz respectively. Operating at a wavelength of 1572 nm with a pulse width of 290 fs, these findings highlight the ability of SMS structure to produce ultrashort dissipative solitons in EDFLs.

The third objective is dedicated to generating dark pulses using SMS structures as artificial SAs. In Chapter 5, domain-wall dark pulses were observed in both anomalous and normal dispersion regimes employing SMS structures as SAs. In the anomalous dispersion regime, a dual-wavelength domain-wall dark pulse was identified, centered at 1567.2 nm and 1569.4 nm. Operating at a fundamental repetition rate of 21.5 MHz, this pulse exhibited the highest average pulse energy of 769.6 pJ, a pulse width of 5 ns, and a SNR of 49 dB. A comparison with results obtained using Polyacrylonitrile thin film as a real SA highlighted the superior power endurance and easier fabrication process associated with SMS structures. In the normal dispersion regime, the 163rd harmonic mode-locked domain-wall dark pulse was demonstrated. This pulse featured dual peaks in the spectra centered at 1562.5 nm and 1569.9 nm. Operating at a fundamental repetition rate of 139.8 MHz, corresponding to the 163rd harmonic order, this pulse achieved a high average pulse energy of 109.7 pJ. Remarkably, no discernible noise floor was observed in the pulse train, while the pulse width and SNR stood at 3.04 ns and 35 dB, respectively. These findings underscore the versatility and potential of SMS structures in generating dark pulses across various dispersion regimes within EDFLs.

In summary, the four outlined objectives have been successfully accomplished. Utilizing SMS structures as artificial SAs and employing straightforward cavity settings alongside dispersion management, a diverse array of pulse types was observed within an EDFL by adjusting the polarization controller and input pump power. The proposed SMS structure, characterized by its simplicity, low cost, and ease of fabrication, demonstrated the capacity to generate stable ultrashort pulses across both normal and anomalous dispersion regions. Remarkably, no damage was observed to any of the SMS structures throughout the experiments, demonstrating their high damage threshold and excellent stability as SAs. The results of these experiments position the SMS structure as a promising candidate for various types of ultrashort pulse generation in EDFLs operating in both normal and anomalous dispersion regimes. Additionally, these findings offer novel insights into pulse formation dynamics, enriching the understanding of EDFL behavior when coupled with SMS structures.

6.2 Novelty and Contributions

The research demonstrated and evaluated the efficacy of SMS structures in generating various types of ultrashort pulsed lasers systematically for the first time, especially with dark pulse discussed. Pulse formation mechanisms were studied with the SMS structure in different dispersion regimes, showing the influence of dispersion on pulse formation. SMS structures are proven to be effective artificial SA with low cost, high damage threshold and easy fabrication process. The demonstration of different kinds of pulse formation showcases the versatility of SMS structure for soliton generation. Key contributions of this work include:

- Successfully demonstrated and evaluated Q-switched EDFLs with SMS structures based on SIMMF as SAs. The study included an analysis of Qswitched pulse performance and a comparison of SMS structures with varying SIMMF lengths.

- Demonstrated and evaluated conventional solitons and their harmonics using SMS structures. The performance of solitons was analyzed across time, frequency, and spectrum domains, with evaluations of Time-Bandwidth Product (TBP) to assess pulse quality. Calculations of peak power and pulse energy highlighted the high damage thresholds of SMS structures.
- Showcasing various mode-locked operations employing different SMS structures across different dispersion regimes and evaluating the performance of the proposed SMS structures. This included bound state solitons, ultra-wide spectrum dissipative solitons, and dissipative soliton harmonics, underscoring the versatility of SMS structures across diverse pulsed laser applications.
- Pioneering the development of dark pulses in EDFLs utilizing SMS structures. This involved demonstrating and evaluating DW dark pulses and harmonic mode locked DW dark pulses in anomalous and normal dispersion regime respectively. The mechanism and performance of these dark pulses were meticulously analyzed, highlighting the potential of SMS structures for dark pulse generation.

The significance of the fundamental study of ultrashort pulse formation with SMS structures comes from the improvement of ultrashort laser performance in the applications. SMS structure as artificial SA is good candidate for ultrashort pulse formation. Ultrashort pulses are widely used in industrial and scientific applications. For instance, ultrashort pulsed lasers can act as laser source for Terahertz laser and frequency comb. Terahertz applications include flaw detection in manufacturing, security screening, medical imaging, sensing and communication. Frequency comb is widely used in atomic clock, spectroscopy, LiDAR, microwave synthesis and optical communication. Small steps of improvement lead to the widespread of laser usage in present days.

6.3 Future Work

Current work focused on experimental work and the evaluation of the performance of SMS structures. Future research in this domain could explore several promising directions that are not covered in this research.

Firstly, even though experimental work is necessary, there's a need for extensive simulation studies on GIMMF-based SMS structures. Investigating the impact of various parameters, such as GIMMF length, core diameter, refractive index profile, and coupling coefficient, on the saturable absorption properties of the SMS structure could provide valuable insights. Optimizing these parameters has the potential to improve performance metrics like modulation depth, recovery time, and saturation fluence. Due to the complexity of the suggested work, tools such as deep learning are recommended.

Secondly, leveraging the high damage threshold of SMS structure-based artificial SAs, future work could focus on increasing pump power to analyze pulses further. Due to the limitation of the current devices, future increase of the pump power was not possible, but the increased pump power can benefit in many aspects. In Q-switched pulses, higher power could potentially narrow pulse widths to the nanosecond range, facilitating applications requiring high peak power and short pulse durations. Similarly, in mode-locked pulses, higher power levels may lead to increased pulse energy.

Thirdly, investigating stability against environmental perturbations is crucial. According to current study, stability remains a significant concern with SMS structures acting as artificial SAs. Research into stability under various operating conditions could yield insights leading to the development of novel ultrashort laser sources and pulse shaping techniques.

Fourthly, exploring application possibilities of the ultrashort lasers generated by the SMS structures is promising. For instance, investigating their potential in biomedical imaging, sensing, and spectroscopy applications, including compatibility, effectiveness,

and sensitivity, could open up new avenues for utilizing these structures in practical contexts.

REFERENCES

Agrawal, G. (2013a). Chapter 1 - Introduction. In G. Agrawal (Ed.), *Nonlinear Fiber Optics (Fifth Edition)* (pp. 1-25). Academic Press. https://doi.org/https://doi.org/10.1016/B978-0-12-397023-7.00001-2

Agrawal, G. (2013b). Chapter 2 - Pulse Propagation in Fibers. In G. Agrawal (Ed.), *Nonlinear Fiber Optics (Fifth Edition)* (pp. 27-56). Academic Press. https://doi.org/https://doi.org/10.1016/B978-0-12-397023-7.00002-4

Agrawal, G. (2013c). Chapter 7 - Cross-Phase Modulation. In G. Agrawal (Ed.), *Nonlinear Fiber Optics (Fifth Edition)* (pp. 245-293). Academic Press. https://doi.org/https://doi.org/10.1016/B978-0-12-397023-7.00007-3

Agrawal, G. P. (2008). Fiber Lasers. In G. P. Agrawal (Ed.), *Applications of Nonlinear Fiber Optics* (pp. 179-244). Academic Press. https://doi.org/10.1016/b978012374302-2.50006-1

Akhmediev, N., Ankiewicz, A., & Torres, J. (2001, 01/01). Solitons Non-Linear Beams and Pulses. *Optics & Photonics News - OPT PHOTONICS NEWS, 12*.

Akhmediev, N. N., Ankiewicz, A., & Soto-Crespo, J. M. (1997, 11/24/). Multisoliton Solutions of the Complex Ginzburg-Landau Equation. *Physical Review Letters, 79*(21), 4047-4051. https://doi.org/10.1103/PhysRevLett.79.4047

Allison, S. W., & Gillies, G. T. (1994, 1994/04/01). Observations of and applications for self-imaging in optical fibers. *Applied Optics, 33*(10), 1802-1805. https://doi.org/10.1364/AO.33.001802

Bao, Q., Zhang, H., Wang, B., Ni, Z., Lim, C. H. Y. X., Wang, Y., Tang, D. Y., & Loh, K. P. (2011, 2011/07/01). Broadband graphene polarizer. *Nature Photonics, 5*(7), 411-415. https://doi.org/10.1038/nphoton.2011.102

Boiti, M., Laddomada, C., & Pempinelli, F. (1982, 1982/04/01). Nonlinear Schrödinger equation, potential nonlinear Schrödinger equation and soliton solutions. *Il*

Nuovo Cimento A (1965-1970), 68(3), 236-248. https://doi.org/10.1007/BF02817707

Chen, G., Wang, H., Zhu, J., Li, H., & Zhu, L. (2021, 2021/01/01/). Generation of transition of dark into bright and harmonic pulses in a passively Er-doped fiber laser using nonlinear multimodal interference technique. *Infrared Physics & Technology, 112*, 103607. https://doi.org/https://doi.org/10.1016/j.infrared.2020.103607

Chen, J., Wang, Z., Li, L., Wang, D. N., Zhu, T., Gao, F., Cao, S., & Fang, Z. (2020). GIMF-Based SA for Generation of High Pulse Energy Ultrafast Solitons in a Mode-Locked Linear-Cavity Fiber Laser. *Journal of Lightwave Technology, 38*(6), 1480-1485. https://doi.org/10.1109/jlt.2019.2954828

Chen, T., Wei, X., Zhang, X., Chen, L., Ren, Y., Peng, F., Zhang, H., & Xia, W. (2021). Evolution of noise-like pulses in mode-locked fiber laser based on straight graded-index multimode fiber structure. *Optics & Laser Technology, 143*. https://doi.org/10.1016/j.optlastec.2021.107347

Diblawe, A. M., Ahmad, B. A., Dimyati, K., Rosol, A. H. A., Tiu, Z. C., Apsari, R., & Harun, S. W. (2023, 2023/03/01). Q-Switched Thulium-Doped Fiber Laser with Molybdenum–Aluminum-Boride-Based Saturable Absorber. *Journal of Russian Laser Research, 44*(2), 172-178. https://doi.org/10.1007/s10946-023-10120-2

Ding, E., Lefrancois, S., Kutz, J., & Wise, F. (2011, 05/01). Scaling Fiber Lasers to Large Mode Area: An Investigation of Passive Mode-Locking Using a MultiMode Fiber. *IEEE journal of quantum electronics, 47*, 597-606. https://doi.org/10.1109/JQE.2011.2107730

Dong, T., Lin, J., Yong, Z., Gu, C., Yao, P., & Xu, L. (2020, 11/01). Noise-like square pulses in a linear-cavity NPR mode-locked Yb-doped fiber laser. *Optics & Laser Technology, 136*, 106740. https://doi.org/10.1016/j.optlastec.2020.106740

Fan, Y., Wang, D. N., & Xu, B. (2023). Generation of conventional solitons and bound state solitons in a passively mode-locked fiber laser based on GIMF–NCF– GIMF structured saturable absorber. *Laser Physics Letters, 20*(6). https://doi.org/10.1088/1612-202X/acd4a6

Fu, S., Sheng, Q., Zhu, X., Shi, W., Yao, J., Shi, G., Norwood, R. A., & Peyghambarian, N. (2015, Jun 29). Passive Q-switching of an all-fiber laser induced by the Kerr effect of multimode interference. *Optics Express, 23*(13), 17255-17262. https://doi.org/10.1364/OE.23.017255

Gan, Y., Wu, Q., Yao, Y., Liu, C., & Fu, Y. (2020, 7-11 Sept. 2020). Observation of Various Bound States of Solitons in a Fiber Laser Based on GIMF-SIMF-GIMF Saturable Absorber. 2020 IEEE 5th Optoelectronics Global Conference (OGC),

Gan, Y., Wu, Q., Yao, Y., Liu, C., Fu, Y., Yang, Y., Tian, J., & Xu, K. (2021). Generation of high-order solitons with order continuously adjustable in a fiber laser based on GIMF–SIMF–GIMF saturable absorber. *Optics Communications, 479*. https://doi.org/10.1016/j.optcom.2020.126441

Ge, Y. Q., Luo, J. L., Li, L., Jin, X. X., Tang, D. Y., Shen, D. Y., Zhang, S. M., & Zhao, L. M. (2015, 2015/01/01). Initial conditions for dark soliton generation in normal-dispersion fiber lasers. *Applied Optics, 54*(1), 71-75. https://doi.org/10.1364/AO.54.000071

Gene, J., Kim, S. K., Do Lim, S., & Jeon, M. Y. (2023, 2023/10/16). Ultrafast dissipative soliton generation in anomalous dispersion achieving high peak power beyond the limitation of cubic nonlinearity. *PhotoniX, 4*(1), 36. https://doi.org/10.1186/s43074-023-00112-5

Gong, Y., Shum, P., Hiang, T., Cheng, Wen, Q., & Tang, D. (2001, 2001/12/15/). Bound soliton pulses in passively mode-locked fiber laser. *Optics Communications, 200*(1), 389-399. https://doi.org/https://doi.org/10.1016/S0030-4018(01)01644-3

Grelu, P., & Akhmediev, N. (2012, 2012/02/01). Dissipative solitons for mode-locked lasers. *Nature Photonics, 6*(2), 84-92. https://doi.org/10.1038/nphoton.2011.345

Gu, H., Qin, Z., Xie, G., Hai, T., Yuan, P., Ma, J., & Qian, L. (2020, 01/01). Generation of 131 fs mode-locked pulses from 2.8 μm Er:ZBLAN fiber laser. *Chinese Optics Letters, 18*, 031402. https://doi.org/10.3788/COL202018.031402

Guangwei Chen, H. W., Jing Zhu, Huiyu Li, Liangqing Zhu. (2021). Generation of transition of dark into bright and harmonic pulses in a passively Er-doped fiber laser using nonlinear multimodal interference technique. *Infrared Physics and Technology, 112*(103607).

Guo, B., Guo, X., Zhou, R., Ren, Z., Chen, Q., Xu, R., & Luo, W. (2022, Dec 30). Multi-Pulse Bound Soliton Fiber Laser Based on MoTe(2) Saturable Absorber. *Nanomaterials (Basel), 13*(1). https://doi.org/10.3390/nano13010177

Haboucha, A., Komarov, A., Leblond, H., Sanchez, F., & Martel, G. (2008, 10/01). Mechanism of multiple pulse formation in the normal dispersion regime of passively mode-locked fiber ring lasers. *Optical Fiber Technology, 14*, 262–267. https://doi.org/10.1016/j.yofte.2008.01.001

Haelterman, M., & Badolo, M. (1995, Nov 15). Dual-frequency wall solitary waves for nonreturn-to-zero signal transmission in W-type single-mode fibers. *Opt Lett, 20*(22), 2285. https://doi.org/10.1364/ol.20.002285

Haelterman, M., & Sheppard, A. P. (1994, Jan 15). Polarization domain walls in diffractive or dispersive Kerr media. *Opt Lett, 19*(2), 96. https://doi.org/10.1364/ol.19.000096

Hasegawa, A., & Tappert, F. (1973a). Transmission of stationary nonlinear optical pulses in dispersive dielectric fibers. I. Anomalous dispersion. *Applied Physics Letters, 23*, 142-144. https://doi.org/10.1063/1.1654836

Hasegawa, A., & Tappert, F. (1973b). Transmission of stationary nonlinear optical pulses in dispersive dielectric fibers. II. Normal dispersion. *Applied Physics Letters, 23*(4), 171-172. https://doi.org/10.1063/1.1654847

Haus, H. A. (2000). Mode-locking of lasers. *IEEE Journal of Selected Topics in Quantum Electronics, 6*(6), 1173-1185. https://doi.org/10.1109/2944.902165

Haus, H. A., Fujimoto, J. G., & Ippen, E. P. (1991, 1991/10/01). Structures for additive pulse mode locking. *Journal of the Optical Society of America B, 8*(10), 20682076. https://doi.org/10.1364/JOSAB.8.002068

He, W., Pang, M., Yeh, D.-H., Huang, J., & Russell, P. S. J. (2021, 2021/06/07). Synthesis and dissociation of soliton molecules in parallel optical-soliton reactors. *Light: Science & Applications, 10*(1), 120. https://doi.org/10.1038/s41377-021-00558-x

Hisyam, M. B., Rusdi, M. F. M., Latiff, A. A., & Harun, S. W. (2017). Generation of Mode-Locked Ytterbium Doped Fiber Ring Laser Using Few-Layer Black Phosphorus as a Saturable Absorber. *IEEE Journal of Selected Topics in Quantum Electronics, 23*(1), 39-43. https://doi.org/10.1109/JSTQE.2016.2532270

Hong, J., Tiu, Z., Batumalay, M., Harith, Z., Diblawe, A. M., Anand, T. J., & Harun, S. (2023, 12/19). Ultrafast Erbium-doped Fiber Laser Using Electrodeposition Coated MoS2 Thin Film As Saturable Absorber. *Materials Research Express, 10*. https://doi.org/10.1088/2053-1591/ad144c

Keller, U. (2022). *Ultrafast Lasers: A Comprehensive Introduction to Fundamental Principles with Practical Applications*. Springer International Publishing. https://books.google.com.my/books?id=jjuEzgEACAAJ

Keller, U., Weingarten, K. J., Kartner, F. X., Kopf, D., Braun, B., Jung, I. D., Fluck, R., Honninger, C., Matuschek, N., & Au, J. A. d. (1996). Semiconductor saturable absorber mirrors (SESAM's) for femtosecond to nanosecond pulse generation in solid-state lasers. *IEEE Journal of Selected Topics in Quantum Electronics, 2*(3), 435-453. https://doi.org/10.1109/2944.571743

Komarov, A., Leblond, H., & Sanchez, F. (2005, 05/20/). Multistability and hysteresis phenomena in passively mode-locked fiber lasers. *Physical Review A, 71*(5), 053809. https://doi.org/10.1103/PhysRevA.71.053809

Komarov, A., Leblond, H., & Sanchez, F. (2006, 2006/11/01/). Passive harmonic modelocking in a fiber laser with nonlinear polarization rotation. *Optics Communications, 267*(1), 162-169.

https://doi.org/https://doi.org/10.1016/j.optcom.2006.06.012

Koo, J., Ashok, N., Kim, D., & Shin, W. (2019, 06/29). Bi2Te3 Topological Insulator for Domain-Wall Dark Pulse Generation from Thulium-Doped Fiber Laser. *Crystals, 9*, 337. https://doi.org/10.3390/cryst9070337

Kulagin, A. E., & Shapovalov, A. V. (2024). A Semiclassical Approach to the Nonlocal Nonlinear Schrödinger Equation with a Non-Hermitian Term. *Mathematics, 12*(4).

Li, C., Krauß, N., Schäfer, G., Ebner, L., Kliebisch, O., Schmidt, J., Winnerl, S., Hettich, M., & Dekorsy, T. (2017). High-speed asynchronous optical sampling based on GHz Yb: KYW oscillators. *Optics express, 25*(8), 9204-9212.

Li, H., Hu, F., Tian, Y., Wang, P., Zhang, J., & Xu, S. (2019, May 13). Continuously wavelength-tunable mode-locked Tm fiber laser using stretched SMF-GIMFSMF structure as both saturable absorber and filter. *Optics Express, 27*(10), 14437-14446. https://doi.org/10.1364/OE.27.014437

Li, H., Wang, Z., Li, C., Zhang, J., & Xu, S. (2017, Oct 30). Mode-locked Tm fiber laser using SMF-SIMF-GIMF-SMF fiber structure as a saturable absorber. *Optics Express, 25*(22), 26546-26553. https://doi.org/10.1364/OE.25.026546

Li, J., Luo, H., Zhai, B., Lu, R., Guo, Z., Zhang, H., & Liu, Y. (2016, 2016/07/26). Black phosphorus: a two-dimension saturable absorption material for midinfrared Q-switched and mode-locked fiber lasers. *Scientific Reports, 6*(1), 30361. https://doi.org/10.1038/srep30361

Li, L., Wang, Y., Wang, X., Lv, R., Liu, S., Chen, Z., & Wang, J. (2018, 2018/07/01/). Generation of dark solitons in Er-doped fiber laser based on ferroferric-oxide nanoparticles. *Optics & Laser Technology, 103*, 354-358. https://doi.org/https://doi.org/10.1016/j.optlastec.2018.01.060

Li, N., Guo, M., Zhang, W. Y., Zhang, J., Guo, Z. X., Zheng, T. Q., Li, Y. Z., An, S. R., & Song, L. J. (2021). A nanosecond Q-switched fiber laser based on step-index multimode fiber. *Laser Physics, 31*(8). https://doi.org/10.1088/15556611/ac089f

Li, N., Zhang, W., Guo, M., Li, M., & Guo, Z. (2021). A tunable Q-switched erbium fiber laser based on one all fiber structure as both saturable absorber and filter. *Optics Communications, 484*, 126698.

Li, S., Yin, Y., Lewis, E., Garrell, G., Rosol, A. H. A., Latiff, A. A., Harun, S. W., Guo, B., & Wang, P. (2019). All fibre Q-switched Thulium-doped fibre laser incorporating Thulium–Holmium co-doped fibre as a saturable absorber. *Optics Communications, 450*, 160-165. https://doi.org/10.1016/j.optcom.2019.05.058

Li, X., Jin, L., Sui, Y., Liu, Y., Xu, C., Wang, Y., Zhang, H., Xu, Y., & Ma, X. (2023). 2.11 GHz all-fiber harmonic mode-locked laser based on highly nonlinear hybrid multimode interference saturable absorber. *Optics Communications, 545*. https://doi.org/10.1016/j.optcom.2023.129632

Lin, Z.-B., Luo, A.-P., Wang, S.-K., Wang, H.-Y., Cao, W.-J., Luo, Z.-C., & Xu, W.-C. (2012, 2012/10/01/). Generation of dual-wavelength domain-wall rectangularshape pulses in HNLF-based fiber ring laser. *Optics & Laser Technology, 44*(7), 2260-2264. https://doi.org/https://doi.org/10.1016/j.optlastec.2012.02.029

Liu, H. H., & Chow, K. K. (2014, 2014/12/01). Dark pulse generation in fiber lasers incorporating carbon nanotubes. *Optics Express, 22*(24), 29708-29713. https://doi.org/10.1364/OE.22.029708

Liu, J., Zhao, F., Wang, H., Zhang, W., Hu, X., Li, X., & Wang, Y. (2019, 2019/03/01/). Generation of dark solitons in erbium-doped fiber laser based on black phosphorus nanoparticles. *Optical Materials, 89*, 100-105. https://doi.org/https://doi.org/10.1016/j.optmat.2018.12.055

Lü, R., Wang, Y., Wang, J., Ren, W., Li, L., Liu, S., Chen, Z., Li, Y., Wang, H., & Fu, F. (2019). Soliton and bound-state soliton mode-locked fiber laser based on a MoS2/fluorine mica Langmuir–Blodgett film saturable absorber. *Photonics Research, 7*(4). https://doi.org/10.1364/prj.7.000431

Lv, Z., Teng, H., Fang, S., Jia, H., Wang, L., Wang, J., & Wei, Z. (2016, 2016/05/06). A harmonically mode-locked dark soliton and bright–dark soliton pair ytterbium fiber laser. *Journal of Optics, 18*(6), 065502. https://doi.org/10.1088/20408978/18/6/065502

Lv, Z., Yang, Z., Song, D., Li, F., Yang, Y., Yang, X., Wang, Y., Li, Q., & Zhao, W. (2019, 2019/11/01/). Observation of dissipative soliton bound states in a nonlinear multimodal interference based all-fiber all-normal-dispersion modelocking laser. *Optics & Laser Technology*, *119*, 105626. https://doi.org/https://doi.org/10.1016/j.optlastec.2019.105626

Lyu, Y., Zou, X., Shi, H., Liu, C., Wei, C., Li, J., Li, H., & Liu, Y. (2017, 2017/06/12). Multipulse dynamics under dissipative soliton resonance conditions. *Optics Express, 25*(12), 13286-13295. https://doi.org/10.1364/OE.25.013286

Malomed, B. A. (1991, 11/01/). Bound solitons in the nonlinear Schr\"odinger-Ginzburg-Landau equation. *Physical Review A, 44*(10), 6954-6957. https://doi.org/10.1103/PhysRevA.44.6954

Malomed, B. A. (1992, 06/01/). Bound solitons in coupled nonlinear Schr\"odinger equations. *Physical Review A, 45*(12), R8321-R8323. https://doi.org/10.1103/PhysRevA.45.R8321

Marini, A., Cox, J., & De Abajo, F. G. (2017). Theory of graphene saturable absorption. *Physical Review B, 95*(12), 125408.

Martinez, A., & Sun, Z. (2013). Nanotube and graphene saturable absorbers for fibre lasers. *Nature Photonics, 7*(11), 842-845.

Menyuk, C. R. (1987, Aug 1). Stability of solitons in birefringent optical fibers. I: equal propagation amplitudes. *Opt Lett, 12*(8), 614-616. https://doi.org/10.1364/ol.12.000614

Michalska, M., Michalski, J., Grzes, P., & Swiderski, J. (2022). Bound-State Soliton and Noise-like Pulse Generation in a Thulium-Doped Fiber Laser Based on a Nonlinear Optical Loop Mirror. *Applied Sciences, 12*(3), 1664. https://www.mdpi.com/2076-3417/12/3/1664

Mohanraj, J., Velmurugan, V., & Sivabalan, S. (2016, 2016/10/01/). Transition metal dichalcogenides based saturable absorbers for pulsed laser technology. *Optical Materials, 60*, 601-617. https://doi.org/https://doi.org/10.1016/j.optmat.2016.09.007

Mohd Rusdi, M. F., Latiff, A. A., Paul, M. C., Das, S., Dhar, A., Ahmad, H., & Harun, S. W. (2017, 2017/03/01/). Titanium Dioxide (TiO2) film as a new saturable absorber for generating mode-locked Thulium-Holmium doped all-fiber laser. *Optics & Laser Technology, 89*, 16-20. https://doi.org/https://doi.org/10.1016/j.optlastec.2016.09.040

Mollenauer, L. F., & Smith, K. (1988, 1988/08/01). Demonstration of soliton transmission over more than 4000 km in fiber with loss periodically compensated by Raman gain. *Optics Letters, 13*(8), 675-677. https://doi.org/10.1364/OL.13.000675

Muhamad Apandi, N. H., Ahmad, H., Lokman, M. Q., Zuikafly, S. N. F., Yahaya, H., Ibrahim, M. H., Rosnan, R. M., & Ahmad, F. (2023). Observation of soliton and bound soliton in erbium-doped fiber lasers using single-walled carbon nanotubes mode-lockers under gamma irradiation. *Optics & Laser Technology, 157*. https://doi.org/10.1016/j.optlastec.2022.108775

Na, Y., Jeon, C.-G., Ahn, C., Hyun, M., Kwon, D., Shin, J., & Kim, J. (2020). Ultrafast, sub-nanometre-precision and multifunctional time-of-flight detection. *Nature Photonics, 14*(6), 355-360.

Nazemosadat, E., & Mafi, A. (2013a, 2013/05/01). Nonlinear multimodal interference and saturable absorption using a short graded-index multimode optical fiber. *Journal of the Optical Society of America B, 30*(5), 1357-1367. https://doi.org/10.1364/JOSAB.30.001357

Nazemosadat, E., & Mafi, A. (2013b, 2013/12/16). Nonlinear switching in multicore versus multimode waveguide junctions for mode-locked laser applications. *Optics Express, 21*(25), 30739-30745. https://doi.org/10.1364/OE.21.030739

Noor, S. F. S. M., Ahmad, B. A., Rosol, A. H. A., Ahmad, H., Apsari, R., & Harun, S. W. (2022). Dual-wavelength Q-switched erbium-doped fiber laser using an SMF-MMF-SMF structure and graphene oxide. *Optoelectronics Letters, 18*(11), 668-672. https://doi.org/10.1007/s11801-022-2097-3

Okamoto, K. (2022). Chapter 5 - Nonlinear Optical Effects in Optical Fibers. In K. Okamoto (Ed.), *Fundamentals of Optical Waveguides (Third Edition)* (pp. 219269). Academic Press. https://doi.org/https://doi.org/10.1016/B978-0-12815601-8.50005-7

Okhotnikov, O., Grudinin, A., & Pessa, M. (2004, 2004/11/26). Ultra-fast fibre laser systems based on SESAM technology: new horizons and applications. *New Journal of Physics, 6*(1), 177. https://doi.org/10.1088/1367-2630/6/1/177

Oreshnikov, I., Driben, R., & Yulin, A. (2017, 07/07/). Dispersive radiation and regime switching of oscillating bound solitons in twin-core fibers near zero-dispersion wavelength. *Physical Review A, 96*(1), 013809. https://doi.org/10.1103/PhysRevA.96.013809

Pang, M., He, W., Jiang, X., & Russell, P. S. J. (2016, 2016/07/01). All-optical bit storage in a fibre laser by optomechanically bound states of solitons. *Nature Photonics, 10*(7), 454-458. https://doi.org/10.1038/nphoton.2016.102

Paschotta, R. (2008). *Field Guide to Laser Pulse Generation*. SPIE Press. https://books.google.com.my/books?id=ZA2tNi7QEPEC

Peng, J., Zhan, L., Luo, S., & Shen, Q. (2013). Passive Harmonic Mode-Locking of Dissipative Solitons in a Normal-Dispersion Er-Doped Fiber Laser. *Journal of Lightwave Technology, 31*(16), 2709-2714. https://doi.org/10.1109/jlt.2013.2271773

Qi, Y., Wang, J., Bai, Z., Yang, S., Ding, J., Yan, B., Wang, Y., & Lu, Z. (2022). Tunable all fiber multi-wavelength mode-locked laser with a large dynamic range using polarization controller coiled SMF-GIMF-SMF structure as both saturable absorber and comb filter. *Optical Fiber Technology, 74*. https://doi.org/10.1016/j.yofte.2022.103055

Ren, X., Li, H., Zhang, Z., Zhang, J., & Xu, S. (2022, 2022/05/01/). Generation of bound solitons in a mode- locked Tm-doped fiber laser based on a graded-index multimode fiber saturable absorber. *Optics & Laser Technology, 149*, 107865. https://doi.org/https://doi.org/10.1016/j.optlastec.2022.107865

Sakaguchi, H., Skryabin, D. V., & Malomed, B. A. (2018, 2018/06/01). Stationary and oscillatory bound states of dissipative solitons created by third-order dispersion. *Optics Letters, 43*(11), 2688-2691. https://doi.org/10.1364/OL.43.002688

Seong, N. H., & Kim, D. Y. (2002, 2002/03/17). Formation of Bound Solitons and their Properties in a Figure-eight Fiber Laser.*OSA Trends in Optics and Photonics* Optical Fiber Communications Conference, Anaheim, California.

Set, S. Y., Yaguchi, H., Tanaka, Y., Jablonski, M., Sakakibara, Y., Rozhin, A., Tokumoto, M., Kataura, H., Achiba, Y., & Kikuchi, K. (2003, 28-28 March 2003). Mode-locked fiber lasers based on a saturable absorber incorporating carbon nanotubes. OFC 2003 Optical Fiber Communications Conference, 2003.,

Shimizu, F. (1967, 11/06/). Frequency Broadening in Liquids by a Short Light Pulse. *Physical Review Letters, 19*(19), 1097-1100. https://doi.org/10.1103/PhysRevLett.19.1097

Silva, L. C. B., Pizarro, Y. A. A., Vieira, M. A., Freitas, J. C. C., Segatto, M. E. V., Pontes, M. J., & Castellani, C. E. S. (2019, 2019/11/20). Stable dark pulses produced by a graphite oxide saturable absorber in a fiber laser cavity. *Applied Optics, 58*(33), 9297-9304. https://doi.org/10.1364/AO.58.009297

Sobon, G., Sotor, J., Martynkien, T., & Abramski, K. M. (2016, Mar 21). Ultrabroadband dissipative soliton and noise-like pulse generation from a normal dispersion mode-locked Tm-doped all-fiber laser. *Optics Express, 24*(6), 61566161. https://doi.org/10.1364/OE.24.006156

Spühler, G. J., Paschotta, R., Fluck, R., Braun, B., Moser, M., Zhang, G., Gini, E., & Keller, U. (1999, 1999/03/01). Experimentally confirmed design guidelines for passively Q-switched microchip lasers using semiconductor saturable absorbers. *Journal of the Optical Society of America B, 16*(3), 376-388. https://doi.org/10.1364/JOSAB.16.000376

Stratmann, M., Pagel, T., & Mitschke, F. (2005, 09/28/). Experimental Observation of Temporal Soliton Molecules. *Physical Review Letters, 95*(14), 143902. https://doi.org/10.1103/PhysRevLett.95.143902

Sylvestre, T., Coen, S., Emplit, P., & Haelterman, M. (2002, Apr 1). Self-induced modulational instability laser revisited: normal dispersion and dark-pulse train generation. *Opt Lett, 27*(7), 482-484. https://doi.org/10.1364/ol.27.000482

Tang, D., Zhao, L., Zhao, B., & Liu, A.-q. (2009, 10/30). Mechanism of multisoliton formation and soliton energy quantization in passively mode-locked fiber lasers. *Physical Review A, 72*. https://doi.org/10.1103/PhysRevA.72.043816

Tang, D. Y., Zhao, L. M., & Zhao, B. (2005, 2005/02/01). Multipulse bound solitons with fixed pulse separations formed by direct soliton interaction. *Applied Physics B, 80*(2), 239-242. https://doi.org/10.1007/s00340-004-1685-1

Thulasi, S., & Sivabalan, S. (2021). All-Fiber Femtosecond Mode-Locked Yb-Laser With Few-Mode Fiber as a Saturable Absorber. *IEEE Photonics Technology Letters, 33*(5), 223-226. https://doi.org/10.1109/lpt.2021.3053418

Tiu, Z. C., Harun, S. W., Ahmad, H., Samion, M. Z., & Tan, S. J. (2022). Review: Dark pulse generation in fiber laser system. *Optics & Laser Technology, 151*. https://doi.org/10.1016/j.optlastec.2022.108056

Tiu, Z. C., Suthaskumar, M., Zarei, A., Tan, S. J., Ahmad, H., & Harun, S. W. (2015, 2015/10/01/). Generation of switchable domain wall and Cubic–Quintic nonlinear Schrödinger equation dark pulse. *Optics & Laser Technology, 73*, 127129. https://doi.org/https://doi.org/10.1016/j.optlastec.2015.04.010

Wang, C., Fomovsky, M., Miao, G., Zyablitskaya, M., & Vukelic, S. (2018). Femtosecond laser crosslinking of the cornea for non-invasive vision correction. *Nature Photonics, 12*(7), 416-422.

Wang, F., Zhang, X., & Cui, J. (2020, 08/01). Generation of soliton rain in a passive mode-locked Tm-doped fiber laser at 2 μm. *Optics & Laser Technology, 128*, 106228. https://doi.org/10.1016/j.optlastec.2020.106228

Wang, M., Zhao, K., Wu, J., Li, Y., Yang, Y., Huang, S., Zhao, J., Tweedle, T., Carpenter, D., & Zheng, G. (2021). Femtosecond laser fabrication of nanograting-based distributed fiber sensors for extreme environmental applications. *International Journal of Extreme Manufacturing, 3*(2), 025401.

Wang, P., Zhao, K., Xiao, X., & Yang, C. (2017, Nov 27). Pulse dynamics of dualwavelength dissipative soliton resonances and domain wall solitons in a Tm fiber laser with fiber-based Lyot filter. *Optics Express, 25*(24), 30708-30719. https://doi.org/10.1364/oe.25.030708

Wang, Q. H., Kalantar-Zadeh, K., Kis, A., Coleman, J. N., & Strano, M. S. (2012, 2012/11/01). Electronics and optoelectronics of two-dimensional transition metal dichalcogenides. *Nature Nanotechnology, 7*(11), 699-712. https://doi.org/10.1038/nnano.2012.193

Wang, R., Jin, L., Wang, J., Xie, S., Li, X., Xu, Y., Zhang, H., Zhao, X., & Ma, X. (2022). Harmonic mode-locked fiber laser based on microfiber-assisted nonlinear multimode interference. *Chinese Optics Letters, 20*(1). https://doi.org/10.3788/col202220.010601

Wang, T., Jin, L., Zhang, H., Pan, W., Zhang, H., Xu, Y., Shi, L., Li, Y., Zou, Y., & Ma, X. (2020). Gigahertz Harmonic Mode‐Locked Fiber Laser Based on Tunable SMS Ultrafast Optical Switch. *Annalen der Physik, 532*(5). https://doi.org/10.1002/andp.202000018

Wang, X.-f., Jin, Z.-g., & Liu, J.-h. (2021, 01/12). 2.04 μm harmonic noise-like pulses generation from a mode-locked fiber laser based on nonlinear polarization rotation. *Optoelectronics Letters, 17*, 18-21. https://doi.org/10.1007/s11801-0210028-3

Wang, X., Liu, Y., Wang, Z., Wang, Z., & Yang, G. (2018, 12/21). L-Band Efficient Dissipative Soliton Erbium-Doped Fiber Laser With a Pulse Energy of 6.15 nJ and 3 dB Bandwidth of 47.8 nm. *Journal of Lightwave Technology, PP*, 1-1. https://doi.org/10.1109/JLT.2018.2889050

Wang, X., Wang, Z., Shen, C., Zhang, X., Huang, S., & Guo, T. (2024, 2024/05/01/). Generation of spatiotemporal dark pulse or polarization domain wall solitons in a partial multimode mode-locked fiber laser. *Infrared Physics & Technology, 138*, 105249. https://doi.org/https://doi.org/10.1016/j.infrared.2024.105249

Wang, Y., Li, J., Mo, K., Wang, Y., Liu, F., & Liu, Y. (2017, 2017/08/10). 14.5 GHz passive harmonic mode-locking in a dispersion compensated Tm-doped fiber laser. *Scientific Reports, 7*(1), 7779. https://doi.org/10.1038/s41598-017-063265

Wang, Y., & Xu, C.-Q. (2007, 2007/01/01/). Actively Q-switched fiber lasers: Switching dynamics and nonlinear processes. *Progress in Quantum Electronics, 31*(3), 131-216. https://doi.org/https://doi.org/10.1016/j.pquantelec.2007.06.001

Wang, Z., Li, L., Wang, D. N., Le, Z., Zhang, S., Cao, S., & Fang, Z. (2019, 2019/02/01). Generation of pulse-width controllable dissipative solitons and bound solitons by using an all fiber saturable absorber. *Optics Letters, 44*(3), 570-573. https://doi.org/10.1364/OL.44.000570

Wu, Q.-C., Zou, Z.-M., Yao, Y., Shi, J., Wu, C.-H., Yang, Y.-F., Tian, J.-J., & Xu, K. (2019). Femtosecond Soliton Erbium-Doped Fiber Laser With a Symmetrical GIMF–SIMF–GIMF Saturable Absorber. *Ieee Photonics Journal, 11*(6), 1-9. https://doi.org/10.1109/jphot.2019.2950379

Wun, J.-M., Liu, H.-Y., Lai, C.-H., Chen, Y.-S., Yang, S.-D., Pan, C.-L., Bowers, J. E., Huang, C.-B., & Shi, J.-W. (2014). Photonic high-power 160-GHz signal generation by using ultrafast photodiode and a high-repetition-rate femtosecond optical pulse train generator. *IEEE Journal of Selected Topics in Quantum Electronics, 20*(6), 10-16.

Xu, Q., Wang, P., Wang, Q., He, J., Wang, Z., & Liu, Y. (2024). Dynamical diversity of noise-like pulse and soliton explosion in NL-MMI mode-locked Er fiber laser.

Optics & Laser Technology, 168. https://doi.org/10.1016/j.optlastec.2023.109914

Yang, F., Sui, Z., Sun, S., Chen, S., Wang, Y., Fan, W., Li, S., Wang, G., Zhang, W., Lu, C., Fu, S., & Zhang, H. (2022). Demonstration of conventional soliton, bound-state soliton, and noise-like pulse based on chromium sulfide as saturable absorber. *Nanophotonics, 11*(21), 4937-4945. https://doi.org/doi:10.1515/nanoph-2022-0483

Yang, F., Wang, D. N., Wang, Z. K., Li, L. J., Zhao, C. L., Xu, B., Jin, S. Z., Cao, S. Y., & Fang, Z. J. (2018, Jan 22). Saturable absorber based on a single mode fiber - graded index fiber - single mode fiber structure with inner micro-cavity. *Optics Express, 26*(2), 927-934. https://doi.org/10.1364/Oe.26.000927

Yang, Y., Zeng, Q., Yang, Y., Du, G., Ji, J., Song, Y., Wang, Z., & Wang, K. (2024). Generation and Dynamics of Multiple Pulses in an Ultrafast Fiber Laser with a Single-Mode Fiber–Graded-Index Multimode Fiber–Single-Mode Fiber-Based Saturable Absorber. *Photonics, 11*(1).

Yin, H., Xu, W., Luo, A.-P., Luo, Z.-C., & Liu, J. (2010, 2010/11/01/). Observation of dark pulse in a dispersion-managed fiber ring laser. *Optics Communications, 283*(21), 4338-4341. https://doi.org/https://doi.org/10.1016/j.optcom.2010.06.076

Zabusky, N. J., & Kruskal, M. D. (1965, 08/09/). Interaction of "Solitons" in a Collisionless Plasma and the Recurrence of Initial States. *Physical Review Letters, 15*(6), 240-243. https://doi.org/10.1103/PhysRevLett.15.240

Zakharov, V. E., & Shabat, A. B. (1973). Interaction between solitons in a stable medium.

Zakharov, V. E., & Shabat, A. B. (1973). Interaction between solitons in a stable medium. *Sov. Phys. JETP, 37*(5), 823-828.

Zhang, B., Li, P., Liu, Z., Li, M., Liu, J., Zhao, H., Hu, Q., & Chen, X. (2023, 01/01). Generation of 12th order harmonic mode-locking in a Nd-doped single-mode all-

fiber laser operating at 0.9 μm. *Chinese Optics Letters, 21*, 011405. https://doi.org/10.3788/COL202321.011405

Zhang, H., Jin, L., Zhang, H., Xu, Y., Shi, L., Wang, T., Chen, H., Wang, D., & ma, X. (2019). All-fiber nonlinear optical switch based on polarization controller coiled SMF–GIMF–SMF for ultrashort pulse generation. *Optics Communications, 452*, 7-11. https://doi.org/10.1016/j.optcom.2019.07.004

Zhang, H., Tang, D., Zhao, L., & Wu, X. (2011, 2011/02/14). Dual-wavelength domain wall solitons in a fiber ring laser. *Optics Express, 19*(4), 3525-3530. https://doi.org/10.1364/OE.19.003525

Zhang, P., Nizamani, B., Dimyati, K., Yasin, M., & Harun, S. W. (2023, 2023/06/01/). Switchable single/dual-wavelength Q-switched all-fiber laser utilizing thuliumdoped fiber saturable absorber. *Journal of Luminescence, 258*, 119809. https://doi.org/https://doi.org/10.1016/j.jlumin.2023.119809

Zhang, W., Zhan, L., Xian, T., & Gao, L. (2019, 2019/11/11). Bidirectional dark soliton mode-locked fiber laser based on thulium-doped fiber saturable absorber.*OSA Technical Digest* International Photonics and OptoElectronics Meeting 2019 (OFDA, OEDI, ISST, PE, LST, TSA), Wuhan.

Zhang, W., Zhan, L., Xian, T., & Gao, L. (2019). Harmonic Mode-Locking in Bidirectional Domain-Wall Soliton Fiber Lasers. *Journal of Lightwave Technology, 37*(21), 5417-5421. https://doi.org/10.1109/JLT.2019.2942185

Zhang, X., Wang, Z., Gao, F., Zhao, C., Chang, S., & Guo, T. (2022, 2022/09/01/). Observation of multimode solitons in the spatiotemporal mode-locked fiber laser with different chromatic dispersion. *Optics Communications, 518*, 128357. https://doi.org/https://doi.org/10.1016/j.optcom.2022.128357

Zhao, F., Wang, Y., Wang, H., Hu, X., Zhang, W., Zhang, T., & Cai, Y. (2018). Highenergy solitons generation with a nonlinear multimode interference-based saturable absorber. *Laser Physics, 28*(8). https://doi.org/10.1088/15556611/aac538

Zhou, R., Yu, D., Liu, X., Li, Q., & Fu, H. Y. (2019, 2019/08/01). Dark rectangular noise-like pulses in a figure-nine fiber laser based on a nonlinear amplifying loop mirror. *Optics Letters, 44*(15), 3717-3720. https://doi.org/10.1364/OL.44.003717

Zhu, T., Wang, Z., Wang, D. N., Yang, F., & Li, L. (2019, 2019/01/01). Observation of controllable tightly and loosely bound solitons with an all-fiber saturable absorber. *Photonics Research, 7*(1), 61-68. https://doi.org/10.1364/PRJ.7.000061

Zhu, X. (2008). *Multimode Interference in Optical Fibers and Its Applications in Fiber Lasers and Amplifiers* [Doctoral Dissertation, The University of Arizona.]. http://hdl.handle.net/10150/195318

Zou, Z., Shi, J., Wu, Q., & Wu, C. (2019). *Bright-dark pulse pair and soliton bunch generation from mode-locked erbium-doped fiber laser with GIMF-SIMF-GIMF as a saturated absorber*. https://doi.org/10.1117/12.2542226

LIST OF PUBLICATIONS AND PAPERS PRESENTED

Y. Chen, T. Z. Cheak, T. S. Jin, G. Vinitha, K. Dimyati, and S. W. Harun, "Domainwall dark pulse generation with SMF-GIMF-SMF structure as artificial saturable absorber," Scientific Reports, vol. 14, no. 1, p. 2141, 2024/01/25 2024, doi: 10.1038/s41598-024-52640-0.

Y. Chen, K. Dimyati, I. A. Badruddin, S. Kamangar, and S. W. Harun, "All-fiber Qswitched erbium-doped fiber laser generation with SMF-SIMF-SMF structure as artificial saturable absorber," Infrared Physics & Technology, vol. 136, p. 105088, 2024/01/01/ 2024, doi: https://doi.org/10.1016/j.infrared.2023.105088.

Y. Chen, A. H. A. Rosol, S. J. Tan, Z. C. Tiu, K. Dimyati, and S. W. Harun, "Kerr Effect as a Mode Locker in Er-Doped Fiber Laser," Journal of Russian Laser Research, vol. 44, no. 6, pp. 663-668, 2023/11/01 2023, doi: 10.1007/s10946023-10175-1.

Y. Chen, Z. C. Tiu, A. H. A. Rosol, S. J. Tan, K. Dimyati, and S. W. Harun, "All-fibre mode-locked laser using SMF-GIMF-SMF structure as artificial saturable absorber," Results in Optics, p. 100603, 2023/12/31/ 2023, doi: https://doi.org/10.1016/j.rio.2023.100603.

Chen, Y., Tiu, Z. C., Tan, S. J., Dimyati, K., & Harun, S. W. (2024, 2024/07/02). Passively harmonic dissipative soliton generation in normal dispersion erbiumdoped fiber laser using SMS fiber as artificial saturable absorber. Scientific Reports, 14(1), 15134. https://doi.org/10.1038/s41598-024-66111-z

Chen, Y., Dimyati, K., & Wadi Harun, S. (2024, 2024/01/01). Q-switched Erbium Doped Fiber Laser Generation Using the Kerr Effect of Multimode Interference. Journal of Physics: Conference Series, 2696(1), 012003. https://doi.org/10.1088/1742-6596/2696/1/012003